MACHINE LEARNING BASED MINERAL CHARACTERIZATION FROM PORE TO CORE SCALE AND IMPLICATIONS FOR GEOCHEMICAL REACTIVITY

by

Parisa Asadi

A dissertation submitted to the Graduate Faculty of
Auburn University
in partial fulfillment of the
requirements for the Degree of
Doctor of Philosophy

Auburn, Alabama
December 10, 2022

Keywords: CO_2-brine-mineral reaction, reactive transport modeling, energy storage, CO_2 mineralization and solubility trapping, Deep Learning, CrunchFlow

Approved by

Lauren E. Beckingham, Chair, Associate Professor, Department of Civil and Environmental Engineering
Mark O. Barnett, Professor, Department of Civil and Environmental Engineering
Nedret Billor, Professor, Department of Mathematics and Statistics
Frances O'Donnell, Assistant Professor, Civil and Environmental Engineering
Jose Vasconcelos Neto, Associate Professor, Civil and Environmental Engineering

ABSTRACT

Geological formations have great potential for large-scale carbon sequestration to reduce the net rate of increase in atmospheric CO_2. In these systems, CO_2 is injected into formations and mineralized through geochemical reactions. Subsurface CO_2 sequestration systems include reservoirs which store the injected CO_2 and impermeable cap-rocks (mostly shales) which seal the reservoir. Impermeable cap-rocks are a necessary component of subsurface CO_2 sequestration systems to prevent fluid migration and leakage. The presence and evolution of fractures in CO_2 sequestration systems can not only pose a risk to system integrity but also threaten overlying groundwater resources with acidification and contamination via trace element mobilization. This process is complex and not well understood. Reactive transport simulations can be used to simulate the evolution of subsurface CO_2 sequestration systems including mineral reactions and porosity evolution. Micro-scale imaging of geological samples is a powerful technique to obtain the necessary parameters for reactive transport simulations. However, images are typically manually processed by domain experts, which is time-consuming, labor-intensive, and subjective. This study is divided into three main sections. The first two sections of this study propose machine learning and deep learning approaches to facilitate the automatic segmentation of minerals while the third section deals with reactive transport simulation. In the first section, the performance of several filtering techniques with three machine learning methods and a deep learning method was assessed for reliable feature extraction and pixel-level phase segmentation of X-ray CT images. K-means clustering, Random Forest, and Feed Forward Artificial Neural Network, as well as the modified U-Net model, were applied to the extracted input features. The results showed that the U-Net model with the linear combination of focal and dice loss performed best with an accuracy of 0.91

and 0.93 for Mancos and Marcellus shales, respectively. In general, it was found that considering more features provided more promising and reliable segmentation results that are valuable for analyzing the composition of dense samples, such as shales, which are significant unconventional reservoirs in oil recovery and caprocks for CO_2 storage systems.

The second study proposed an intelligent framework that not only evaluates the accuracy of prediction for each pixel but also investigates the accuracy of predicted neighboring pixels. Random Forest and U-Net machine learning were used as primary model architectures for mineral characterization and surface area analysis of six sandstone samples. Various input variable sets including filter extracted features, scanning electron microscopy (SEM) backscatter electron (BSE) images and SEM-energy dispersive x-ray spectroscopy images (EDS) images were considered. A new methodology was proposed to distinguish the more susceptible places to dissolution on the surface of a given mineral using a ranked mineral dissolution risk assessment map. The results showed both methods had an acceptable performance, especially with extracted features as input to the models. However, the U-Net model outperformed the Random Forest in all samples. In addition to high accuracy in both models, the proposed methodology was shown to reliably identify the locations susceptible to dissolution indicated via proposed risk assessment maps. The intelligent segmentation and surface area analysis framework is a promising tool for accelerating the processing of SEM data and reactivity assessment of samples.

The last section of this study aimed to understand the impact of variations in mineralogy of the fracture surface and surrounding matrix on simulated mineral reactions and reaction rates between minerals and CO_2 saturated brine. The porosity, mineral composition, and ion concentration evolutions near fracture surfaces in the context of geologic CO_2 storage, over various mineral distributions on fracture surfaces measured from image analyses of SEM-BSE images and

XRD information, were assessed and compared. Numerical simulations considered reactions with CO_2 acidified brine at short-term scales and long-term which are pertinent for understanding reactions for the typical laboratory experiments and field, respectively.

DEDICATION

I dedicate this dissertation to my husband, Mostafa, for his continued support, patience, and love. I would also like to dedicate this dissertation to the brave women of Iran who are fighting for their freedom and their human rights during the writing of this dissertation. While my heart is deeply saddened by what they are going through, I hope that one day I look at this section of my dissertation and smile to see that they achieve what they have been long yearning for, their freedom.

ACKNOWLEDGMENTS

I would like to thank Dr. Lauren Beckingham, my major advisor, for his extraordinary supervision and direction in the preparation of this dissertation. Dr. Beckingham was beyond an extraordinary supervisor for me, she inspired me in many aspects. Her commitment to work, her dedication to mentorship, and her love for people and family were inspirational. I would also like to acknowledge the advisory committee members including Dr. Mark O. Barnett, Frances O'Donnell, Jose Vasconcelos Neto, and Nedret Billor for their time and assistance during this project.

TABLE OF CONTENTS

ABSTRACT ..... **II**

DEDICATION ..... **V**

ACKNOWLEDGMENTS ..... **VI**

LIST OF FIGURES ..... **IX**

LIST OF TABLES ..... **XV**

INTRODUCTION **1**

1.1. Introduction 1

1.2. Integrating machine/deep learning methods and filtering techniques for reliable mineral phase segmentation of 3D x-ray computed tomography images 3

1.3. Image processing using machine/deep learning for mineral segmentation and surface areas analysis 4

1.4. Modeling the spatial and temporal evolution of fractured systems with heterogenous mineralogy 5

1.5. References 6

INTEGRATING MACHINE/DEEP LEARNING METHODS AND FILTERING TECHNIQUES FOR RELIABLE MINERAL PHASE SEGMENTATION OF 3D X-RAY COMPUTED TOMOGRAPHY IMAGES **13**

2.1. Introduction 14

2.2. Materials and Methods 17

2.2.1. Mancos and Marcellus Shale Samples 17

2.2.2. Sample Preparation and Image Acquisition 19

2.2.3. Classification Experiment 20

2.3. Model Evaluation 31

2.4. Results and Discussion 32

2.4.1. Comparison of the Model's Performance and the Prediction Results 32

2.4.2. Applying Trained Machine Learning and U-Net Models on an Unseen Sample 38

2.4.3. Core Segmentation and Analysis 41

2.4.4. Feature Importance 44

2.5. Conclusion 46

2.6. References 48

INTELLIGENT FRAMEWORK FOR MINERAL SEGMENTATION AND FLUID-ACCESSIBLE SURFACE AREA ANALYSIS IN SCANNING ELECTRON MICROSCOPY **54**

3.1. Introduction 55

3.2. Data and Methodology 58

3.2.1. Sandstone Samples 58
3.2.2. SEM BSE-EDS and Labeled Images 59
3.2.3. Feature Extraction 61
3.2.4. Establishing the Datasets 62
3.2.5. Pixel Wise Image Analysis and Segmentation Algorithms 64
3.2.6. Mineral/pore Quantification and Surface Area Analysis 67
3.2.7. Performance Metrics 69
3.3. Results and Discussion 69
3.3.1. Performance of the models on single and pooled datasets 69
3.3.2. Effect of input variable on the models' performance 71
3.3.3. Comparison of the Best Random Forest and U-Net Models 76
3.3.4. Mineral/pore abundance and mineral accessibility analysis 79
3.4. Conclusions 83
3.5. References 85
MODELING THE SPATIAL AND TEMPORAL EVOLUTION OF FRACTURED SYSTEMS WITH HETEROGENOUS MINERALOGY 90
4.1. Introduction 91
4.2. Data and Methodology 94
4.2.1. Sample 94
4.2.2. Reactive transport simulations 97
4.3. Results and discussion 102
4.3.1. Evolution of mineral volume fractions 103
4.3.2. Ion concentration and pH 114
4.3.3. Porosity Evolution 122
4.4. Conclusion 125
4.5. Acknowledgements 127
4.6. Reference 127
CONCLUSIONS AND CONTRIBUTION TO NEW KNOWLEDGE 134
5.1. Integrating machine/deep learning methods and filtering techniques for reliable mineral phase segmentation of 3D X-ray Computed Tomography images 134
5.2. Intelligent framework for mineral segmentation and fluid-accessible surface area analysis in Scanning Electron Microscopy 136
5.3. Modeling the Spatial and Temporal Mineral Evolution in Fractured Heterogenous System 138

LIST OF FIGURES

Figure 2.1 Marcellus and Mancos core samples were extracted and mounted on pins to scan (Carl Zeiss Microscopy Customer Center Bay Area). 20

Figure 2.2. The (workflow) schematic of mineral classification using different filters as input variables and three machine learning approaches..... 21

Figure 2.3. Representative histograms for 2D slices from Mancos and Marcellus X-ray CT images. 25

Figure 2.4. Labeled images and their corresponding phases and colors. (a) Mancos sample; (b)Marcellus sample..... 26

Figure 2.5. Overall performance of different machine learning methods and U-Net deep learning method on perdition of different phases in the Mancos dataset; (a) Overall performance of the RF model, (b) Overall performance of the FNN model, (c) Overall performance of the K-means model, (d) Overall performance of the U-Net model. 32

Figure 2.6. Overall performance of different machine learning methods and U-Net deep learning method on perdition of different phases in Marcellus dataset. (a) Overall performance of the RF model, (b) Overall performance of the FNN model, (c) Overall performance of the K-means model, (d) Overall performance of the U-Net model. 34

Figure 2.7. IOU score for the perdition of different phases for the Mancos dataset (‘0′ is organic matter, ‘1’ is the ‘Kaolinite + Dolomite + Calcite’ group, ‘2’ is background, ‘3’ is ‘Quartz + Illite/Smectite + Albite’ group, ‘4’ is pyrite). (a) IOU score for the RF model, (b) IOU score for the FNN model, (c) IOU score for the K-means model, (d) IOU score for the U-Net model..... 37

Figure 2.8. IOU score for the perdition of different phases for Marcellus dataset (‘0’ is organic matter, ‘1’ is the ‘Muscovite + Microcline + Albite +Dolomite + Quartz’ group, ‘2’ is background, ‘3’ is ‘Calcite + clay’ group, ‘4’ is pyrite). (a) IOU score for the RF model, (b) IOU score for the FNN model, (c) IOU score for the K-means model, (d) IOU score for the U-Net model. 38
Figure 2.9. Output phase segmented images using ML methods with filtering techniques and deep learning method for Marcellus sample. (a) label image, (b) FNN model using original image as input (OI), (c) RF model using original image as input (OI), (d) U-Net considering focal and dice loss as the loss function (S3), (e) FNN model using 14 extracted features as input (14F), (f) RF model using 14 extracted features as input (14F) 39
Figure 2.10. Output phase segmented images using machine learning methods with filtering techniques and deep learning method for the Mancos sample . (a) label image, (b) FNN model using original image as input (OI), (c) RF model using original image as input (OI), (d) U-Net considering focal and dice loss as the loss function (S3), (e) FNN model using 14 extracted features as input (14F), (f) RF model using 14 extracted features as input (14F). 40
Figure 2.11. The 3D view of segmented core samples;(a) Mancos and (b) Marcellus samples. 42
Figure 2.12. Grain size distribution of granular minerals within samples imaged with X-ray CT; (a) the distribution for Mancos sample, (b) the distribution for Marcellus sample. 44
Figure 2.13. The rank of the extracted features is based on their contribution to improving segmentation (vertical variables are filter names, for example, F-32 is the 32nd filter of the second convolutional layer of VGG16, and horizontal numbers are the average rank of filters called feature importance value). (a)the rank for the VGG16F extracted features; (b) the rank for the 14F extracted features. 45

Figure 3.1. a) 2D SEM BSE image of a thin section from the Paluxy formation with image resolution of 1.9 μm, and image size of 17.14 mm^2 (reproduced from *Salek et al., 2022*), b.) Mineral phase segmented image. 60

Figure 3.2. The accuracy and loss against the number of epochs for the U-Net model trained on pooled dataset. 70

Figure 3.3. Performance of U-Net deep learning (a) and Random Forest machine learning (b) models for different mineral classes in pooled dataset. 72

Figure 3.4. Visual performance of U-Net on different classes in the pooled dataset. Vertical and horizontal axes demonstrate pixel numbers with 0.71 μm resolution. 74

Figure 3.5. Visual performance of the RF model on different mineral classes in the pooled dataset. Vertical and horizontal axes demonstrate pixel numbers with 0.71 μm resolution. 75

Figure 3.6. Rank of the input variables based on their contribution to improving segmentation (horizontal numbers are the rank of the variables called feature importance value). 76

Figure 3.7. Comparison of the best performing U-Net and Random Forest models on predicting different mineral classes in pooled dataset. 77

Figure 3.8. Visual comparison of the best performing U-Net and Random Forest models for predicting different mineral classes in pooled dataset. Vertical and horizontal axes demonstrate pixel numbers with 0.71 μm resolution. 78

Figure 3.9. Ranked mineral dissolution risk assessment map for K-feldspar (rank 10) that is adjacent to rank 15 (pores) and 14 (carbonate), with 0.34 μm resolution. Rank zero shows pixels that are not on the surface of the mineral of interest. 82

Figure 4.1. Processed SEM-EDS mineral maps of the near fracture matrix. (a) shows the matrix perpendicular to the imaged fracture surface, and (b) shows the matrix parallel to the fracture (Brunhoeber et. al. 2021). 96

Figure 4.2. Diagram of the simulation system where a) corresponds to mineralogy determined from images perpendicular to the fracture, b) reflects mineralogy determined from bulk XRD analysis of the sample, and c) captures mineralogy observed in images of the matrix in a sample parallel to the fracture. 98

Figure 4.3. Simulated evolution of mineral volume fraction for the heterogenous mineralogy system defined using images perpendicular to the fracture over the first 20 days of simulation for cells one to nine. Cells 1 to 6 are representative of the fracture surface and 7 to 9 are representative of the fracture. 105

Figure 4.4. Simulated evolution of mineral volume fraction for systems with heterogenous mineralogy defined from the perpendicular images for the first 3 years simulation for cells one to nine. Cells 1 to 6 reflect the fracture surface and 7 to 9 the fracture. 106

Figure 4.5. Simulated evolution of mineral volume fraction using XRD information depicting the first 20 days simulation for cells one to nine, Cells 1 to 6 are representative of the fracture surface and 7 to 9 are representative of the fracture. 109

Figure 4.6. Simulated evolution of mineral volume fraction using XRD information depicting the first 3 years simulation for cells one to nine, where 1 to 6 are representee of fracture surface and 7 to 9 are representative of fracture. 110

Figure 4.7. Simulated evolution of mineral volume fraction using parallel images to the fracture (Matrix) depicting the first 20 days simulation for cells one to nine, where 1 to 6 are representee of the fracture surface and 7 to 9 are representative of the fracture. 112

Figure 4.8. Simulated evolution of mineral volume fraction using parallel images to the fracture (Matrix) depicting the first 3 years simulation for cells one to nine, where 1 to 6 are representee of fracture surface and 7 to 9 are representative of fracture..... 113

Figure 4.9. Simulated evolution of major ion concentrations and pH for fthe heterogenous mineralogy system defined using images perpendicular to the fracture over the first 20 days of simulation for cells one to nine. Cells 1 to 6 are representative of the fracture surface and 7 to 9 are representative of the fracture..... 116

Figure 4.10. Simulated evolution of major ion concentrations and pH for the heterogenous mineralogy system defined using images perpendicular to the fracture depicting 3 years of simulation for cells one to nine. Cells 1 to 6 are representative of the fracture surface and 7 to 9 are representative of the fracture..... 117

Figure 4.11. Simulated evolution of major ion concentrations and pH using XRD information depicting the first 20 days simulation for cells one to nine, Cells 1 to 6 are representative of the fracture surface and 7 to 9 are representative of the fracture..... 118

Figure 4.12. Simulated evolution of major ion concentrations and pH using XRD information depicting the 3 years simulation for cells one to nine, Cells 1 to 6 are representative of the fracture surface and 7 to 9 are representative of the fracture. 119

Figure 4.13. Simulated evolution of major ion concentrations and pH using parallel images to the fracture (Matrix) depicting the first 20 days simulation for cells one to nine, where 1 to 6 are representee of the fracture surface and 7 to 9 are representative of the fracture. 120

Figure 4.14. Simulated evolution of major ion concentrations and pH using parallel images to the fracture (Matrix) depicting 3 years simulation for cells one to nine, where 1 to 6 are representee of the fracture surface and 7 to 9 are representative of the fracture..... 121

Figure 4.15. Simulated porosity (%) evolution over first 20 days. 124

Figure 4.16. Simulated porosity (%) evolution over 3 years. 124

LIST OF TABLES

Table 2.1 XRD composition analysis of the shale samples (Volume percentage of minerals). ... 18

Table 2.2. Experimental conditions of the X-ray CT scanning (Zeiss Microscopy Customer Center Bay Area). ... 19

Table 2.3. Filters used to extract features and their associated kernel size and standard deviations (SD). ... 22

Table 3.1. XRD composition analysis of the samples obtained from Kocurek Industries 1, Guan2 (2012) and Soong et al.3 (2016). ... 59

Table 3.2. Labeled mineral/pore pixels for the samples. ... 61

Table 3.3. Predicted abundance and accessibility values obtained from the models and the corresponding ground truth data. ... 80

Table 4.1 Mineral volume fractions calculated from Brunhoeber et. al. (2021), specific surface area and rate constants for reactive transport simulations at reservoir condition as obtained from the literature muscovite (Oelkers et al., 2008), kaolinite (Carroll and Walther, 1990; Ganor et al., 1995), illite (Gu and Evans, 2007), K-Feldspar (Bevan and Savage, 1989), albite (Chen and Brantley, 1997), quartz (Knauss and Wolery, 1988; Brady and Walther, 1990), pyrite and dolomite (Palandri and Kharaka, 2004), and calcite (Alkattan et al., 1998). ... 96

Table 4.2. Simulated brine chemistry of the Mancos formation. ... 101

CHAPTER 1

INTRODUCTION

1.1. Introduction

Geological formations have great potential for large-scale carbon sequestration to reduce the net rate of increase in atmospheric CO_2. In these systems, CO_2 is injected into formations and mineralized through geochemical reactions. Subsurface CO_2 sequestration systems include reservoirs (mostly sandstones) which store the injected CO_2 and impermeable cap-rocks (mostly shales) which seal the reservoir. Impermeable cap-rock is a necessary component of subsurface CO_2 sequestration systems to prevent fluid migration and leakage. The presence and evolution of fractures in CO_2 sequestration systems can not only pose a risk to system integrity *(Major et al., 2019; Fitts et al., 2021; Brunhoeber and Beckingham, 2019)* but also threaten overlying groundwater resources with acidification and contamination via trace element mobilization *(Choi, 2019; Qafoku et al., 2017; Apps et al., 2010; de Orte et al., 2015)*. Previous research *(Tian, 2019; Fitts and Peters, 2013; Bensinger and Beckingham, 2022; Sabo and Beckingham, 2021)* showed that mineral dissolution and precipitation can alter the formation and caprock properties and may create or increase the formation or fracture permeability. This process, however, is complex and not well understood since mineral dissolution/precipitation reactions may enhance or reduce permeability, influenced by the distribution of reactive minerals within the porous media or on the fracture surface *(Spokas, 2019)*. Thus, it is crucial to understand the mineral composition and distribution to evaluate potential reactivity and impacts on formation and fracture properties.

Reactive transport simulations can be used to simulate the evolution of subsurface CO_2 sequestration systems including mineral reactions and porosity evolution. Micro-scale imaging is a powerful technique for mineral-pore phase characterization to parametrize reactive transport simulations. Integrating micro-scale imaging techniques, especially scanning electron microscopy-backscatter electron (SEM-BSE), energy dispersive x-ray spectroscopy imaging (EDS) and 3D X-ray Computed Tomography (CT) imaging with machine learning (ML) methods provides a powerful tool for characterization of formation properties. Imaging can also be used to analyze the changes in porosity, pore connectivity, and mineral surface area to enhance understanding of the impact of CO_2 injection on formation properties.

Machine learning methods utilize mathematical models to excavate nonlinear underlying patterns in a dataset, which helps a computer system make predictions or classifications on the dataset *(Guntoro et al., 2019; Suthaharan, 2016)*. This integrated framework can simultaneously consider several extracted features in addition to voxel attenuation/gray-scale color which could be a promising method for reliable phase segmentation and pore-mineral surface area analysis. This ability would be valuable when several phases have similar/overlapping attenuation as well as in images with spatial variations in attenuation for a given phase. In these cases, additional features of phases may be the key to individual phase segmentation *(Chauhan et al., 2016; Anderson et al., 2020)*. Within the petroleum industry, environmental and geosciences, imaging techniques, and machine learning models have been used in various applications *(Ulker and Sorgun et al., 2016; Gupta et al., 2018; Gupta et al., 2018, Saikia et al., 2020; Semnani and Borja, 2017)* but few studies have focused on mineral phase characterization *(Chauhan et al., 2016; Li et al., 2021; Karimpouli and Tahmasebi, 2019; Da Wang et al., 2020)* and none on reactive surface area analysis within SEM and X-ray CT images.

This research aims to first utilize the 2D BSE and 3D X-ray imaging and image processing techniques for mineral phase characterization, mineral surface area analysis, and informing reactive transport simulations, then to investigate the evolution of minerals and reaction rates, which are outlined in the following research question groups.

1.2. Integrating machine/deep learning methods and filtering techniques for reliable mineral phase segmentation of 3D x-ray computed tomography images

Shales are important unconventional oil reservoirs and caprocks for CO_2 storage systems. Both of these applications involve potentially reactive conditions from the presence of CO_2 where hydrocarbons can be extracted via hydraulic fracturing, which is often enhanced with the injection of CO_2, referred to as CO_2-enhanced oil recovery (CO_2-EOR) *(Yang et al., 2021).* However, only some mineral phases in the system are reactive in the associated conditions. As hydrocarbon distribution can be correlated with the inorganic and organic constituents of the formation, understanding the mineralogy and mineral distribution in these samples is also critical for assessing the gas capacity in addition to considering reactive fracture evolution. Studying mineral distribution in these formations can also help with the prediction of fracture formation as fractures may preferentially form in calcite *(Yakaboylu, 2020)* or clay-rich regions *(Brunhoeber and Beckingham, 2019; Yang et al., 2021; Yakaboylu, 2020)*. Furthermore, this can help with understanding the impacts of reactions on fracture permeability which have been noted to be influenced by the distribution of reactive minerals on the fracture surface *(Spokas, 2019)*.

Machine learning-based phase segmentation makes it possible to simultaneously consider several extracted features in addition to the voxel attenuation for a more reliable mineral phase segmentation. While there exist works at the intersection of core imaging and machine learning,

no study has yet investigated the potential improvement of phase segmentation in shale X-ray CT images using filtering techniques as additional input along with machine learning models to reliably segment different phases, which raises some questions:

- What are the specific characteristics of different mineral phases that can be extracted from 3D X-ray CT images using some filtering techniques to reliably segment mineral phases?
- Can these characteristic features be potentially used as variables to train machine learning models to automate the mineral segmentation process?

1.3. **Image processing using machine/deep learning for mineral segmentation and surface areas analysis**

Imaging is powerful means of sample characterization where mineral abundances and surface areas can be quantified from mineral maps. Pore-scale image processing and reactive transport modeling have advanced crucially through the integration of machine learning with imaging techniques (*Chen et al., 2020b; Kim et al., 2021)*. These integrated image analysis workflows can accelerate the mineral characterization of a given geological sample. The obtained parameters such as porosity, mineral composition, mineral accessible surface area data, and segmented mineral maps then can be utilized to parameterize reactive transport simulations. These data are often obtained via manual processing of collected images, which is time and resource intensive and additionally subjective to user interpretation. This study evaluates the potential of machine learning methods for pore-mineral characterization of a given sample over various image resolutions in 2D SEM images to answer the following:

- Can machine learning methods accurately segment minerals/pores in SEM images and characterize mineralogy in SEM images for a given geological sample?
- Do machine learning methods preserve geological characteristics within the images, such as connected porosity, mineral/pore roughness, and mineral surface area ratios? Is the ratio of correctly predicted pixels over total pixels (accuracy) a correct metric for a machine learning-based geochemistry image processing framework?
- What is the real performance of machine learning methods if we consider geological sample characteristics such as the connected porosity and mineral surface area, instead of pixel-wise accuracy, as a metric? Are the connected porosity and surface area analyses more valuable metrics than the pixel-wise accuracy for the geological image processing?

1.4. **Modeling the spatial and temporal evolution of fractured systems with heterogenous mineralogy**

The rapid development of subsurface organic-rich shales for hydrocarbon recovery in past years has opened up the possibility of utilizing these hydraulically fractured shale reservoirs as potential target reservoirs for CO_2 sequestration. Shales have low permeability and high sealing capacity which make them potential candidates for CO_2 sequestration given porosity is increased by artificial fracturing. Shales are also important caprocks for CO_2 storage in saline aquifers. In these formations, mineral dissolution and precipitation reactions in fractures may potentially alter fracture apertures following the injection of CO_2. Recent research studies simulated flow and transport in fractured rocks and quantified mineral dissolution rates *(Yoon et al., 2019; Li 2007; Pandey and Rajaram 2016; Deng and Peters, 2019; Yekta et al., 2021; Andrews and Navarre-Sitchler, 2021)*. However, the enhancement or reduction of fracture aperture and permeability by

mineral dissolution or precipitation on the fracture surfaces *(Deng et al., 2016; Gutierrez et al., 2000; Menefee et al., 2020)* is not well understood and the exploration of these heterogeneous domain evolutions has been relatively limited to date.

Recent work has shown fractures form preferentially in clay-rich regions such that the fracture surface mineralogy is not well reflected by the bulk mineralogy (Brunhoeber et al., 2021). This is often not accounted for in prior studies of reactive fracture evolution where no study has investigated the impact of varying multi-mineralogic fracture surface compositions on fracture surface and matrix reactions and reaction rates to better understand potential fracture aperture and permeability evolution. Implications of the clay rich region surrounding the fracture on the reactive evolution of the fracture and matrix are considered in this work via the following research questions:

- What is the relationship between fracture surface composition and the spatial and temporal evolution of minerals in heterogeneous fractured rock domains exposed to the flow of CO_2 saturated brine? What is the impact of variations in mineralogy of the fracture surface and surrounding matrix on simulated mineral reactions and reaction rates between minerals and CO_2 saturated brine?
- What is the effect of considering varying fracture surface mineral compositions on porosity evolution?

1.5. **References**

- Andrews, E., & Navarre-Sitchler, A. (2021). Temporal and spatial heterogeneity of mineral dissolution rates in fractured media. Geochimica et Cosmochimica Acta, 312, 124-138.

- Anderson, T. I., Vega, B., & Kovscek, A. R. (2020). Multimodal imaging and machine learning to enhance microscope images of shale. Computers & Geosciences, 145, 104593.
- Apps, J. A., Zheng, L., Zhang, Y., Xu, T., & Birkholzer, J. T. (2010). Evaluation of potential changes in groundwater quality in response to CO_2 leakage from deep geologic storage. Transport in Porous Media, 82(1). https://doi.org/10.1007/s11242-009-9509-8
- Brunhoeber, O. M., & Beckingham, L. E. (2019, December). Role of Mineralogy in Controlling Fracture Formation. In AGU Fall Meeting Abstracts (Vol. 2019, pp. H33N-2200).
- Brunhoeber, O. M., Anovitz, L. M., Asadi, P., & Beckingham, L. E. (2021). Role of mineralogy in controlling fracture formation. ACS Earth and Space Chemistry, 5(11), 3104-3114.
- Bensinger, J., & Beckingham, L. E. (2020). CO_2 storage in the Paluxy formation at theKemper County CO_2 storage complex: Pore network properties and simulated reactive permeability evolution. International Journal of Greenhouse Gas Control, 93. https://doi.org/10.1016/j.ijggc.2019.102887
- Chauhan, S., Rühaak, W., Anbergen, H., Kabdenov, A., Freise, M., Wille, T., & Sass, I. (2016). Phase segmentation of X-ray computer tomography rock images using machine learning techniques: an accuracy and performance study. Solid Earth, 7(4), 1125-1139.
- Choi, B. Y. (2019). Potential impact of leaking CO_2 gas and CO_2-rich fluids on shallow groundwater quality in the Chungcheong region (South Korea): A hydrogeochemical approach. International Journal of Greenhouse Gas Control, 84. https://doi.org/10.1016/j.ijggc.2019.03.010

- Da Wang, Y., Shabaninejad, M., Armstrong, R. T., & Mostaghimi, P. (2020). Physical accuracy of deep neural networks for 2D and 3D multi-mineral segmentation of rock micro-CT images. arXiv preprint arXiv:2002.05322.
- de Orte, M. R., Sarmiento, A. M., Basallote, M. D., Rodríguez-Romero, A., Riba, I., & delValls, A. (2014). Effects on the mobility of metals from acidification caused by possible CO_2 leakage from sub-seabed geological formations. Science of the Total Environment, 470–471. https://doi.org/10.1016/j.scitotenv.2013.09.095
- Deng, H., & Peters, C. A. (2019). Reactive transport simulation of fracture channelization and transmissivity evolution. Environmental engineering science, 36(1), 90-101.
- Deng, H., Molins, S., Steefel, C., DePaolo, D., Voltolini, M., Yang, L., & Ajo-Franklin, J. (2016). A 2.5D Reactive Transport Model for Fracture Alteration Simulation. Environmental Science and Technology, 50(14). https://doi.org/10.1021/acs.est.6b02184
- Fitts, J. P., Ellis, B. R., Deng, H., & Peters, C. A. (2012). Geochemical controls on fracture evolution in carbon sequestration. 46th US Rock Mechanics / Geomechanics Symposium 2012, 3.
- Fitts, J. P., & Peters, C. A. (2013). Caprock fracture dissolution and CO_2 leakage. Reviews in Mineralogy and Geochemistry. https://doi.org/10.2138/rmg.2013.77.13
- Guntoro, P. I., Tiu, G., Ghorbani, Y., Lund, C., & Rosenkranz, J. (2019). Application of machine learning techniques in mineral phase segmentation for X-ray microcomputed tomography (µCT) data. Minerals Engineering, 142, 105882.
- Gupta, I., Rai, C., Sondergeld, C., & Devegowda, D. (2018). Rock Typing in Eagle Ford, Barnett, and Woodford Formations. SPE Reservoir Evaluation & Engineering, 21(03), 654-670.

- Gupta, I., Rai, C., Sondergeld, C., & Devegowda, D. (2018). Rock typing in the upper Devonian-lower Mississippian woodford shale formation, Oklahoma, USA. Interpretation, 6(1), SC55-SC66.
- Gutierrez, M., Øino, L. E., & Nygård, R. (2000). Stress-dependent permeability of a demineralised fracture in shale. Marine and Petroleum Geology. https://doi.org/10.1016/S0264-8172(00)00027-1
- Israeli, Y., & Emmanuel, S. (2018). Impact of grain size and rock composition on simulated rock weathering. Earth Surface Dynamics, 6(2), 319-327.
- Karimpouli, S., & Tahmasebi, P. (2019). Segmentation of digital rock images using deep convolutional autoencoder networks. Computers & geosciences, 126, 142-150.
- Li, L., Peters, C. A., & Celia, M. A. (2007). Effects of mineral spatial distribution on reaction rates in porous media. Water resources research, 43(1).
- Luhmann, A. J., Tutolo, B. M., Bagley, B. C., Mildner, D. F., Seyfried Jr, W. E., & Saar, M. O. (2017). Permeability, porosity, and mineral surface area changes in basalt cores induced by reactive transport of CO 2-rich brine. Water Resources Research, 53(3), 1908-1927.
- Li, C., Wang, D., & Kong, L. (2021). Application of Machine Learning Techniques in Mineral Classification for Scanning Electron Microscopy-Energy Dispersive X-Ray Spectroscopy (SEM-EDS) Images. Journal of Petroleum Science and Engineering, 200, 108178.
- Major, J. R., Eichhubl, P., Dewers, T. A., & Olson, J. E. (2018). Effect of CO_2–brine– rock interaction on fracture mechanical properties of CO_2 reservoirs and seals. Earth and Planetary Science Letters. https://doi.org/10.1016/j.epsl.2018.07.013

- Menefee, A. H., Welch, N. J., Frash, L. P., Hicks, W., Carey, J. W., & Ellis, B. R. (2020). Rapid mineral precipitation during shear fracturing of carbonate-rich shales. Journal of Geophysical Research: Solid Earth, 125(6), e2019JB018864.
- Mouzakis, K. M., Navarre-Sitchler, A. K., Rother, G., Bañuelos, J. L., Wang, X., Kaszuba, J. P., ... & McCray, J. E. (2016). Experimental study of porosity changes in shale caprocks exposed to CO_2-saturated brines I: Evolution of mineralogy, pore connectivity, pore size distribution, and surface area. Environmental engineering science, 33(10), 725-735.
- Navarre-Sitchler, A., & Jung, H. (2017). Complex coupling of fluid transport and geochemical reaction rates: insights from reactive transport models. Procedia Earth and Planetary Science, 17, 5-8.
- Noiriel, C., Luquot, L., Madé, B., Raimbault, L., Gouze, P., & van der Lee, J. (2009). Changes in reactive surface area during limestone dissolution: An experimental and modelling study. Chemical Geology, 265(1-2), 160-170.
- Pandey, S., & Rajaram, H. (2016). Modeling the influence of preferential flow on the spatial variability and time-dependence of mineral weathering rates. Water Resources Research, 52(12), 9344-9366.
- Qafoku, N. P., Lawter, A. R., Bacon, D. H., Zheng, L., Kyle, J., & Brown, C. F. (2017). Review of the impacts of leaking CO_2 gas and brine on groundwater quality. In Earth-Science Reviews (Vol. 169). https://doi.org/10.1016/j.earscirev.2017.04.010
- Qin, F., & Beckingham, L. E. (2019). Impact of image resolution on quantification of mineral abundances and accessible surface areas. Chemical Geology, 523, 31-41.

- Sabo, M. S., & Beckingham L. E. (2021). Porosity-permeability evolution with simultaneous mineral dissolution and precipitation. Water Resources Research, 56, e2020WR029072. https://doi.org/10.1029/2020WR029072
- Saikia, P., Baruah, R. D., Singh, S. K., & Chaudhuri, P. K. (2020). Artificial Neural Networks in the domain of reservoir characterization: a review from shallow to deep models. Computers & Geosciences, 135, 104357.
- Semnani, S. J., & Borja, R. I. (2017). Quantifying the heterogeneity of shale through statistical combination of imaging across scales. Acta Geotechnica, 12(6), 1193-1205.
- Spokas, K., Fang, Y., Fitts, J. P., Peters, C. A., & Elsworth, D. (2019). Collapse of reacted fracture surface decreases permeability and frictional strength. Journal of Geophysical Research: Solid Earth, 124(12), 12799-12811.
- Suthaharan, S. (2016). Machine learning models and algorithms for big data classification. Integr. Ser. Inf. Syst, 36, 1-12.
- Tian, H., Xu, T., Zhu, H., Yang, C., & Ding, F. (2019). Heterogeneity in mineral composition and its impact on the sealing capacity of caprock for a CO 2 geological storage site. Computers and Geosciences. https://doi.org/10.1016/j.cageo.2019.01.015
- Ulker, E., & Sorgun, M. (2016). Comparison of computational intelligence models for cuttings transport in horizontal and deviated wells. Journal of Petroleum Science and Engineering, 146, 832-837.
- Yang, H., Zhao, Y., Zhang, X., Liu, G., Du, X., Shang, D., ... & Tu, H. (2021). Supercritical CO_2 fracturing with different drilling depths in shale. Energy Sources, Part A: Recovery, Utilization, and Environmental Effects, 1-20.

- Yakaboylu, G. A., Gupta, N., Sabolsky, E. M., & Mishra, B. (2020). Mineralogical characterization and strain analysis of the Marcellus shales. International Journal of Rock Mechanics and Mining Sciences, 130, 104345.
- Yang, Y., Bruns, S., Stipp, S. L. S., & Sørensen, H. O. (2018). Impact of microstructure evolution on the difference between geometric and reactive surface areas in natural chalk. Advances in Water Resources, 115, 151-159.
- Yekta, A., Salinas, P., Hajirezaie, S., Amooie, M. A., Pain, C. C., Jackson, M. D., ... & Soltanian, M. R. (2021). Reactive transport modeling in heterogeneous porous media with dynamic mesh optimization. Computational Geosciences, 25(1), 357-372.
- Yoon, H., Ingraham, M. D., Grigg, J., Rosandick, B., Mozley, P., Rinehart, A., ... & Dewers, T. (2019). Impact of Depositional and Diagenetic Heterogeneity on Multiscale Mechanical Behavior of Mancos Shale, New Mexico and Utah, USA.

CHAPTER 2

INTEGRATING MACHINE/DEEP LEARNING METHODS AND FILTERING TECHNIQUES FOR RELIABLE MINERAL PHASE SEGMENTATION OF 3D X-RAY COMPUTED TOMOGRAPHY IMAGES

Parisa Asadi and Lauren E. Beckingham

Department of Civil and Environmental Engineering, Auburn University, Auburn, AL 36849

Published in Energies 2021, 14, 4595. https://doi.org/10.3390/en14154595

Abstract

X-ray CT imaging provides a 3D view of a sample and is a powerful tool for investigating the internal features of porous rock. Reliable phase segmentation in these images is highly necessary but, like any other digital rock imaging technique, is time-consuming, labor-intensive, and subjective. Combining 3D X-ray CT imaging with machine learning methods that can simultaneously consider several extracted features in addition to color attenuation, is a promising and powerful method for reliable phase segmentation. Machine learning-based phase segmentation of X-ray CT images enables faster data collection and interpretation than traditional methods. This study investigates the performance of several filtering techniques with three machine learning methods and a deep learning method to assess the potential for reliable feature extraction and pixel-level phase segmentation of X-ray CT images. Features were first extracted from images using well-known filters and from the second convolutional layer of the pre-trained VGG16, a convolution neural net (CNN) architecture. Then, K-means clustering, Random Forest, and Feed

Forward Artificial Neural Network methods, as well as the modified U-Net model, were applied to the extracted input features. The models' performances were then compared and contrasted to determine the influence of the machine learning method and input features on reliable phase segmentation. The results showed considering more dimensionality has promising results and all classification algorithms result in high accuracy ranging from 0.87 to 0.94. Feature-based Random Forest demonstrated the best performance among the machine learning models, with an accuracy of 0.88 for Mancos and 0.94 for Marcellus. The U-Net model with the linear combination of focal and dice loss also performed well with an accuracy of 0.91 and 0.93 for Mancos and Marcellus, respectively. In general, considering more features provided promising and reliable segmentation results that are valuable for analyzing the composition of dense samples, such as shales, which are significant unconventional reservoirs in oil recovery.

2.1. **Introduction**

Shales are important unconventional oil reservoirs. In these low permeability formations, hydrocarbons can be extracted using hydraulic fracturing, often enhanced with the injection of CO_2 referred to as CO_2-enhanced oil recovery (CO_2-EOR) *(Yang et al., 2021)*. As hydrocarbon distribution can be correlated with the inorganic and organic constituents of the formation, understanding the mineralogy and mineral distribution in these samples is critical for assessing the gas capacity. Studying mineral distribution in these formations can also help with the prediction of fracture formation and hydrocarbon recovery as fractures may preferentially form in calcite *(Yakaboylu et al., 2020)* or clay-rich regions *(Yakaboylu et al., 2020; Brunhoeber et al., 2022; Yoon et al., 2019)*. In CO_2-EOR systems, fracture aperture may be dynamic as minerals dissolve and precipitate following CO_2 injection. This process, however, is complex and not well

understood where reactions may enhance or reduce fracture permeability, influenced by the distribution of reactive minerals on the fracture surface *(Spokas et al., 2019; Iloejesi and Beckingham, 2021)*.

X-ray computed tomography (X-ray CT) is a powerful means of imaging that can facilitate the 3D non-destructive characterization of geologic samples. While historically high-resolution X-ray CT imaging of samples was only possible using synchrotron sources, advancements in the development of laboratory and benchtop instruments have broadened access to high-resolution X-ray CT imaging in the form of X-ray micro- and nano-computed tomography (X-ray nano CT) instruments. These X-ray CT instruments can provide a three-dimensional (3D) depiction of an object with high resolution (up to 100 nanometers) with a relatively large field of view (FOV) compared to other 3D imaging techniques *(Goral et al., 2020)*. This scale of information is typically only widely available in the laboratory using 2D imaging approaches such as scanning electron microscopy (SEM). 3D X-ray CT imaging, however, offers an additional depth of information that is not available with 2D-based microscopy analysis *(Guntoro et al., 2019)*. This can facilitate the analysis of the 3D nature of the sample, such as pore size distribution and connectivity *(Bensinger and Beckingham, 2020)*. The use of 3D X-ray CT imaging instead of 2D imaging also eliminates stereological errors generated by conventional 2D microscopy analysis used for porous media samples, allowing more accurate analysis of the samples ((*Guntoro et al., 2019;* Guntoro et al., 2019).

X-ray CT images consist of voxels of varying grayscale intensity correlated to the X-ray attenuation of the material. Variations in attenuation result due to differences in material properties including density and atomic number. Traditional image processing and segmentation rely on the similarity or intensity (or both) of the pixels to delineate the boundaries of the objects (*Chen et al.,*

2020). Segmentation of images by attenuation can facilitate quantitative image processing of sample properties and characteristics including porosity, surface area, and mineral volume fractions *(Landrot et al., 2012; Qin and Beckingham, 2019; Anjikar et al., 2020)*. It should be noted, however, that not all mineral phases can be segmented using attenuation alone due to close or overlapping x-ray attenuation coefficients and partial volume effects *(Chauhan et al., 2016; Cnudde and Boone, 2013; Wildenschild, 2013)*. In addition, beam hardening can make the grayscale attenuation of a given phase differ depending on the location of the phase within the sample *(Guntoro et al., 2019)*, especially in the borders of the images. This is particularly noted in dense samples such as shale cores. These challenges make image segmentation, even into groups of minerals with similar attenuations, time-consuming, labor intensive, and subjective. One practical alternative is utilizing some advanced techniques such as machine learning.

Machine learning methods utilize mathematical models to excavate nonlinear underlying patterns in a dataset, which helps a computer system make predictions or classifications on the dataset *(Guntoro et al., 2019; Suthaharan, 2016)*. Within the petroleum industry and geosciences, machine learning models have been used in various applications, such as fluid transport analysis *(Ulker and Sorgun, 2016)*, rock typing *(Gupta et al., 2018; Gupta et al., 2018)*, reservoir characterization *(Saikia, 2020)*, and multiscale imaging to quantify properties of shale source rocks *(Semnani and Borja, 2017)*, as well as phase segmentation *(Li et al., 2021)* of SEM images of a shale. A few studies have even focused on segmenting different mineral phases within X-ray CT images using machine learning *methods (Guntoro et al., 2019; Guntoro et al., 2019; Chauhan et al., 2016; Anderson et al., 2020; Karimpouli and Tahmasebi, 2019; Da Wang et al., 2002)*. However, the effectiveness and reliability of machine learning methods to differentiate, quantify

and extract features from X-ray CT images of shales are not well understood but could provide a valuable approach to image processing in the petroleum and geosciences field.

Machine learning-based phase segmentation makes it possible to simultaneously consider several extracted features in addition to the voxel attenuation for a more reliable phase segmentation. This ability would be valuable when several phases have similar/overlapping attenuation as well as in images with spatial variations in attenuation for a given phase. In these cases, additional features of phases may be key to individual phase segmentation (*Chauhan et al., 2016; Anderson et al., 2020)*. While there exist works at the intersection of core imaging and machine learning, no study has yet investigated the potential improvement of phase segmentation in shale X-ray CT images using filtering techniques, as additional input, along with machine learning models to reliably segment different phases. This study investigates the performance of several filtering techniques with three machine learning methods and one deep learning method to assess the potential for reliable feature extraction and pixel-level phase segmentation of a Marcellus and a Mancos shale. This study will help geologists to obtain the different distinguishable phases in 3D X-ray CT images to provide practical techniques for reliable phase segmentation. To our knowledge, it is the first time that the task of distinguishing mineral phases of 3D X-ray CT images is integrated through both pixel-level classifications using machine learning models along with filtering techniques and image segmentation methods using a deep learning model on shale samples.

2.2. **Materials and Methods**

2.2.1. Mancos and Marcellus Shale Samples

Shale core samples 1” in diameter and 2” in length from the Marcellus and Mancos formations obtained from Kocurek Industries were used in this work. The Marcellus shale is an organic-rich shale formation in the northeastern US *(Gihm et al., 2011)*. According to the U.S. Geological Survey (USGS) assessment, the Marcellus Shale contains about 84 trillion cubic feet and 3.4 billion barrels of undiscovered, technically recoverable natural gas and natural gas liquids, respectively. The Mancos shale formation is in the Midwestern US and is a major source of rock for oil and/or gas in the Rocky Mountain Region. It is also estimated that Mancos contains 66.3 trillion cubic feet of shale gas, 74 million barrels of shale oil, and 45 million barrels of natural gas liquids in addition to some unproved and undiscovered recoverable resources based on the U.S. Geological Survey *(Hawkins et al., 2016)*.

The mineralogical analysis obtained by X-Ray Diffraction (XRD) analysis in *(Brunhoeber et al., 2022)* is listed in Table 2.1. The Marcellus shale is predominantly calcite, quartz, and pyrite. It should be noted that the clay minerals were not detected in XRD. This indicated their minor concentrations with respect to the major calcite phase. The Mancos formation has a larger variation in mineralogy and is 57.63% quartz with approximately equal clay (Muscovite and Kaolinite), carbonate (dolomite and calcite), and feldspar (microcline and albite) fractions, and minor pyrite.

Table 2.1 XRD composition analysis of the shale samples (Volume percentage of minerals).

Sample/ Mineral	Quartz	Pyrite	Calcite	Muscovite	Kaolinite	Microcline	Albite	Dolomite
Mancos	57.63	0.22	6.88	9.68	3.37	7.45	8.11	6.66
Marcellus	2.97	0.33	96.70					

2.2.2. Sample Preparation and Image Acquisition

Sub-samples for each formation were extracted from 1" core sample for high-resolution X-ray CT imaging by Carl Zeiss Microscopy Customer Center Bay Area (Pleasanton). 0.8 mm × 1 mm sections were milled from the top 5mm of each core sample using a laser and mounted on pins (Figure 2.1). X-ray CT images of each sample were then collected using an Xradia 620 Versa (Zeiss Microscopy Customer Center Bay Area). The sample scan parameters are shown in Table 2.2 where the X-ray energy of 60 kV was utilized to provide better imaging of the less dense features of the sample (*Anderson et al., 2020*). Almost all parameters are the same for both samples, only the filter and exposure time are different. Projections were reconstructed using the Reconstructor Scout-and-Scan Control System software and exported as TXM and tiff format files. The resulting images are used in this study.

Table 2.2. Experimental conditions of the X-ray CT scanning (Zeiss Microscopy Customer Center Bay Area).

Sample Name	Marcellus	Mancos
Voltage	60 kV	60 kV
Power	10 W	10 W
No. of projections	2201	2201
Spatial resolution	0.8 μm	0.8 μm
Bin	2	2
Objective	20×	20×
Filters	LE4	LE2
Exposure time	20 s	9 s

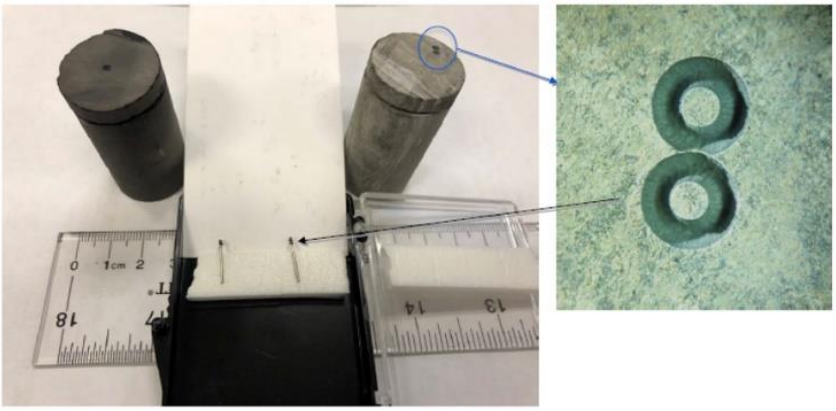

Figure 2.1 Marcellus and Mancos core samples were extracted and mounted on pins to scan (Carl Zeiss Microscopy Customer Center Bay Area).

2.2.3. Classification Experiment

This study explored mineral phase segmentation in X-ray CT images of shale samples using machine/deep learning with filtering techniques to provide image features as additional inputs. Figure 2.2 shows the experimental design. The workflow includes defining input variables from cross-sectional slices of the original X-ray CT images, followed by machine learning and deep learning for phase segmentation. The machine learning section in the workflow of the study included three parts (three different sets of input images), each of which considered different extracted features as the input data for the machine learning methods. These stacked input variables were introduced to the Random Forest (RF), K-means clustering (K-means), Feed Forward Neural network (FNN), and the U-Net deep learning models to train and evaluate their computational performance and accuracy. Each machine learning model was trained and cross-validated for each sample using the 78,018,066-pixel data (81 × 994 × 969 pixels). For the deep learning method, data augmentation was also applied to increase the amount of data by augmenting images including flipping, zooming, shifting, and rotation. The associated images were cropped to 128 × 128-pixel size images to be used for the U-Net deep learning method. After data augmentation, 11,000 slices with 128 × 128-pixel size were provided.

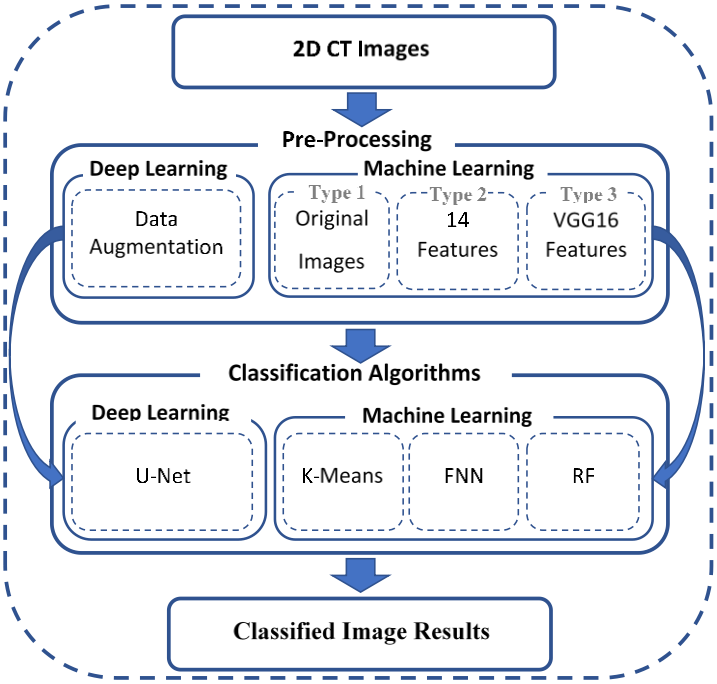

Figure 2.2. The (workflow) schematic of mineral classification using different filters as input variables and three machine learning approaches.

2.2.3.1. Image Processing and Feature Extraction

Mineral phases can have distinguishable features in images, such as texture and grain size. In feature-based classification, images can be represented in additional dimensions (i.e., extracted feature images) which helps to better explore the similarities and differences of different phases to classify phases in separate classes. In this study, different types of features were extracted from the 2D cross-sectional slices of X-ray CT images, and phase classification was performed leveraging these features in addition to attenuation values. Two different feature extraction strategies were utilized (Figure 2.2) to create feature maps, which are briefly discussed in the following sections.

Filtering Techniques

Filters were applied to both Mancos and Marcellus images using the OpenCV *(Bradski, 2008)* and Scikit-image *(Van der Walt., 2014)* filters in Python to provide feature maps representative of texture, grain size, edges, entropy, and abnormality, as well as color attenuation. Several well-known filters, including Gaussian, Median, Sobel (45 degrees, vertical and horizontal), and Gabor (Table 2.3), were used. Each filter convolutes the original image to perform specific tasks such as blurring (e.g., the Gaussian filter), edge detection, or texture extraction (e.g., the Gabor and Sobel filters). For example, the Gaussian filter convolutes the image using specific standard deviations (σ), creating feature maps in different scales. Filtered images with higher standard deviations (more blurred) lose details of smaller grains while those with smaller standard deviations preserve more features from the smaller grains. The difference in the two images provides new information that can be also used as input variables to the machine learning models. In this work, edge features and textures were extracted using Sobel and Gabor filters (horizontal and vertical), while blobs and corners were extracted with a difference of Gaussians, the determinant of the Hessian matrix, and Laplacian filters.

Table 2.3. Filters used to extract features and their associated kernel size and standard deviations (SD).

Filter Name	Kernel Size	SD	Task	Abbreviation
Median	3 × 3	-	denoising and integrating phases	-
Gaussian	3 × 3	1	denoising and integrating phases	-
Difference of Gaussians 1-10	3 × 3	1, 10	Detecting smaller features	DoG 1-10
Difference of Gaussians 1-5	3 × 3	1, 5	Detecting smaller features	DoG 1-5
Difference of Gaussians 2-5	3 × 3	2, 5	Detecting smaller features	DoG 2-5
Difference of Gaussians 1-2	3 × 3	1, 2	Detecting smaller features	DoG 1-2
Sobel (45 degrees)	3 × 3	-	Detecting edges and textures	Sobel-45
Sobel (Vertical)	3 × 3	-	Detecting edges and textures	Sobel-V
Sobel (Horizontal)	3 × 3	-	Detecting edges and textures	Sobel-H
Laplace	3 × 3	-	Detecting blobs and edges	-
Difference of Hessians	3 × 3	3, 5	Detecting blobs and corners	DoH
Gabor (Horizontal)	3 × 3	-	Detecting textures	Gabor-H
Gabor (Vertical)	3 × 3	-	Detecting textures	Gabor-V

Extracting Filters from a Deep Convolutional Layer

One promising technique for feature extraction is applying pre-trained filters obtained from a trained deep-learning model. In this study, the trained filters obtained from the second convolutional layer of the first block in the visual geometry group (VGG16) network *(Ronneberger et al., 2015)* were applied to extract image features. The VGG16 convolutional neural network is widely used in a wide variety of fields because of its high generalization capability, simple structure, and accuracy where is it among the top-5 of models tested on ImageNet, a dataset of over 14 million images belonging to 1000 classes *(Ronneberger et al., 2015)*. As a result, the VGG16 network has learned a rich array of feature representations for a wide range of images. Here, features were extracted from X-ray CT images using the second convolutional layer of the first block of VGG16 with 64 filters. This layer was selected since it is the deepest layer of VGG16 which its output feature images will have the same size as the original input CT images. As a result, same-size feature images were provided. In this study, the filters of this block were applied to each X-ray CT slice to extract features for machine learning models.

2.2.3.2. Image Segmentation and Labeling

Segmentation refers to the grouping of pixels into several classes by identification and isolation of pixels that have the same features into a single category. The most common segmentation method is based on the histogram analysis of grayscale intensities of the pixels in the image which provides the distribution of the grayscale level of each pixel in the image. In X-ray CT images, this provides a relative identification of the different phases contained in the image. Figure 2.3 shows the histograms of gray intensities for a 2D slice from the Mancos and Marcellus datasets. The two peaks indicate a clear threshold value for separating two classes, which in this case are the background (left peak which has zero intensity) and the sample (right peak). Further segmentation and phase labeling were carried out manually based on knowledge of phases in the sample (their attenuation grayscale, texture, and size characteristics) and characteristics of these phases from processed SEM, BSE, and EDS images in prior work *(Brunhoeber et al., 2022)* and XRD data (Table 2.1). Figure 2.4 shows an example of labeled images and their corresponding colors and phases (Furthermore, readers are referred to 3D view videos (S1 to S6) of both samples in the Supplementary Material which show the samples and segmented mineral phases). For example, in the Marcellus sample, phases were considered as grains (mostly quartz), matrix (which was mostly calcite and clays), pyrite, organic matter, and background. Labels were assigned by manually segmenting, correcting, and post-processing of 2D slices. In total, 81 2D slices (994 × 969-pixel images, i.e., 78,018,066 pixels in total) from the X-ray CT image were segmented, in which, 60 labeled X-ray CT images were used to train the classifiers and the 21 images used to evaluate the performance of trained models.

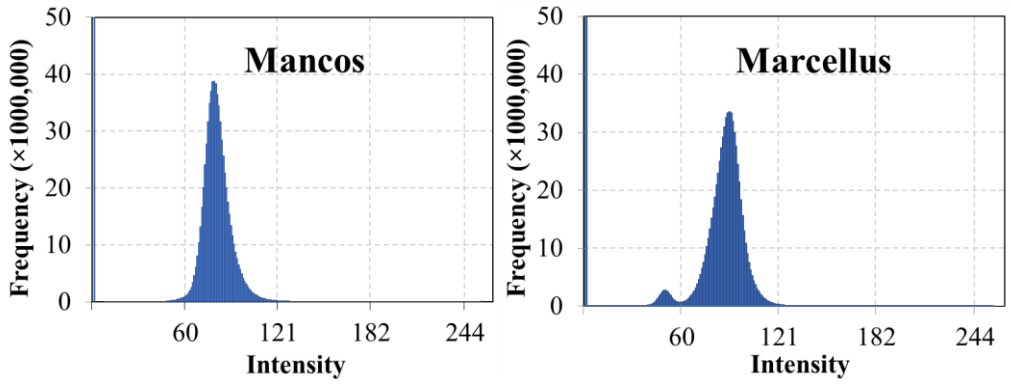

Figure 2.3. Representative histograms for 2D slices from Mancos and Marcellus X-ray CT images.

2.2.3.3. Machine Learning

Machine learning algorithms rely on sets of features to train the classification models. Once trained, models can be used to identify features in an unknown dataset and group them into respective classes. Machine learning methods in general fall into unsupervised and supervised categories. Here, three classification machine learning algorithms are implemented. Of these, k-means is unsupervised, while RF and Feed Forward Artificial Neuron Networks are non-linear supervised classification algorithms. The theories and parameters for the considered algorithms are briefly described in this section.

K-Means Clustering

K-means clustering partitions a collection of data into a k number group of data to make respective clusters. It then calculates the k centroid and assigns each point to the cluster with the nearest centroid from the respective data point *(Dhanachandra et al., 2015)*. There are several ways of calculating the similarities between pixels, in this study we used Euclidean distance to define the most similar centroid. Once the grouping is done it recalculates the new centroid for each cluster and a new Euclidean distance between each center and each data point to assign the points in the cluster with minimum Euclidean distance. As such, K-means is an iterative algorithm in which it

minimizes the sum of distances from each object to its cluster centroid *(Dhanachandra et al., 2015)*.

Here, K-means clustering was implemented using the Scikit-learn library *(Pedregosa et al., 2011)* in python. The K was considered 3 to 9 to find the best (k = 5) number of clusters. In addition, the epoch varied from 100 to 1000, the initialization method was set to "K-means++" to speed up the algorithm convergence. The "n-initint" was set to 10 and the best results were kept, "n-jobs" was set to -1 for parallel computation, and the algorithm was set to "Elkan".

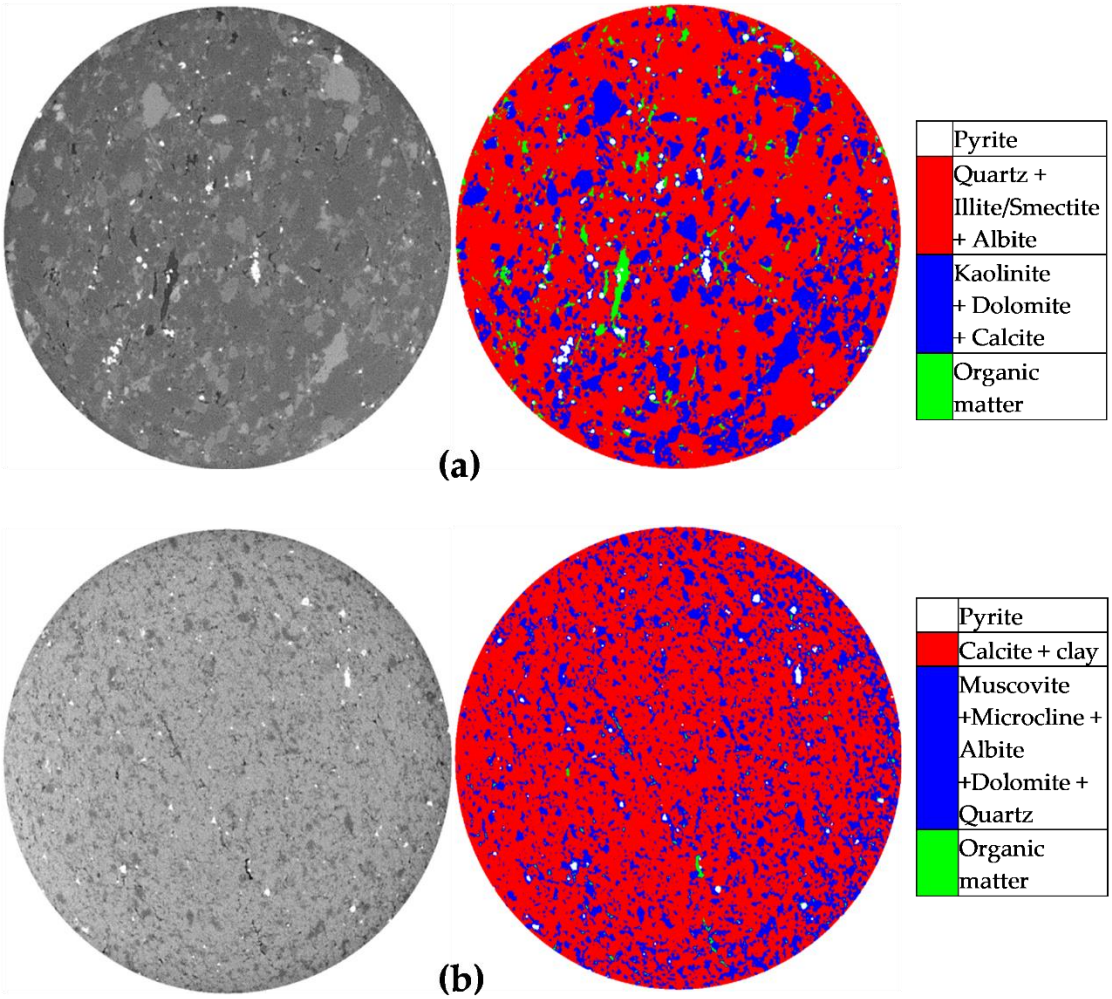

Figure 2.4. Labeled images and their corresponding phases and colors. (a) Mancos sample; (b)Marcellus sample.

Random Forest

Random Forest (RF) *(Breiman, 2001)* is an ensemble learning method for classification and regression consisting of multiple individual trees. In the training step, observations are randomly sampled from the training dataset to build an individual classification/regression tree and the best feature to split a node is selected within a randomly picked subset of features to further add randomness to the system. This process is repeated for a certain number of trees (ntree) and different randomly selected sets of input features (mtry). The overall goal of the process is to decrease the variance and improve the training accuracy. Then, the predictions are made for the remaining observations based on a weighted vote across all trees. The hierarchical structure of RF makes it an appealing method for phase segmentation where the data are largely imbalanced (i.e., some phases have more frequency than minority classes).

In this study, the RF model was implemented using the "Random Forest" Scikit-learn library *(Pedregosa et al., 2011)*. In the first run, a forest of 100 random trees was created (i.e., ntree = 100); each tree had unlimited depth and was grown without pruning. At each node, m input variables (estimated as the square root of the numbers of predictors, i.e., mtry ≈ 4 for type2 input variables and mtry ≈ 8 for type3) were randomly selected among all input variables to train the model. In this study, only two main hyperparameters, ntree and mtry, were fine-tuned using random search, and the depth of the tree remained as the default settings in the RF classifier in the Scikit-learn library. Then the random search *(Feurer et al., 2015)* was applied to fine-tune the hyperparameters of RF (i.e., mtry and ntree) by grid searching between the number of trees in the range of 100 to 700 trees and the number of randomly selected input variables at each split (i,e, mtry) in the range of 2 to 8, resulting in the final forest with ntree = 200 and mtry = 2 in each node for type2 variable inputs and ntree = 300 and mtry= 2 for type3 variable inputs.

Feed Forward Neural Network

Feed Forward Neural Networks can learn and model non-linear and complex relationships, which makes them a compelling approach for phase segmentation since high non-linearity can exist among input features and the target classes. A network consists of an input layer, hidden layers, and a layer of output neurons with multiple activated perceptrons stacked together and associated weights and biases. Adjacent layers are fully connected, and results obtained from each layer are fed into the next layer through a non-linear transformation called an activation function. Neurons of the input layer receive the input features, process them, and pass the processed information through the hidden layers to the last layer. The output of the last layer adjusts based on the predefined loss function using backward propagation by changing the weights and biases. Thus, the network trains by adjusting the weights to predict the correct class label of the given inputs for the classification task.

In this study, we used a shallow Feed Forward Neural Network as it was easier to be trained and fine-tuned on a small dataset. Based on the recommendations of previous studies *(Heaton et al., 2015; Hart et al., 2019)*, several structures were randomly selected and tested, including one or two hidden layers with a various number of neurons (i.e., 2 × 14 and 2 × 64, for type 2 and type 3 input variables, respectively), and their corresponding performance compared. For the type 1 input variable, the best number of hidden neurons was 32. Finally, a three-layer neural network with a single hidden layer consisting of a two × number of input neurons was selected as the hidden units.

TensorFlow library *(Abadi et al., 2016)* was used to develop the Feed Forward Neural networks. For this study, the input layer consisted of N neurons, which corresponds to the number

of input features, and the output layer included M neurons, which is the number of segmented phases in each sample, with a SoftMax activation function. A single hidden layer consisting of K neurons was selected as the hidden units. For example, the input layer consisted of 14 neurons for type 2 variable inputs and 64 for type 2 variable inputs, each corresponding to one of the selected input variables, which was connected to the hidden layer through a rectified linear unit (ReLU) activation function. In addition, each output neuron represented a distinct phase identified by having maximum probability obtained from a SoftMax activation function. The Categorical cross-entropy and focal loss and dice functions were considered as loss functions to adjust weights and biases, and Adam (adaptive moment estimation) was selected as the optimizer. We also used early stopping callbacks to avoid overfitting. Fine-tuning was carried out using a fine-tuning function in the TensorFlow library where the numbers of epochs varied from 100 to 1000 and the learning rate (LR) from 10−6 to 100 (the best LR was 0.0001).

2.2.3.4. Deep Learning Model (U-Net)

U-Net is a fully connected Convolutional Neural Network (CNN) method that was initially developed for biomedical image segmentation by *(Ronneberger et al., 2015)*. It is comprised of two main sections: an encoder and a decoder. The encoder contains several blocks which take an input and apply two convolutional kernels of 3 × 3, followed by a rectified linear transformation (ReLU) and a max-pooling operation with a stride of 2 × 2. The reduced spatial information with increased feature channels in the encoder path allows the network to learn the complex structure effectively due to propagating context information to the higher dimension. The decoder section consists of several expansion blocks, each of which passes the input to two convolutional layers followed by a 2 × 2 up-sampling layer. To maintain symmetry, the channels in the CNN layers are

cut into half after applying each block. In the decoder, the size of the image gradually increases, and the depth gradually decreases. Finally, the last layer feature maps pass through a 1 × 1 CNN layer with M feature maps where M is the same as the number of classes desired.

Here, 2D slices from the original X-ray CT images and their corresponding segmented maps were used to train the network. The focal (equation 1) and dice loss (equation 2) functions were applied, along with categorical cross-entropy as a loss function to adjusted weights and biases, and their performance to training a multi-class classifier model was compared. The focal loss function is designed to address the class imbalance by down-weighting easy classes such that their contribution to the total loss is small even if their number is large. Thus, it focuses on training a sparse set of hard classes.

$$\text{Focal Loss}(p_t) = -\alpha_t(1-p_t)^{\gamma}\, log(p_t) \quad (1)$$

where Pt is the probability of a given class, $\gamma > 0$, and when $\gamma = 1$ focal loss works like cross-entropy loss function, and α range from [0, 1]. In this study, $\gamma = 2$ had the best performance and α was set to 1. Dice loss based on *(Dice, 1945; Sorensen, 1948)* has also been adapted as a loss function:

$$\text{Dice Loss}\left(Y;\, Y_p\right) = 1 - \frac{\left(2 \times Y \times Y_p + 1\right)}{\left(Y + Y_p + 1\right)} \quad (2)$$

where Y is labeled data and Y_p is predicted values. Adam (adaptive moment estimation) was selected as the optimizer, and similar to Feed Forward Neural network, early-stopping was used to prevent overfitting. In addition, fine-tuning was applied using the fine-tuning function in the TensorFlow library where the number of epochs varied from 100 to 1000 (epoch = 500 was the best one), and the learning rate (LR) from 10^{-6} to 10^{0} (LR = 0.0001 was the best one). Note that the datasets were normalized into an array with an interval of [0, 1] so that the models can perform faster.

2.3. **Model Evaluation**

To evaluate the prediction performance and the trained models, the multiclass version of the F1-score, Intersection over Union or overall goodness-of-fit (IOU), and overall accuracy of each method were determined and compared. Model evaluation was carried out using the test image set against the ground truth images. The F1-score based on *(Dice, 1945; Sorensen, 1948)* is identified as:

$$\text{F1} = \frac{2\times Precision \times Recall}{(Precision + Recall)} \quad (3)$$

$$\text{Precision} = \frac{TP}{(TP + FP)} \quad (4)$$

$$\text{Recall} = \frac{TP}{(TP + FN)} \quad (5)$$

where *TP* is true positive prediction, *FP* is false positive prediction, and *FN* is false-negative prediction. To calculate the multiclass version of the F1-score, each class was considered individually as the positive class, with the other classes considered as negative classes, to get the binary F1-score for all classes. Then, the multiclass F1-score was calculated by averaging the binary F1-scores of all classes.

IOU evaluates the overlap of the predicted test image set and the ground truth images using the following equation:

$$\text{IOU} = \frac{Area\ of\ overlap}{Area\ of\ union} \quad (6)$$

In addition, Overall accuracy was calculated based on the total number of true predicted values over the total number of pixels.

2.4. **Results and Discussion**

2.4.1. Comparison of the Model's Performance and the Prediction Results

This section compares and contrasts the performance of all models. Figures 2.5 and 2.6 show the test performance of pixel-wise phase segmentation of all the models with 21 stacked 2D image slices (994 × 969 pixels) that were randomly chosen from the 3D X-ray CT image stack. All three machine learning methods (RF, FNN, and K-means) were trained and tested on the original dataset (OI), 14 extracted features (14F), and 64 extracted features (VGG16F). The latter was obtained from pre-trained filters of the convolutional layer of VGG16 architecture.

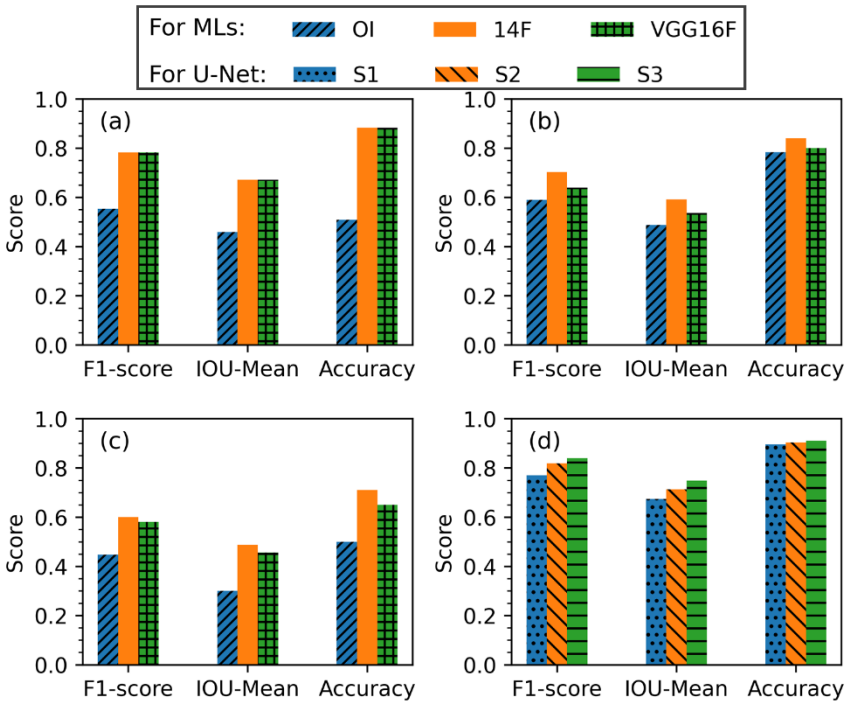

Figure 2.5. Overall performance of different machine learning methods and U-Net deep learning method on perdition of different phases in the Mancos dataset; (a) Overall performance of the RF model, (b) Overall performance of the FNN model, (c) Overall performance of the K-means model, (d) Overall performance of the U-Net model.

In addition, the U-Net model was trained with different loss functions (i.e., categorical cross-entropy, focal and dice losses). Focal and dice losses were added to improve the prediction of minority phases in addition to preserving the accuracy of the majority classes. In the first scenario (S1) for the U-Net model, loss and metric were set to the defaults of the original U-Net method (i.e., categorical cross-entropy as loss function and accuracy as a metric). For the second scenario (S2), the metric was set to mean IOU and F1-scores, and the loss function was set to focal loss. The linear combination of focal and dice loss (dice loss + 2 × focal loss) was set as a loss function for the third scenario (S3), and the metric was similar to S2. To select the best coefficient for focal and dice losses in the third scenario (S3), several coefficients were implemented using random search. The linear combination of loss functions (coefficient = 1 for dice loss and coefficient = 2 for focal loss) showed the highest IOU, F1-score, and accuracy. In addition, the class weights for dice loss were obtained based on the fraction of each class with respect to the total number of pixels, which reduced the influence of the imbalance dataset on the models' performance.

As shown in Figures 2.5 and 2.6, using only the original image (OI) as input, the accuracy of the machine learning models was less than that for feature-based machine learning image segmentation (i.e., 14F and VGG16F) for both Mancos (Figure 2.5) and Marcellus (Figure 2.6) datasets. Considering IOU and F1-score, which includes a weighted prediction precision for each class, reveals that using only the original image (OI) for phase segmentation is not reliable and including more input features might result in a more robust pre-diction. Figure 2.6 also indicates all machine learning models achieved a decent accuracy with 14F inputs outperforming the OI and VGG16F.

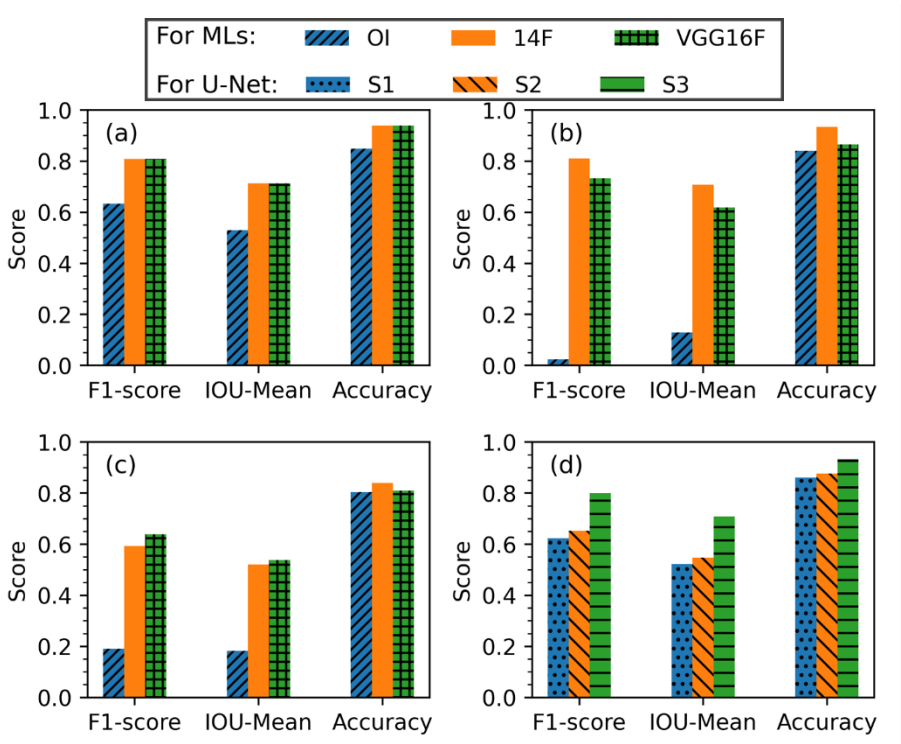

Figure 2.6. Overall performance of different machine learning methods and U-Net deep learning method on perdition of different phases in Marcellus dataset. (a) Overall performance of the RF model, (b) Overall performance of the FNN model, (c) Overall performance of the K-means model, (d) Overall performance of the U-Net model.

This higher performance for 14F can be attributed to the fact that many filters were examined visually, and the top 14 filters were selected for the segmentation task. These results demonstrate the importance of feature engineering and also selecting the top features for the machine learning classification tasks. The obtained results are in good agreement with the previous study conducted by *(Chauhan et al., 2016)* on X-ray images of several sand-stone samples which showed the accuracy of machine learning methods was largely affected by feature vector selection and was improved by utilizing more features obtained from some filtering techniques.

Among machine learning models implemented on both datasets (Figures 2.5 and 2.6), the RF model outperformed other methods in terms of accuracy, IOU, and F1-scores. On the other hand, K-means achieved the lowest performance on this dataset since it is an unsupervised model which may not perform well on noisy data due to spatial variations in attenuation of a given phase,

especially near the borders of the X-ray CT images. The U-Net (U-Net, S3) model achieved the most accurate results in general. This finding is in line with the previous study *(Li et al., 2021)* that showed RF and U-Net methods had the best performance for a mineral segmentation task on SEM images of a shale sample compared to other machine learning models.

In addition, the results for the U-Net deep learning method using different metric and loss functions (S1, S2, and S3) are promising that are in good agreement with previous works using focal loss and dice losses *(Yeung et al., 2021; Wang et al., 2020)*. The higher performance of the deep learning method compared to machine learning methods is that the deep learning pixel segmentation better identifies patterns in complex image datasets. It eventually uses these patterns to perform classification. Another reason is that it has a dynamic (online) process of learning and training for adjusting its feature weights and biases. In addition, com-pared to Feed Forward Neural network, U-Net utilizes deep layers which helps it to project data to a higher dimension (more features). As a result, this image segmentation technique is a more powerful tool for partitioning challenging image datasets, which may include a variety of artifacts and noises, as well as grayscale similarities which previously are difficult to segment by thresholding or any other traditional approaches.

In general, the results obtained from the comparison of different methods (Figures 2.5 and 2.6) show the U-Net model with the combination of focal and dice loss (S3) and the RF with 14 features (14F) outperform other methods in terms of accuracy (0.88 for RF and 0.91 for U-Net on the Mancos dataset, and 0.94 for RF and 0.93 for U-Net on Marcellus dataset), IOU (0.67 for RF and 0.75 for U-Net on the Mancos dataset, and 0.71 for RF and 0.71 for U-Net on Marcellus dataset), and F1-score (0.78 for RF and 0.84 for U-Net on the Mancos dataset, and 0.81 for RF and 0.80 for U-Net on Marcellus dataset) on both test samples. This is in good agreement with previous

studies *(*Chen *et al., 2020; Li et al., 2021)*. In the study conducted by *(Chen et al., 2020)*, the U-Net method that was applied to SEM images of Duvernay Shale samples showed an IOU of 0.9 indicating the power of the U-Net deep learning method for phase segmentation of core shale images over other machine learning methods.

Figures 2.7 and 8 show IOU scores for the perdition of different phases for the Mancos dataset and Marcellus datasets. In Figure 2.7, '0' is organic matter, '1' is the Kaolinite + Dolomite + Calcite group, '2' is background, '3' is Quartz + Illite/Smectite + Albite group, '4' is pyrite. In Figure 2.8, '0' is organic matter, '1' is the Muscovite + Microcline + Albite +Dolomite + Quartz group, '2' is background, '3' is Calcite + clay group, 4 is pyrite. The results show that major phases such as grains (mostly quartz), matrix (which was mostly calcite and clays), pyrite, and background were correctly detected in almost all cases. However, organic matter (class '1′) was not predicted accurately due to misclassification with the background. Both background and organic matter classes share similar comprising features including black grayscale value with no specific pattern or texture.

As shown in Figures 2.7 and 2.8, considering extracted features (e.g., 14F and VGG16F) in addition to color attenuation improved samples' IOU score in almost all classes. The increase in IOU was as low as 4% or as high as 45%. This indicates the power of feature-based machine learning which is particularly valuable for a small dataset where ap-plying deep learning methods and trainable filtering techniques is difficult or even impossible.

Compared to the RF model with the original image (OI) and 14 features (14F), the predicted images by the U-Net model exhibited a better performance (less scatteredness, artifacts, and misclassification) in terms of prediction of different classes, especially for isolated small particles. It is because the U-Net model takes the spatial information of the input data along with attenuation

(grayscale) information. The results are in good agreement with *(Li et al., 2021)* and *(*Chen *et al., 2020)*.

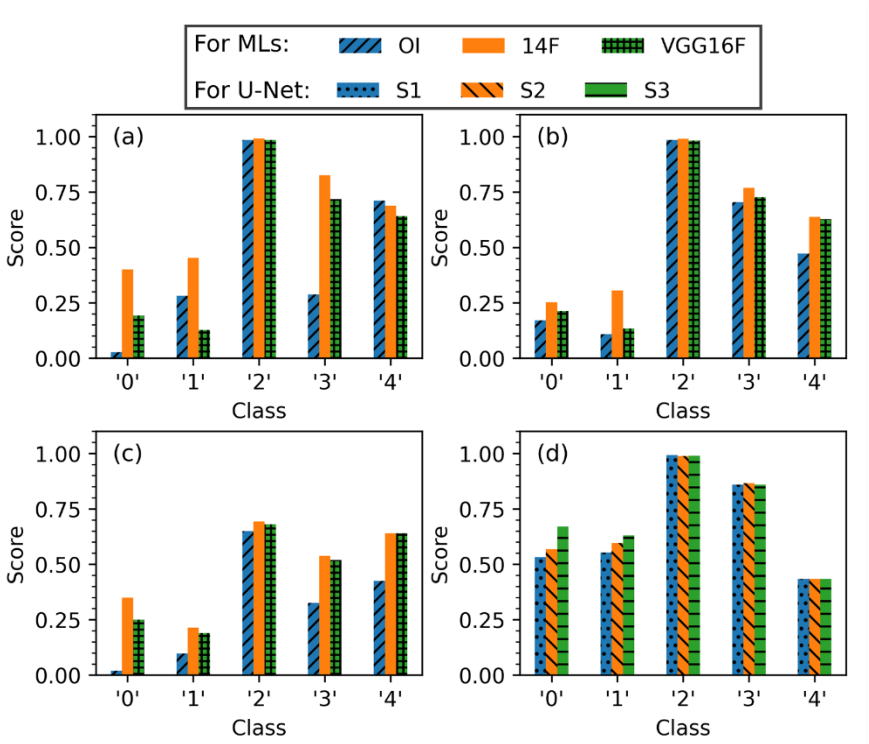

Figure 2.7. IOU score for the perdition of different phases for the Mancos dataset (‘0′ is organic matter, ‘1’ is the ‘Kaolinite + Dolomite + Calcite’ group, ‘2’ is background, ‘3’ is ‘Quartz + Il-lite/Smectite + Albite’ group, ‘4’ is pyrite). (a) IOU score for the RF model, (b) IOU score for the FNN model, (c) IOU score for the K-means model, and (d) IOU score for the U-Net model.

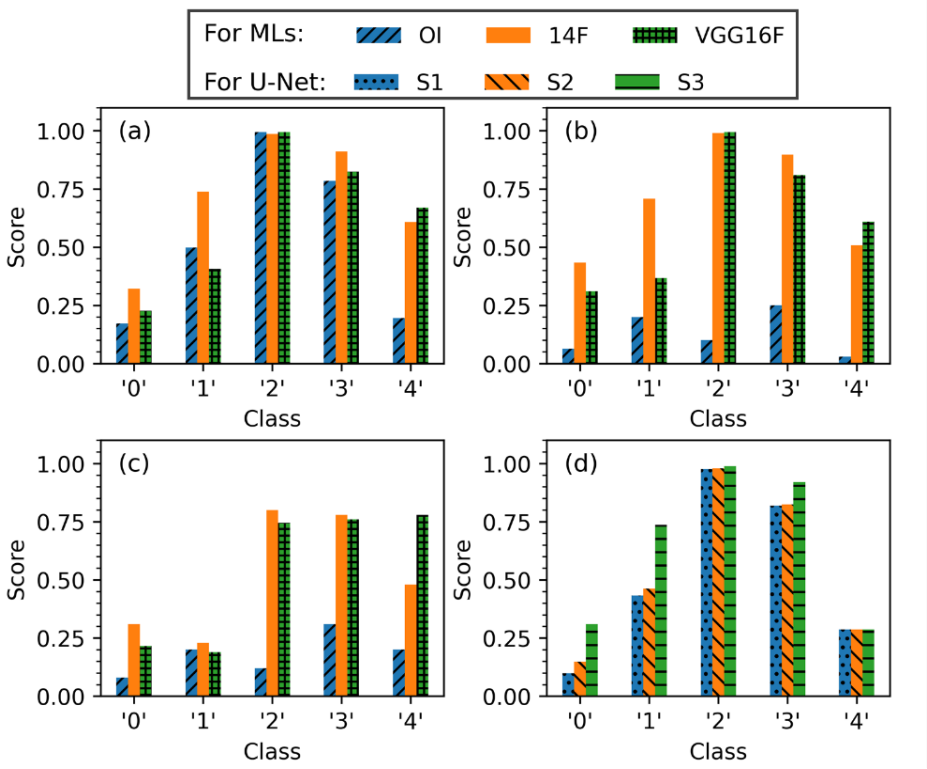

Figure 2.8. IOU score for the perdition of different phases for Marcellus dataset (‘0’ is organic matter, ‘1’ is the ‘Muscovite + Microcline + Albite +Dolomite + Quartz’ group, ‘2’ is background, ‘3’ is ‘Calcite + clay’ group, ‘4’ is pyrite). (a) IOU score for the RF model, (b) IOU score for the FNN model, (c) IOU score for the K-means model, and (d) IOU score for the U-Net model.

2.4.2. Applying Trained Machine Learning and U-Net Models on an Unseen Sample

In this section, an example of applying machine learning and U-Net deep learning models for phase segmentation of unseen X-ray CT images is discussed and visualization is provided. A total of 963,186 pixels were fed into the trained models to visually compare the results. The ground truth (labeled data) and predicted images are shown in Figure 2.9 (Marcellus) and Figure 2.10 (Mancos), respectively. In both figures, the label data is shown along with the output from the models. Only the top-performing methods are selected and shown for brevity, for example, for RF and FNN, the results with original images (OI) as input as well as VGG16 filters (VGG16F) as input are shown while for U-Net the scenario 3 (S3) is presented. As shown in these figures, the difference between simple and feature-based semantic segmentation is well demonstrated in visualization of pixel-

wise semantic segmentation obtained from the RF and FNN models (Figures 2.9 and 2.10). It is clear that adding extra features to machine learning models improved the prediction results.

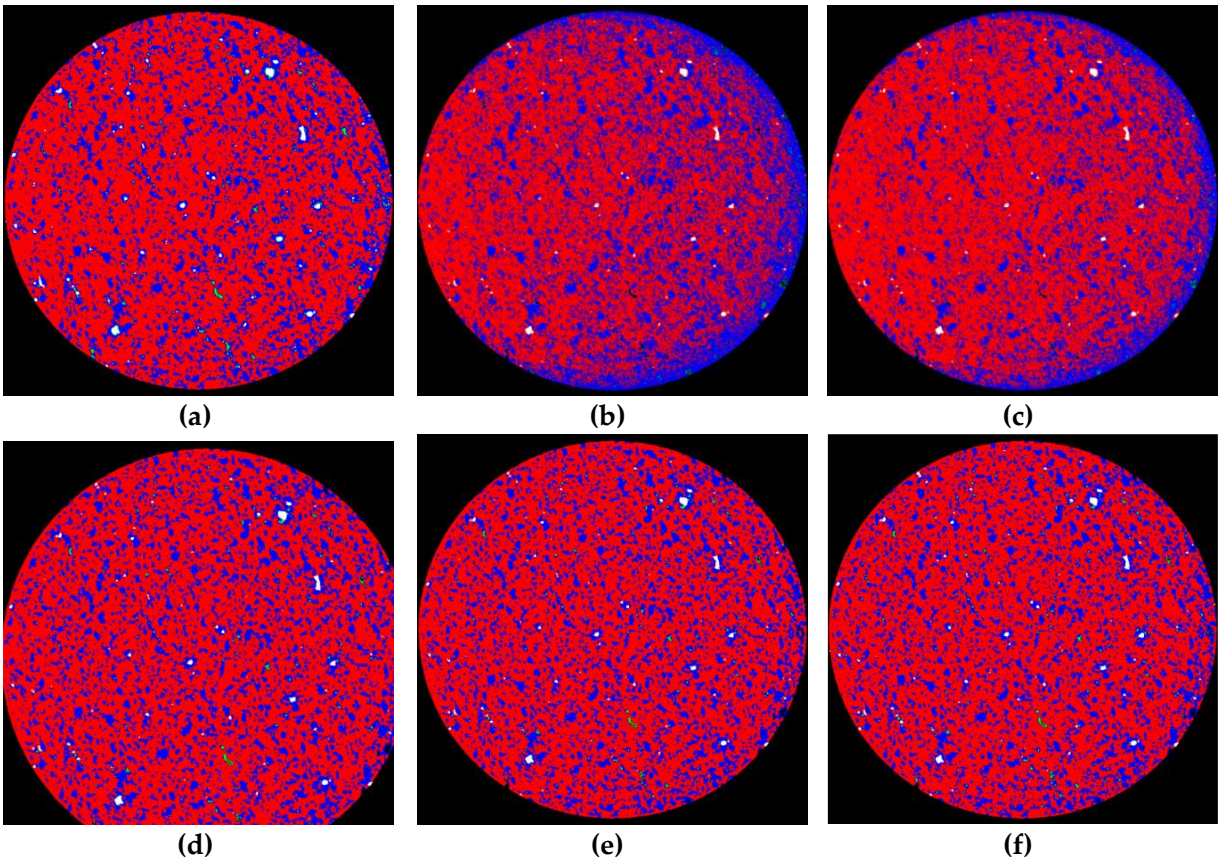

Figure 2.9. Output phase segmented images using ML methods with filtering techniques and deep learning method for Marcellus sample. (a) label image, (b) FNN model using original image as input (OI), (c) RF model using original image as input (OI), (d) U-Net considering focal and dice loss as the loss function (S3), (e) FNN model using 14 extracted features as input (14F), (f) RF model using 14 extracted features as input (14F)

In addition, results show that the machine learning with different filtering techniques removed artifacts (such as the blue ring in Figure 2.9) and improved prediction near the borders in both samples. As such, the special variation in color attenuation of a given phase which prevents a correct phase segmentation, especially on the edges of X-ray CT images, is not a prohibitive issue and can be addressed. The result of U-Net with Focal and dice loss showed the best

segmentation among all methods which improved the reliability of prediction of minority classes and removed noise from the predicted segmented images. This is in good agreement with previous studies *(Yeung et al., 2021; Wang et al., 2020)*. In general, a comparison of predicted results in both samples shows that filtering techniques and the deep learning method improve the predation of borders of each phase (edges).

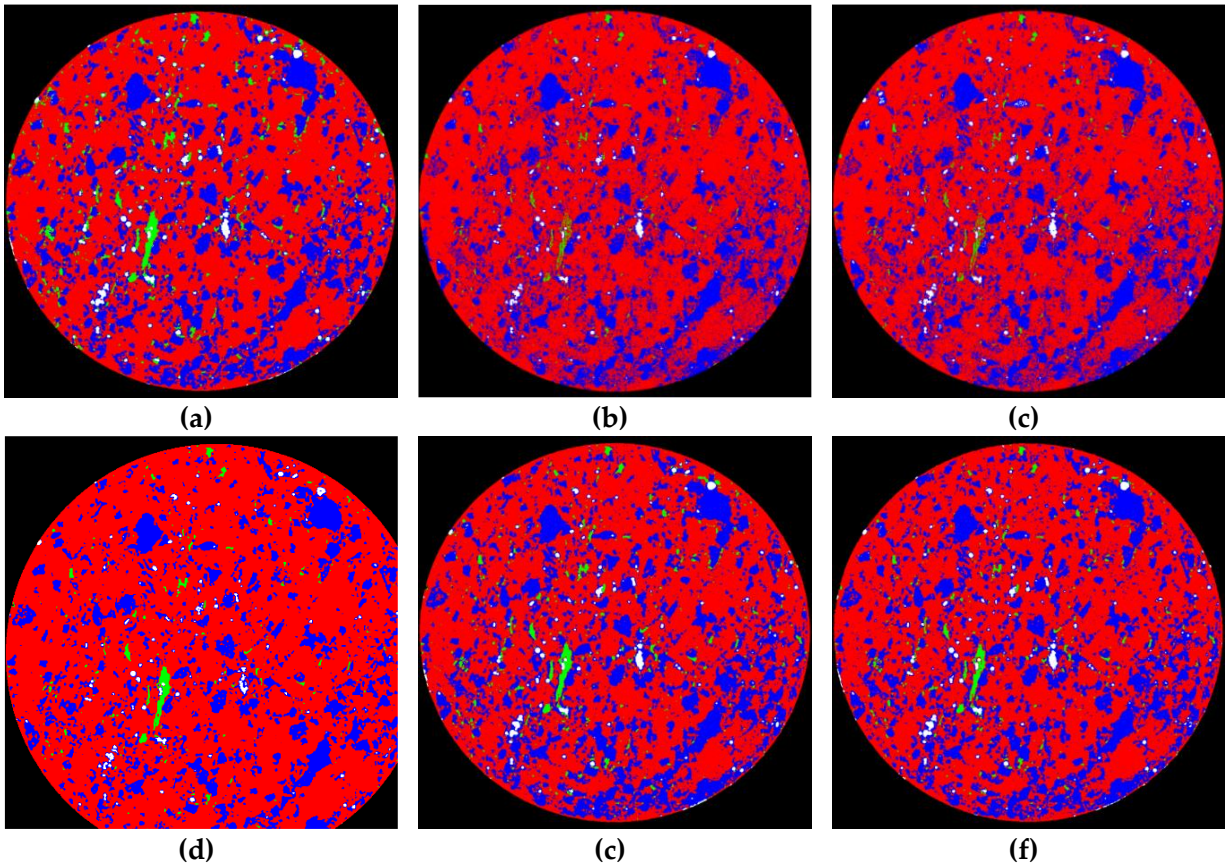

Figure 2.10. Output phase segmented images using machine learning methods with filtering techniques and deep learning methods for the Mancos sample. (a) label image, (b) FNN model using original image as input (OI), (c) RF model using original image as input (OI), (d) U-Net considering focal and dice loss as the loss function (S3), (e) FNN model using 14 extracted features as input (14F), (f) RF model using 14 extracted features as input (14F).

2.4.3. Core Segmentation and Analysis

The X-ray CT image dataset of the Mancos and Marcellus core samples were processed and segmented using the best-trained model (U-Net, S3) with python programming language. Visualization of segmented pyrite, matrix, grains, organic matter, and background within the cores are shown in Figure 2.11 for both samples. As shown, the most prevalent component of the Marcellus sample is calcite (red color) which is confirmed by XRD data. In Mancos, the quartz-dominated matrix is the most dominant phase that also agreed with the XRD data.

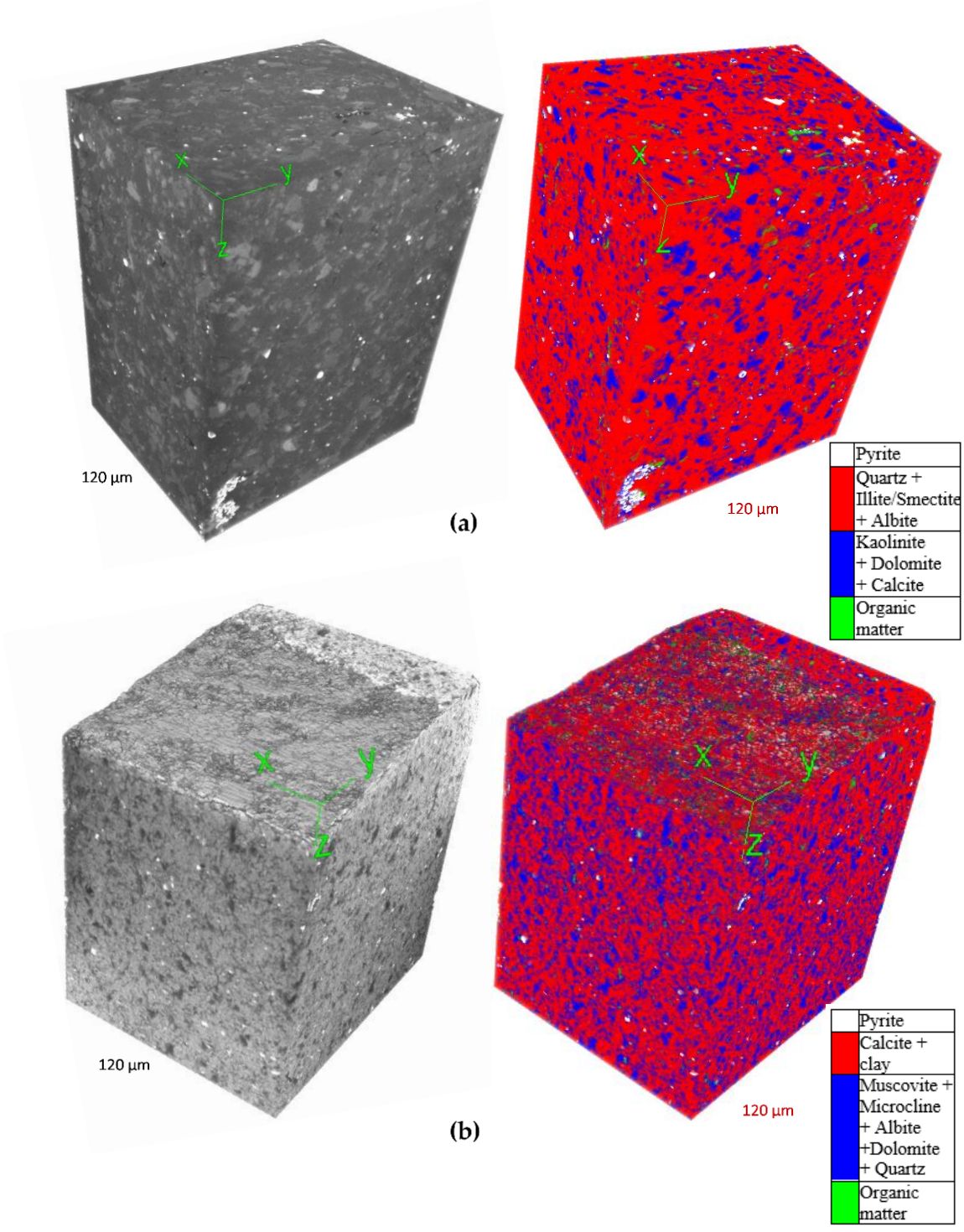

Figure 2.11. The 3D view of segmented core samples;(a) Mancos and (b) Marcellus samples.

Segmented images may be used to extract useful data such as grain size distributions or mineral volume fractions. Here, the grain size distribution analysis of granular minerals was performed to determine the relative size of the most abundant granular mineral phase (blue color in both samples) presented within both samples (Figure 2.12). The ImageJ plugin was used to calculate the area, size, and spatial information of the segmented blue phase within predicted images. Then, each grain diameter was calculated to plot the diameter distribution.

Figure 2.12 depicts the grain size distribution of granular minerals (blue color in both samples) within both Mancos and Marcellus images and the predicted ones obtained from the RF and U-Net (S3) models. The analysis of grain distribution confirms the previous data and suggests although the predicted grain distribution of both methods is similar to the true grain distribution, the U-Net is more similar to ground truth data. It is particularly more evident in the Mancos sample.

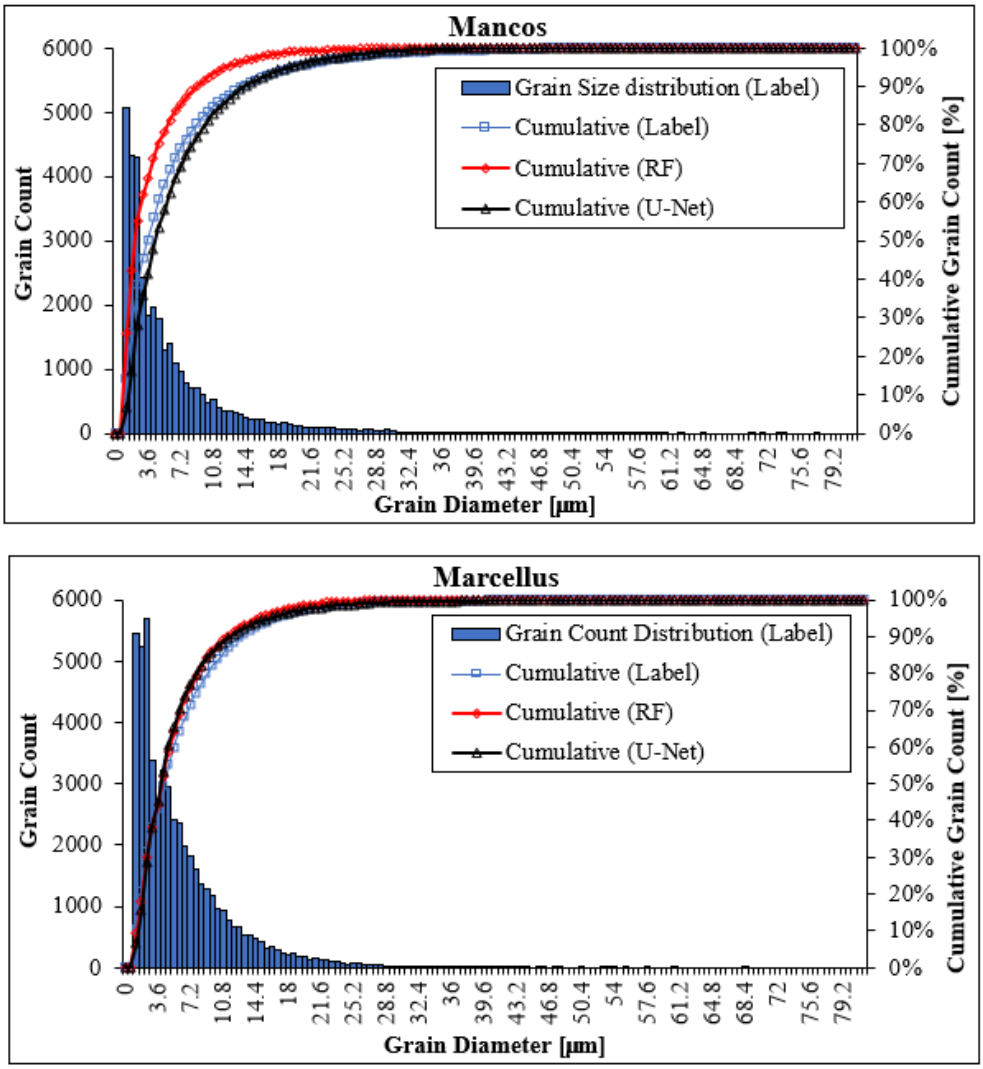

Figure 2.12. Grain size distribution of granular minerals within samples imaged with X-ray CT; (a) the distribution for Mancos sample, (b) the distribution for Marcellus sample.

2.4.4. Feature Importance

The RF model, which had the best performance among all machine learning methods, was used to determine the most important variables for pixel-wise phase segmentation based on the "mean decrease in Gini Impurity". This metric was chosen due to its robustness in ranking the variable importance.

The rank of each variable at each dataset was obtained using Gini Impurity and the final variable importance ranking was calculated by averaging the results over both samples. Figure 2.13 shows the relative rank of variable importance based on a decrease in Gini Impurity for the classification task. The higher the number, the more important the filter. Higher numbers show a higher contribution to successful classification. As shown in the Figure, the Median filter had the highest importance followed by the original image and difference of the Gaussian filter. The feature importance results for VGG16F extracted features showed “filter 32” has the highest contribution to the classification tasks. VGG16 has 64 filters which are named from 1 to 64. In this figure, the most contributing filters are ranked and named from F-4 to F-32

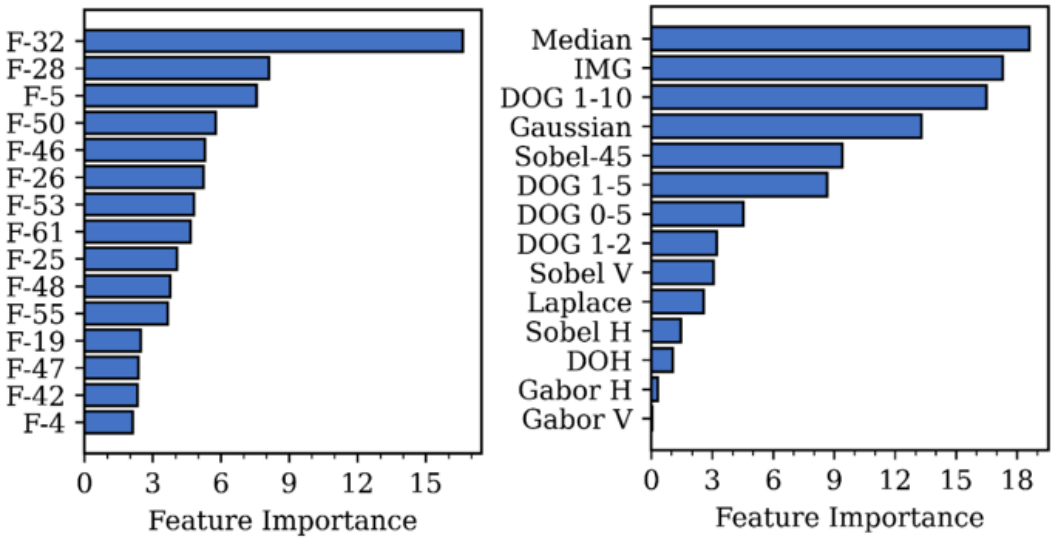

Figure 2.13. The rank of the extracted features is based on their contribution to improving seg-mentation (vertical variables are filter names, for example, F-32 is the 32nd filter of the second convolutional layer of VGG16, and horizontal numbers are the average rank of filters called feature importance value). (a)the rank for the VGG16F extracted features; (b) the rank for the 14F extracted features.

2.5. **Conclusion**

This research explores the feasibility of using machine learning approaches with feature extraction techniques for pixel-level phase segmentation of shales in 3D X-ray CT images. Once segmented, the categorized data could be used to retrieve useful information such as grain size distributions. Based on the results for two different datasets, RF had the best accuracy among all applied machine learning methods due to its capability to handle imbalanced datasets and data scarcity. The feature-based RF model (14F-RF and VGG16F-RF) improved the segmentation results significantly for both samples since filtering techniques helped to find additional features to reliably segment different phases. Feature importance analysis showed the Median and Gaussian filters had the highest contribution in phase segmentation due to removing unwanted noise and providing more integrated phases.

The results from U-Net showed even higher performance compared to RF. Considering all three methods of evaluations (i.e., F1-score, IOU, and accuracy), the U-Net method has a better performance in predicting each class compared to all other methods which provide a more reliable phase segmentation in different sample types.

It was also shown that the loss function plays an essential role in determining the model performance in both Marcellus and Mancos samples. The results showed that, for the complex objectives of mineral phase segmentation, it is not efficient to train the model only based on a universal loss function such as categorical cross-entropy which just monitors the overall loss since the majority class can directly affect it. In fact, for highly imbalanced segmentation, focal and dice losses, which are focus-based loss functions, work better as it minimizes the error based on each class as well as the overall error. As a result, a minority class is less likely to be overwhelmed by a majority class.

Overall, it was shown that the U-Net deep learning model can outperform machine learning models for mineral phase segmentation and is the recommended method when a large dataset is available. This study will help geologists to obtain the different distinguishable phases in 3D X-ray CT images to provide practical techniques for reliable phase segmentation. The future work would be further distinguishing discrete mineral phases by training ML/DL methods using SEM images of a surface of a given sample as ground truth for the X-ray CT mineral segmentation task. The trained model then can be utilized to segment the complete stack of X-ray CT images into individual mineral phases.

Supplementary Materials: The following are available online at https://github.com/Parisa-Asadi/Integrating-machine-deep-learning-and-filtering-techniques-for-reliable-mineral-phase-segmentation/blob/main/README.md, Video: S1: A 3D View of Mancos Shale (View 1); S2: A 3D view of Mancos Shale (View 2); S3: A 3D view of Phase Segmented Mancos Shale; S4: A 3D view of Marcellus Shale (View 1); S5: A 3D view of Marcellus Shale (View 2); S6: A 3D view of Phase Segmented Marcellus Shale.

Author Contributions:

Conceptualization, P. Asadi and L.E. Beckingham, methodology, software, validation, formal analysis, data curation, writing – original draft preparation, and visualization P. Asadi, resources, writing – review and editing, supervision, project administration, and funding acquisition L.E. Beckingham. All authors have read and agreed to the published version of the manuscript.

Funding:

This research has been supported by American Chemical Society Petroleum Research Fund: 58471 DNI 9 and National Science Foundation: CMMI MRI 1919818.

Institutional Review Board Statement:

Informed Consent Statement:

Not applicable.

Data Availability Statement:

The visualized data that support the findings of this study can be found here: [https://github.com/Parisa-Asadi/Integrating-machine-deep-learning-and-filtering-techniques-for-reliable-mineral-phase-segmentation/blob/main/README.md]. The raw data is available from the corresponding author, Lauren E. Beckingham, upon request.

Acknowledgments: Acknowledgments are made to the Donors of the American Chemical Society Petroleum Research Fund for support (or partial support) of this research. Purchase of the X-ray Computed Nano-tomography instrument used to obtain results included in this publication was supported by the National Science Foundation under the award CMMI MRI 1919818.

Conflicts of Interest: The authors declare no conflict of interest.

2.6. References

- Abadi, M.; Barham, P.; Chen, J.; Chen, Z.; Davis, A.; Dean, J.; Devin, M.; Ghemawat, S.; Irving, G.; Isard, M.; et al. Tensorflow: A system for large-scale machine learning. In

Proceedings of the 12th USENIX Symposium on Operating Systems Design and Implementation, Savannah, GA, USA, 2–4 November 2016; pp. 265–283.

- Anderson, T.I.; Vega, B.; Kovscek, A.R. Multimodal imaging and machine learning to enhance microscope images of shale. Comput. Geosci. 2020, 145, 104593.
- Anjikar, I.S.; Wales, S.; Beckingham, L.E. Fused Filament Fabrication 3-D Printing of Reactive Porous Media. Geophys. Res. Lett. 2020, 47, e2020GL087665.
- Bensinger, J.; Beckingham, L.E. CO_2 storage in the Paluxy formation at the Kemper County CO_2 storage complex: Pore network properties and simulated reactive permeability evolution. Int. J. Greenh. Gas. Control 2020, 93, 102887.Bradski, G.; Kaehler, A. Learning OpenCV: Computer Vision with the OpenCV Library. O'Reilly Media, Inc.: Newton, MA, USA, 2008.
- Breiman, L. Random forests. Mach. Learn. 2001, 45, 5–32.
- Brunhoeber, O.M.; Anovitz, L.M.; Beckingham, L.E. Role of mineralogy in controlling fracture formation. ACS Earth Space Chem. Under review.
- Chauhan, S.; Rühaak, W.; Anbergen, H.; Kabdenov, A.; Freise, M.; Wille, T.; Sass, I. Phase segmentation of X-ray computer tomography rock images using machine learning techniques: An accuracy and performance study. Solid Earth 2016, 7, 1125–1139.
- Chen, Z.; Liu, X.; Yang, J.; Little, E.; Zhou, Y. Deep learning-based method for SEM image segmentation in mineral charac-terization, an example from Duvernay Shale samples in Western Canada Sedimentary Basin. Comput. Geosci. 2020, 138, 104450.
- Cnudde, V.; Boone, M.N. High-resolution X-ray computed tomography in geosciences: A review of the current technology and applications. Earth-Sci. Rev. 2013, 123, 1–17.

- Da Wang, Y.; Shabaninejad, M.; Armstrong, R.T.; Mostaghimi, P. Physical accuracy of deep neural networks for 2d and 3d multi-mineral segmentation of rock micro-CT images. arXiv 2020, arXiv:2002.05322.
- Dice, L.R. Measures of the amount of ecologic association between species. Ecology 1945, 26, 297–302.
- Dhanachandra, N.; Manglem, K.; Chanu, Y.J. Image segmentation using K-means clustering algorithm and subtractive clus-tering algorithm. Procedia Comput. Sci. 2015, 54, 764–771.
- Feurer, M.; Springenberg, J.; Hutter, F. Initializing bayesian hyperparameter optimization via meta-learning. In Proceedings of the AAAI Conference on Artificial Intelligence, Austin, TX, USA, 25–30 January 2015; Volume 29, No. 1.
- Goral, J.; Andrew, M.; Olson, T.; Deo, M. Correlative core-to pore-scale imaging of shales. Mar. Pet. Geol. 2020, 111, 886–904.
- Gihm, Y.S.; Hwang, I.G.; Kim, H.T.; Lee, H.S.; Lee, D.S. Geological Characteristics and Development Strategy of the Marcellus Shale. J. Korean Soc. Mineral. Energy Resour. Eng. 2011, 48, 371–382.
- Gupta, I.; Rai, C.; Sondergeld, C.; Devegowda, D. Rock Typing in Eagle Ford, Barnett, and Woodford Formations. SPE Res-ervoir Eval. Eng. 2018, 21, 654–670.
- Gupta, I.; Rai, C.; Sondergeld, C.; Devegowda, D. Rock typing in the upper Devonian-lower Mississippian
- Guntoro, P.I.; Tiu, G.; Ghorbani, Y.; Lund, C.; Rosenkranz, J. Application of machine learning techniques in mineral phase segmentation for X-ray microcomputed tomography (µCT) data. Miner. Eng. 2019, 142, 105882.

- Guntoro, P.I.; Ghorbani, Y.; Koch, P.H.; Rosenkranz, J. X-ray microcomputed tomography (μCT) for mineral characterization: A review of data analysis methods. Minerals 2019, 9, 183.
- Hart, E.; Sim, K.; Kamimura, K.; Meredieu, C.; Guyon, D.; Gardiner, B. Use of machine learning techniques to model wind damage to forests. Agric. For. Meteorol. 2019, 265, 16–29.
- Hawkins, S.J.; Charpentier, R.R.; Schenk, C.J.; Leathers-Miller, H.M.; Klett, T.R.; Brownfield, M.E.; Finn, T.M.; Gaswirth, S.B.; Marra, K.R.; Le, P.A.; et al. Assessment of Continuous (Unconventional) Oil and Gas Resources in the Late Cretaceous Mancos Shale of the Piceance Basin, Uinta-Piceance Province, Colorado and Utah; United States Geological Survey: Reston, USA, 2016; pp. 2016–3030.
- Heaton, J. Chapter 12: Pruning and Model Selection. In AIFH, Volume 3: Deep Learning and Neural Networks. Heaton Research, Inc.: St. Louis, MO, USA, 2015; pp. 195–204.
- Iloejesi, C.O.; Beckingham, L.E. Assessment of geochemical limitations to utilizing CO_2 as a cushion gas in compressed energy storage systems. Environ. Eng. Sci. 2021, 38, 115–126.
- Karimpouli, S.; Tahmasebi, P. Segmentation of digital rock images using deep convolutional autoencoder networks. Comput. Geosci. 2019, 126, 142–150.
- Landrot, G.; Ajo-Franklin, J.B.; Yang, L.; Cabrini, S.; Steefel, C.I. Measurement of accessible reactive surface area in a sandstone, with application to CO_2 mineralization. Chem. Geol. 2012, 318, 113–125.
- Li, C.; Wang, D.; Kong, L. Application of Machine Learning Techniques in Mineral Classification for Scanning Electron Mi-croscopy-Energy Dispersive X-Ray Spectroscopy (SEM-EDS) Images. J. Pet. Sci. Eng. 2021, 200, 108178.

- Pedregosa, F.; Varoquaux, G.; Gramfort, A.; Michel, V.; Thirion, B.; Grisel, O.; Duchesnay, E. Scikit-learn: Machine learning in Python. J. Mach. Learn. Res. 2011, 12, 2825–2830.
- Qin, F.; Beckingham, L.E. Impact of image resolution on quantification of mineral abundances and accessible surface areas. Chem. Geol. 2019, 523, 31–41.
- Ronneberger, O.; Fischer, P.; Brox, T. U-net: Convolutional networks for biomedical image segmentation. In Proceedings of the International Conference on Medical Image Computing and Computer-Assisted Intervention Springer, Munich, Germany, 5–9 October 2015; pp. 234–241.
- Saikia, P.; Baruah, R.D.; Singh, S.K.; Chaudhuri, P.K. Artificial Neural Networks in the domain of reservoir characterization: A review from shallow to deep models. Comput. Geosci. 2020, 135, 104357.
- Semnani, S.J.; Borja, R.I. Quantifying the heterogeneity of shale through statistical combination of imaging across scales. Acta Geotech. 2017, 12, 1193–1205.
- Sorensen, T.A. A method of establishing groups of equal amplitude in plant sociology based on similarity of species content and its application to analyses of the vegetation on Danish commons. Biol. Skar. 1948, 5, 1–34.
- Spokas, K.; Fang, Y.; Fitts, J.P.; Peters, C.A.; Elsworth, D. Collapse of reacted fracture surface decreases permeability and frictional strength. J. Geophys. Res. Solid Earth 2019, 124, 12799–12811.
- Suthaharan, S. Machine learning models and algorithms for big data classification. Integr. Ser. Inf. Syst. 2016, 36, 1–12.
- Ulker, E.; Sorgun, M. Comparison of computational intelligence models for cuttings transport in horizontal and deviated wells. J. Pet. Sci. Eng. 2016, 146, 832–837.

- Van der Walt, S.; Schönberger, J.L.; Nunez-Iglesias, J.; Boulogne, F.; Warner, J.D.; Yager, N.; Gouillart, E.; Yu, T. scikit-image: Image processing in Python. Peer J. 2014, 2, e453.
- Wildenschild, D.; Sheppard, A.P. X-ray imaging and analysis techniques for quantifying pore-scale structure and processes in subsurface porous medium systems. Adv. Water Resour. 2013, 51, 217–246.
- Wang, L.; Wang, C.; Sun, Z.; Chen, S. An Improved Dice Loss for Pneumothorax Segmentation by Mining the Information of Negative Areas. IEEE Access 2020, 8, 167939–167949.
- Yang, H.; Zhao, Y.; Zhang, X.; Liu, G.; Du, X.; Shang, D.; Yu, Y.; Chen, J.; Wang, H.; Tu, H. Supercritical CO_2 fracturing with different drilling depths in shale. Energy Sources Part A Recovery Util. Environ. Eff. 2021, 1–20, doi:10.1080/15567036.2019.1673850.
- Yakaboylu, G.A.; Gupta, N.; Sabolsky, E.M.; Mishra, B. Mineralogical characterization and strain analysis of the Marcellus shales. Int. J. Rock Mech. Min. Sci. 2020, 130, 104345.
- Yeung, M.; Sala, E.; Schönlieb, C.B.; Rundo, L. Unified Focal loss: Generalising Dice and cross entropy-based losses to handle class imbalanced medical image segmentation. arXiv 2021, arXiv:2102.04525.
- Yoon, H.; Ingraham, M.D.; Grigg, J.; Rosandick, B.; Mozley, P.; Rinehart, A.; Mook, W.M.; Dewers, T. Impact of Depositional and Diagenetic Heterogeneity on Multiscale Mechanical Behavior of Mancos Shale. Am. Assoc. Pet. Geol. Mex. Utah USA 2019, doi: 10.1306/13672214M1213824.

CHAPTER 3

INTELLIGENT FRAMEWORK FOR MINERAL SEGMENTATION AND FLUID-ACCESSIBLE SURFACE AREA ANALYSIS IN SCANNING ELECTRON MICROSCOPY

Parisa Asadi and Lauren E. Beckingham

Department of Civil and Environmental Engineering, Auburn University, Auburn, AL 36849

Published in Applied Geochemistry, 2022, 143, 105387.

https://doi.org/10.1016/j.apgeochem.2022.105387

ABSTRACT

Imaging is powerful means of sample characterization where mineral abundances and surface areas can be quantified from mineral maps. Images are typically manually processed by domain experts, which is time-consuming, labor-intensive, and subjective. Emerging techniques, such as machine learning based image processing, can potentially address these limitations and accelerate image processing but the performance of these models for accurate sample characterization and surface area analysis has not been completely evaluated. This study evaluates the potential of Random Forest and U-Net machine learning methods for mineral characterization and surface area analysis of six sandstone samples. Various input variable sets including filter extracted features, scanning electron microscopy (SEM) backscatter electron (BSE) images and SEM-energy dispersive x-ray spectroscopy (EDS) images were considered. The evaluation was conducted by providing an intelligent framework that not only evaluates the accuracy of prediction for each pixel but also investigates the accuracy of predicted neighboring pixels. In addition, a new methodology is proposed to distinguish the more susceptible places to dissolution on the surface of a given

mineral using a ranked mineral dissolution risk assessment map. The results showed both methods had an acceptable performance with the U-Net model outperforming Random Forest. Both methods showed an improved accuracy when filter-extracted features were added to the dataset as input variables. The models' performance predicting mineral abundances and accessibility agreed well with ground truth data for majority classes (e.g., quartz) compared to minority classes. Finally, the proposed methodology was shown to reliably identify the locations susceptible to dissolution indicated via proposed risk assessment maps. The intelligent segmentation and surface area analysis framework is a promising tool for accelerating the processing of SEM data and reactivity assessment of samples.

3.1. **Introduction**

Micro-porosity imaging is a valuable technique for characterizing mineral/pore spatial distributions in the fields of geosciences and environmental engineering. The extracted parameters such as porosity, mineral abundance, texture, fracture distribution, and accessible mineral surface areas (*Qin and Beckingham 2019; Landrot et al. 2012; Peters 2009; Ma et al., 2021; Luhmann et all., 2017*) are the basis for digital rock analysis (*Asadi and Beckingham, 2021; Kim et al., 2021; Brunhoeber et al., 2021; Anovitz et al., 2022*) and other related computational simulation works. Reactive transport models utilize this information to simulate geochemical reactions that vary from a chemical weathering induced mineral dissolution (*Chen et al., 2020a; Mahdikhani et al., 2018; Deng et al., 2020*), to rather complex CO_2-brine-mineral interactions in carbon capture and storage (CCS) systems (*Beckingham et al., 2017; Qin and Beckingham, 2019*) and reactions in multi-mineral subsurface energy storage (*Koohi-Fayegh and Rosen, 2020; Iloejesi and Beckingham 2021a&b)* and enhanced oil recovery (*Esene et al., 2019; Seyyedi et al., 2018*) Systems.

Scanning electron microscopy backscattered electron microscopy (SEM-BSE) imaging is a powerful technique for mineral analysis and microstructure characterization (*Li et al., 2021; Peters, 2009*). SEM imaging incorporating energy-dispersive X-Ray spectroscopy (EDS) elemental maps enable classification of minerals and facilitates quantification of mineral phases, including those with abundance less than the X-ray diffraction (XRD) detection limit (*Landrot et* al. 2012). Although XRD is a great source for mineral identification, it cannot provide any spatial information. In addition, XRD has noted limitations for distinguishing the minority mineral phases based on the instrument used, often 1% (Landrot et al., 2012) to 5% (Beckingham et al., 2017 Salek Et al., 2022). These types of limitations do not restrict identification of minority phases via SEM-BSE and EDS imaging.

Extracted data from SEM-BSE and EDS imaging is useful for assessing sample properties or parameterizing reactive transport simulations to consider reactivity under a specified set of conditions (*Beckingham et al. 2017*). Quantification of mineral volume fractions and accessible surface areas are of particular interest where accessible surface area refers to mineral surfaces in contact with reactive fluids. Beckingham et al. (*2017*) found that simulations carried out using mineral accessible surface areas quantified from mineral/pore segmented images better reflected the reaction rates observed in core-flood experiments than simulations that used the specific surface areas measured via the Brunauer, Emmett and Teller method (BET). The BET theory is commonly used to evaluate the gas adsorption data and generate a specific surface area result expressed in units of area per mass of sample (m^2/g).

Despite advances in image processing and analysis, segmenting of SEM-BSE and EDS images is challenging. Images either need to be processed by software with a large element composition-to-mineral database such as Quantitative Evaluation of Minerals by Scanning

Electron Microscopy (QEMSCAN) (*Pirrie et al., 2004*) or to be conducted by experienced expert technicians (*Asadi and Beckingham, 2021; Brunhoeber et al., 2021; Kim et al., 2021*), both of which are expensive, time-consuming, labor-intensive, and subjective. Machine learning (ML) based methods have emerged as a relatively new and open-source approach for mineral classification.

Machine learning for geoscience and environmental engineering applications has included mineral characterization (*Karimpouli and Tahmasebi, 2019; Li et al., 2021; Chen et al., 2020b*), spatial distribution mapping (*Kim et al., 2021*), rock typing and permeability prediction (*Mohammadian et al., 2022, Yoon and Melander, 2021*). Pore-scale imaging has advanced crucially through the integration of machine learning with imaging techniques (*Asadi and Beckingham, 2021; Kim et al., 2021).* While prior work has considered use of machine learning for mineral segmentation in SEM images (*Li et al., 2021*), the performance of machine learning models for mineral characterization of SEM images based on mineral abundance and accessible surface area analysis, which is the focus of this work, has not been considered.

Using mathematical models, machine learning excavates nonlinear underlying patterns in a dataset (*Chen et al., 2020b; Zhang et al., 2022, Asadi and Beckingham 2021; Suthaharan, 2016*). Models can simultaneously consider several extracted features in addition to the color or grayscale intensity for a more reliable mineral/pore segmentation. This ability is valuable for segmenting individual minerals with similar or overlapping grayscale intensity in SEM BSE images as well as addressing grayscale color variations from one sample to the other due to different device parameter setups such as brightness or contrast. In these cases, extracted features of minerals are key to successful mineral/pore segmentation (*Asadi and Beckingham 2021; Suthaharan, 2016*). Relying only on gray-scale intensity for training of machine learning models can lead to unstable

models with less generalization to other datasets due to intensity variation among different images and intensity overlaps of different minerals. Combining image datasets with image filtering techniques as inputs to machine learning models can potentially improve mineral quantification and surface area analysis from images. This is because filters can find underlying patterns in minerals and therefore improve the prediction results.

This study aims to provide an intelligent platform for auto-segmentation of mineral/pore phases in SEM images, using mineral volume fractions and accessible surface area to evaluate performance. Two widely used machine learning methods, Random Forest and U-Net are used to process images of sandstone samples and mineral volume fractions and accessible surface areas determined from machine learning-processed images and compared with data from manually processed images. A quantitative dissolution risk assessment analysis that identifies locations more susceptible to dissolution by taking the predicted results for neighboring pixels into account is proposed. The prepared framework will help geologists obtain the mineralogy, mineral/pore spatial distribution and the mineral reactivity risk assessment maps for sandstone samples reliably and quickly based on SEM images. This automated and open-source framework to estimate mineral abundance and accessibility is also desirable to reduce time and resource requirements to obtain sample characteristics and inform reactive transport simulation models.

3.2. **Data and Methodology**

3.2.1. Sandstone Samples

Processed mineral maps for six sandstone samples introduced in our previous work (*Salek et al. 2022*) were selected for machine learning model training and analysis. Data included processed maps of Bandera Brown, Bentheimer, and Kentucky sandstones (samples purchased from Kocurek

Industries), Lower Tuscaloosa and Paluxy sandstones (samples from Geological Survey of Alabama), and an additional Paluxy sandstone from Kemper County pilot CO_2 injection site (Qin and Beckingham, 2019). In addition, a new pooled dataset was created and considered by the models which was the combination of the images of the six sandstone samples (referred to as the pooled dataset). The XRD data (Table 3.1) and prior compositional analyses of the samples showed that they are mainly quartz (66% - 94%), with various amounts of feldspars, carbonate and clay minerals, and trace amount of other mineral species such as chlorite, with porosity ranging from 14% to 33% (*Kocurek Industries; Guan 2012; Soong et al. 2016; Salek et al., 2022; Qin and Beckingham, 2019*).

Table 3.1. XRD composition analysis of the samples obtained from Kocurek Industries 1, Guan2 (2012) and Soong et al.3 (2016).

Sandstones	**XRD Source**	**Porosity**	**Quartz**	**Albite**	**Microcline**	**Calcite**	**Dolomite**	**Kaolinite**	**Illite**	**Chlorite**
Bandera Brown1	SPE-178999	22-23	66	13	2	3	0	3	11	2
Bentheimer1	SPE-174666	24	94.4	1.2	1.2	0.5	0			
Bandera Gray1	SPE-173736	20-21	59	12	0	0	15	3	10	1
Kentucky1	SPE-147395	14	66	17	3	0	0	trace	14	0
Paluxy2		20-25	69.3	24.5	1.2	0.8		2.3	0.2	
Lower Tuscaloosa3		30-33	92	0.5	1.6		1.5	3.7		

3.2.2. SEM BSE-EDS and Labeled Images

SEM BSE images of the samples used in this work and their corresponding EDS elemental maps were captured using a ZEISS EVO 50VP Scanning Electron Microscope at Auburn University and analyzed in our previous work (*Salek et al., 2022; Qin and Beckingham 2019*). SEM images were captured at resolutions ranging from 0.34 μm to 5.71 μm. Eight SEM-EDS elemental maps were used in this study including aluminum (Al), magnesium (Mg), sodium (Na), potassium (K), calcium (Ca), silicon, (Si), iron (Fe), titanium (Ti). Image acquisition was performed on single

image field of views for all samples except for the Paluxy sandstone from Kemper County pilot CO_2 injection site (Qin and Beckingham, 2019) that was generated from multiple image fields and was tiled to create a main image with the resolution of interest (0.34 µm). Mineral phases were identified based on relative grayscale intensity and elemental signatures (Peters, 2009), with knowledge of anticipated minerals from XRD data (Salek et al. 2022; Qin and Beckingham, 2019). The detailed information about the SEM-BSE and EDS image acquisition and device set up are provided by Qin and Beckingham (2019) and Salek et al. (2022), and detailed image processing methodology and its cross validation with XRD data can be found in Landrot et al. (2012) and Beckingham et al. (2017).

Here, to train the models and validate the machine learning models' performances, mineral maps were labeled with a specific label value assigned to each mineral as the ground truth value. Figure 3.1 shows an example of labeled image and its corresponding colors. As evident in the Figure, the samples were mainly comprised of quartz, carbonates, K-feldspar and albite. Table 3.2 shows the number of pixels of each mineral class for the six samples that 70%, 15% and 15% were used for training, validation, and test, respectively.

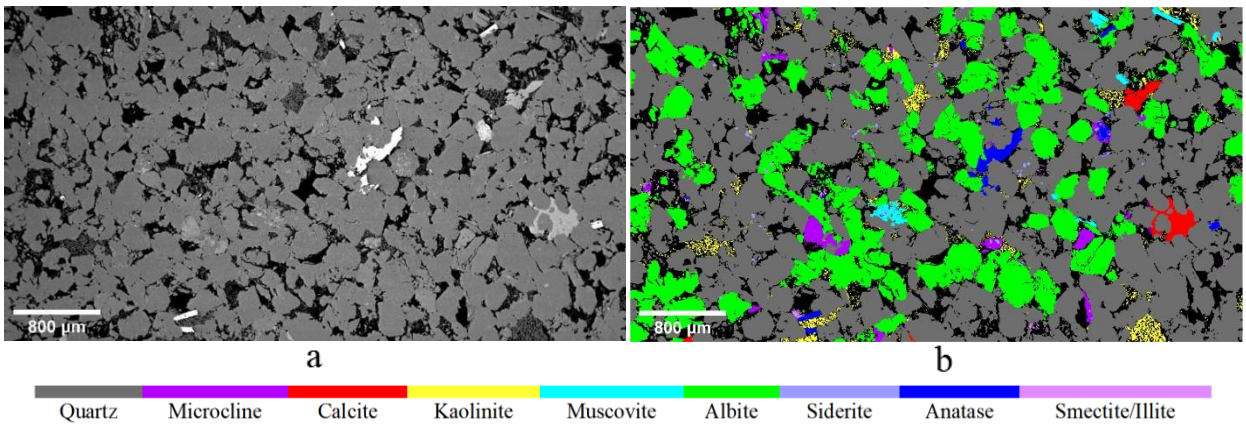

Figure 3.1. a) 2D SEM BSE image of a thin section from the Paluxy formation with image resolution of 1.9 µm, and image size of 17.14 mm^2 (reproduced from *Salek et al., 2022*), b.) Mineral phase segmented image.

Table 3.2. Labeled mineral/pore pixels for the samples.

Mineral	Label	Bandra Brown	Lower Tuscaloosa	Bentheimer	Kentucky	Bandera Gray	Paluxy Sample1	Paluxy Sample2
Pore	“0”	443623	144457	1616132	1145212	2552360	2673382	8183063
Quartz	“1”	1144567	267011	2845788	279728	727147	891332	19279109
Albite	“2”	159540	1396	74450	307767	411706	944590	
Kaolinite	“3”	67063	10623				87317	
Smectite/Illite	“4”	18267			215434	256845	9163	1791284
K-Feldspar	“5”	129752	4577	81431	53458	487745	46501	1058115
Chlorite	“6”	7581						
Magnetite	“7”	23169			47663			
Anatase	“8”	7333			3042	11581	31302	
Carbonate	“9”	105	4321	75		228996	30133	2615561
Muscovite	“10”		1510		46492	27582	23082	105808
Zircon	“11”				6672			
Ilmenite	“12”			10284	5362			
Siderite	“13”						11079	528404
Biotite	“14”					45734		

3.2.3. Feature Extraction

Minerals have different visible characteristics like texture and grain size which make them distinguishable from one another. Filtering techniques convolute the original images such that additional features may be reliably extracted for machine learning models to differentiate minerals with similar color intensity (*Asadi and Beckingham, 2021)*. In this study, well-known filters, including difference of Gaussian, Median, Non-local mean, Bilateral, vertical and horizontal Sobel filters, were applied to the sandstone BSE images using the OpenCV (*Bradski and Kaehler, 2008*) and Scikit-image (*Van der Walt et al., 2014*) libraries of Python. These filters provide feature maps representative of texture, grain size, edges and color variation. For instance, the Sobel and Bilateral

filters are used to extract edge features and textures, while difference of Gaussians is utilized for blobs and corners (*Asadi and Beckingham 2021*).

3.2.4. Establishing the Datasets

In this study, BSE images, elemental EDS maps, and extracted features were used as input variables for machine learning models. Labeled images were established as ground truth images for each sample and introduced to the models to be trained for mineral/pore segmentation. In addition to these individual sample datasets, a pooled dataset which was a combination of all samples was generated to further investigate feature-based machine learning mineral/pore segmentation on a more general and comprehensive database. For the Random Forest model, the input was the pixel-level grayscale values extracted from the BSE image, elemental maps (including Al, Mg, Na, K, Ca, Si, Fe, Ti), and filter extracted features (including difference of Gaussian disk 1 and 10, Bilateral, Median-blur, non-local Means, and Sobel filter in x and y directions). The label data was the mineral class that ranged from 0 to 14 for each pixel. The U-Net model was trained end-to-end where the input was images cut from the stacked BSE image, the elemental maps (i.e., Al, Mg, Na, K, Ca, Si, Fe, Ti), and the filter extracted features (i.e., difference of Gaussian disk 1 and 10, Bilateral, Median-blur, non-local Means, and Sobel filter in x and y directions), while the output was the corresponding mineral labels.

3.2.4.1. Dataset for Random Forest

The Random Forest training dataset for each sample had a shape of m×n, where m was the number of pixels, and n was the number of input variables obtained from the eight elemental EDS maps, BSE intensity image, and the six filter extracted feature maps (Table 3.2). The BSE and EDS intensity values at each pixel were extracted from the grayscale maps. Intensity values range from

0 (black) to 255 (white) and brighter pixels reflect higher elemental intensities in EDS maps and bigger average atomic numbers in BSE images. The brightness/intensity values of filter-extracted features demonstrates various patterns such as entropy or edges in the associated BSE images.

To create the database, each input variable was first normalized to transform data to the range of 0–1 by dividing each pixel value by the maximum value for that specific input variable. The input variable values at the same pixel location were then extracted as a vector containing 15 input values, including the inputs from BSE, EDS, and filter-extracted features. The mineral/pore class labels at the corresponding output pixels were the ground truth data with 15 mineral/pore classes (Table 3.2). The dataset for the samples was imbalanced as they were mainly comprised of quartz, feldspars, and calcite. To address this issue, different weights were assigned to each class that was proportional to the inverse percent size of each class within the dataset. Thus, a matrix with the size of the number of pixels in each dataset × 15 was used as input, where 15 denotes the number of input variables extracted at each data point.

The ground truth data was a vector with the size of the number of pixels in each dataset × 1 which contained the value of the mineral/pore class labels. The dataset of each sample was randomly split into training (70%), validation (15%) and test (15%) datasets to train and evaluate the Random Forest model.

3.2.4.2. Dataset for U-Net

3.2.5. Unlike the Random Forest model with pixel-level classification, where the input data was a matrix of shape m×n, the training process for the U-Net model was end-to-end and utilized neighboring pixels, which allows for segmented regions with less noise. To create the dataset, the stacked and normalized input images were cropped into smaller training samples (128×128 pixels). Then, using a data augmentation procedure that including flipping in both vertical and horizontal directions, zooming, shifting, and rotation, the amount of data was increased to have more data for improved prediction. For the pooled dataset, each input sample had a total of 15 channels (input variable set), while the output had 15 channels for each mineral/pore class. After data augmentation, there were a total of 8,505 samples (Table 3.2) for training and testing, which were further divided into training, validation, and testing, with the fractions of 70%, 15% and 15%. Pixel Wise Image Analysis and Segmentation Algorithms

3.2.5.1. Random Forest Machine Learning Model

Random Forest (*Breiman 2001*) is one of the powerful ensemble learning methods that combines *m* random decision trees (*mtree*) trained on different subsamples of data into a decision forest (*Asadi and Tian, 2021*) to solve regression/classification problems. The grown forest algorithm not only has higher precision over individual decision trees such as CART, but also is relatively unbiased to multivariate common linearity and imbalanced data (*Asadi and Beckingham 2021; Asadi and Tian 2021)* which makes it appealing for phase segmentation.

For training, the model randomly selects *N* subsamples from the training dataset using a Bootstrapping technique. Each sample set is used to construct a decision classification tree, each of which randomly selects *k* input variables and starts with a single node. Each node in the decision tree is a weak binary classifier which selects the various parameters (e.g., *k* input variables or a variable attribute) to maximize the classification index, whereas the final leaf node includes a discriminator to assign each pixel to a specific class. In Random Forest, each tree finds new splits and builds out it's nodes while minimizing the Gini impurity (equation 1) for each split based on

its information and patterns in a subsample of the training set, eventually stopping at leaf nodes when it reaches the maximum depth of tree or the minimum number of samples per node.

In general, each node in a forest seeks to minimize the impurity index. In this study, the Gini index that is one of the most common impurity functions was used. The function is given by,

$$\text{Gini (p)} = \sum_{k=1}^{k} p_k \,(1 - p_k) = 1 - \sum_{k=1}^{k} p_k^2 \qquad (1)$$

where p_k is probability that the sample belongs to class *k*. This represents the likelihood of misclassification of a random data point at a certain node if the data point were classified randomly. When the Gini coefficient is the smallest, the purity is the highest and the uncertainty is the smallest.

In this study, the Scikit-Learn library of Python was used to implement the Random Forest model (*Pedregosa et al., 2011*). At first, a model with 200 random trees (i.e., *ntree* = 200), each with unlimited depth and no pruning, was created. Randomly selected k input variables (estimated as the square root of the numbers of predictors, i.e., *ktry* ≈ 4) from all input variables were selected at each node to train the model. Next, the model's hyperparameters were fine-tuned. For *ktry* and *ntree* tuning, the random search was incorporated by grid searching the ntree in the range of 30 to 700 and *ktry* in the range of 2 to 8, resulting in the final forest of *ntree* = 50 and *ktry* = 4. The depth of tree changed from 15 to 4×15 and the best one was 32. The minimum sample per split was selected to be five based on random number search in the range of three to ten.

3.2.5.2. Modified U-Net Deep Learning Model

The U-Net method (*Ronneberger et al., 2015*), a fully connected Convolutional Neural Network (CNN) method, was originally proposed to efficiently capture nuances required in the analysis of medical images. Ever since, it has become a standard tool for various classification problems and

shown great performance by using less images and outputting more precise segmentation maps (*Asadi and Beckingham, 2021; Kim et al., 2021*). The architecture is based on a symmetric encoder–decoder approach which resembles a U-shaped structure. The encoder consists of contraction blocks to capture context via feature extraction. Each block takes a 128 by 128 input image to apply two convolutional kernels of 3 by 3, followed by a rectified linear transformation and a max-pooling operation with a stride of 2 by 2. The max-pooling process reduces spatial information while convolutional kernels increase feature channels in the encoder path allowing the network to learn complex structures effectively due to propagating context information to higher dimensions (*Asadi and Beckingham, 2021*). The decoder is responsible for precisely retrieving spatial information along the up sampling, where the output of each convolutional level is combined with high resolution features from the contraction part through skip connection ports. The expansion blocks in the decoder pass the input to two convolutional layers followed by a 2 by 2 up-sampling layer. In the decoder, while the image size gradually increases, the feature depth gradually decreases. At the end of the network, the feature images were passed through a 1 by 1 convolutional layer with a SoftMax activation function to perform the multi-layer semantic segmentation and provide the probability of each pixel, and map *M* features which are desired minerals/pore classes. The class associated with the highest estimated probability would then be the one assigned to that pixel.

This classification scheme was implemented in Python using the TensorFlow and Keras packages. Here, stacked BSE, EDS and filter extracted features from the original BSE images as well as their corresponding segmented maps were used for training. Several loss functions including focal (equation 2) and categorical cross-entropy were utilized and applied to adjusted weights and biases for finding the best performing one. The focal loss function, which is designed

to counteract class imbalance, had the best performance and is used in this study. In the focal loss function, each class is down-weighted such that their contribution to the total loss is small even if their number is large. The function is given by,

$$\text{Focal Loss}(p_t) = -\alpha_t(1-p_t)^{\gamma}\, log(p_t) \quad (2)$$

where p_t is the probability of a given class, α is a regulator parameter range from [0, 1], and γ controls the penalizing power of the model to the error and is an integer number greater than zero (γ>0). When γ = 1, the focal loss function works like the cross-entropy loss function. In this study, γ = 2 and α = 1 were set due to better performance. Adaptive moment estimation (ADAM) was selected as the optimizer to iteratively adapt the network's learning rate and early-stopping was used to prevent overfitting. Fine-tuning function of the TensorFlow library was used for the number of epochs varied from 100 to 1000 (epoch = 300 was the best one) and the learning rate (LR) from 10^{-6} to 10^{0} (LR = 0.0001 was the best one). Note that normalized datasets, with an interval of [0, 1], were used here so that the models could converge faster.

3.2.6. Mineral/pore Quantification and Surface Area Analysis

In this study, the performance of machine learning models for mineral/pore quantification and surface area analysis was evaluated. The porosity, mineral abundance, and mineral accessibility values were determined in predicted mineral maps and cross compared to the ground-truth data quantified from 2D labeled BSE-EDS images. The porosity values and volume fraction of mineral phases (mineral abundance) were determined by counting pore pixels and mineral pixels with the same color, respectively. The percentage of each mineral's surface that is adjacent to the pores (mineral accessibility) then were quantified by counting mineral pixels adjacent to pore pixels.

Here, accessibility is based on the assumption that all pores are connected or would be accessible to reactive fluids.

3.2.6.1. Ranked Mineral Dissolution Risk Assessment

Here, a new concept, a ranked mineral dissolution risk assessment map, that inherits the name and application from groundwater vulnerability and risk assessment maps but for mineral dissolution assessment, is introduced. The ranked mineral dissolution risk assessment map is used here as a means of evaluating the model predicted maps and checking their goodness of fit for extracting reactive sample characteristics not only pixel wise but also considering adjacent neighbors.

To create the ranked mineral dissolution risk assessment map, we first assigned a rank number to each pixel, ranging from 1 for less reactive minerals (i.e., quartz) to 14 for highly reactive ones (i.e., calcite, dolomite) for a specific set of conditions. Pores were assigned the highest (15) assigned rank number. The mineral rankings were based on dissolution rates obtained from Brantley (2008), Yadav and Chakrapani (2006), and Zhang et al. (2015) at pH 5 and a temperature of 298 K. Next, the pixel-wise risk number for each individual mineral was determined based on the highest adjacent ranked pixel to the pixel of interest.

The ranked mineral dissolution risk assessment map will help further assess the spatial distribution of reactivity risk for a given mineral and its evolution of risk. This map only considers the potential risk of being exposed to fluid to provide a conceptual reactive risk assessment map. The higher assigned rank, the higher the risk for the given pixel to be exposed to the fluid and to be involved in a rection over time compared to other pixels with similar mineralogy but less dissolvable adjacent neighbors.

3.2.7. Performance Metrics

To evaluate the performance of machine learning-based models, accuracy, precision, recall, and F1-score performance metrics were used. Precision calculates how often the model's prediction is correct over all positive predictions of a given class, whereas recall or sensitivity measures how accurate the model is in detecting true positive classes (relevant data). F1-score is the tradeoff between recall and precision and takes both *TP*, data points truly predicted as the class under consideration, and *FN*, incorrect rejection of that class, into account. They are defined as:

$$F1 = (2\times \text{precision} \times \text{recall})/(\text{precision} + \text{recall}) \quad (3)$$

$$\text{precision} = TP/(TP + FP) \quad (4)$$

$$\text{recall} = TP/(TP + FN) \quad (5)$$

The test image set was compared against the ground truth images to evaluate the models. To calculate the binary F1-score for each class, the given class was considered individually as positive, with the other classes as negative. Once the score was calculated for every class, their mean values were computed to evaluate the macro performance of the classifiers. However, this analysis does not consider a potential class imbalance among the samples as it weighs all classes equally. Thus, for a fairer global performance evaluation, we also estimated the overall statistics by computing the weighted average of each evaluation metric with respect to the representativity of each class.

3.3. **Results and Discussion**

3.3.1. Performance of the models on single and pooled datasets

This section investigates the effect of different image datasets with various grayscale distribution on the U-Net and Random Forest classifier's performances. Samples (i.e., individual sandstone

samples as well as the pooled dataset) had different image resolution, size, range of gray scale intensity, and several mineral components. Figure 3.2 presents the loss and accuracy of the trained U-Net model as a function of epoch for the pooled dataset. As shown, the loss in the pooled dataset decreases significantly after five epochs, while the accuracy of the U-Net model improves to around 96% after a few epochs. Similarly, the Random Forest classifier for the pooled dataset reaches an accuracy of 92%. A similar trend is obtained for individual datasets with accuracy ranging from 85% to 95%. The loss and accuracy plots for individual samples as well as for the pooled dataset for the Random Forest model are provided in the supplementary materials (Figures. S1 – S3).

By comparing the results of individual samples results (Figures. S1 – S3) with the pooled dataset (Figure 3.2), it can be concluded that using a larger dataset (i.e., pooled dataset) can improve the results. In general, the U-Net model trained on the pooled dataset reaches a lower loss value with fewer epochs, obtaining a higher accuracy and outperforming the individual datasets. The same is evident for the Random Forest model where the model trained on the pooled dataset achieves a better score compared to individual sets.

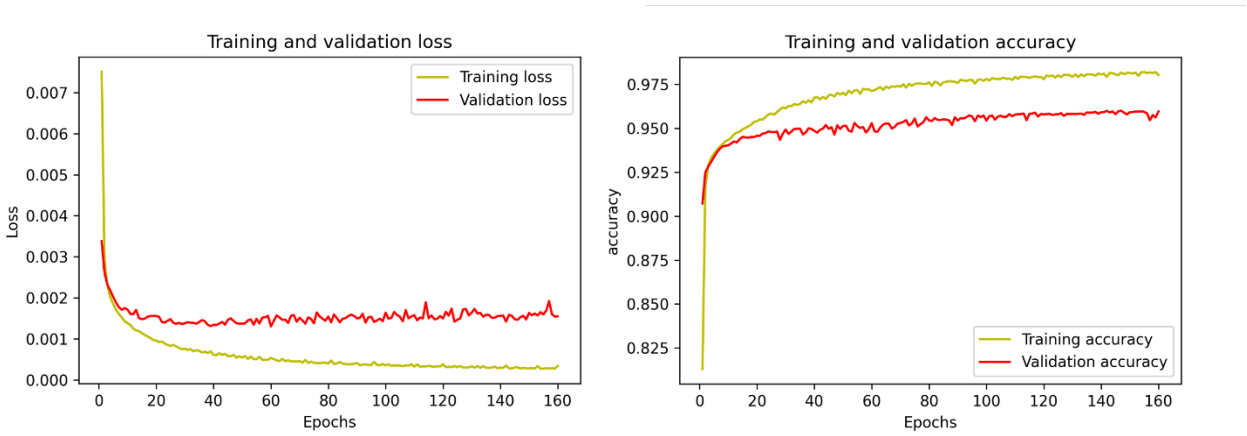

Figure 3.2. The accuracy and loss against the number of epochs for the U-Net model trained on pooled dataset.

3.3.2. Effect of input variable on the models' performance

The pooling of different sandstone samples together provides a dataset with varied grayscale intensity values but similar mineral characteristics such as mineral size, texture, patterns, etc. Therefore, to make a better prediction, machine learning algorithms must rely on the underlying patterns in addition to the BSE grayscale values. This section presents the models' performances on predicting mineral/pore classes with different input variable sets (i.e., BSE gray intensity, elemental EDS maps, and filter extracted features).

Figure 3.3 shows the F1-score of pores and mineral classes calculated for the predicted results of U-Net and Random Forest models on the pooled dataset. Different colors reflect different input variable sets, where the results of the Random Forest and U-Net classifiers trained with only the gray-scale BSE image (blue in Fig. 3.3) have 56% and 88% accuracy, respectively. As shown, the BSE-based model cannot predict minority classes such as zircon, chlorite, siderite and biotite and has a fair performance identifying albite due to its similar grayscale intensity as quartz.

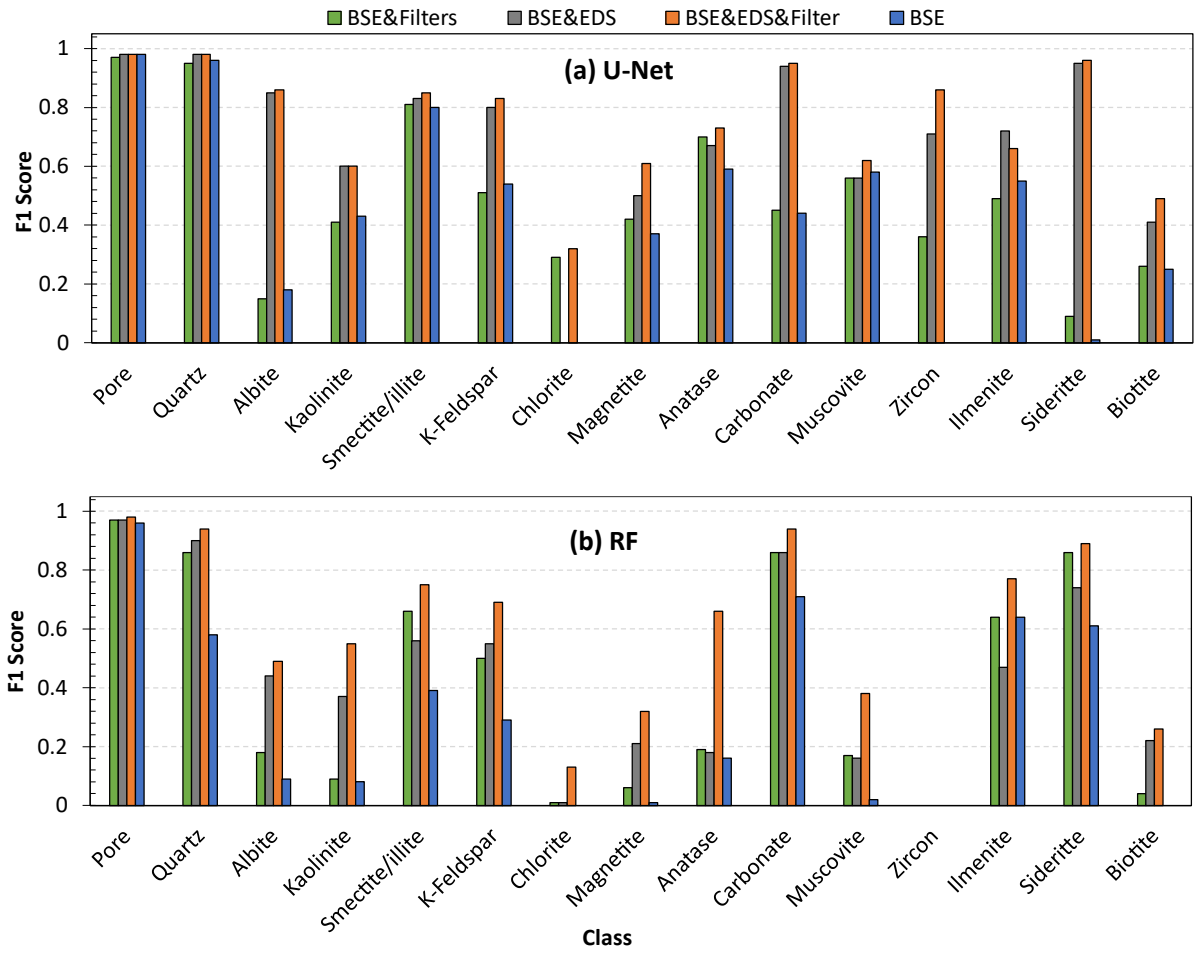

Figure 3.3. Performance of U-Net deep learning (a) and Random Forest machine learning (b) models for different mineral classes in pooled dataset.

When filter extracted features are considered in addition to the grayscale BSE images (green in Fig. 3.3), a higher performance for both models is evident. The filters extract features such as texture, size, edges, etc. which improve the predictive performance of the model, especially for minerals with similar grayscale intensity (e.g., quartz and K-feldspar). The performance of models in predicting chlorite, zircon, smectite/illite and muscovite significantly improved, particularly for the Random Forest model. The filtered-based model has a comparable performance to the BSE-EDS based model (the dark gray in Fig. 3.3), highlighting the significant improvement of mineral segmentation by simply utilizing filtering techniques. This is particularly valuable in cases when EDS elemental maps are not available.

Integrating the EDS elemental map and filtering techniques (in Fig 3.3) further improves the results by considering both extracted features and elemental maps along with the BSE values. The resulting accuracy improves from 56% to 92% for Random Forest and 88% to 96% for the U-Net model, which also is shown visually in Figure 3.4 and 3.5. This also has noted success in predicting phases with low volume fractions, minority classes. These phases are difficult to predict and result in low performance of the associated classes due to data scarcity. An improvement in prediction is evident in the pooled dataset using the BSE, EDS, and filter images as input. This results in prediction of minority classes such as chlorite that are not predicted by any other methods. In addition, the performance in predictions of muscovite is significantly higher than that in any other methods in both models. In summary, the pooled dataset with the BSE&EDS&Filter input variables set has the highest accuracy and F1-Score and thus was selected as the final model.

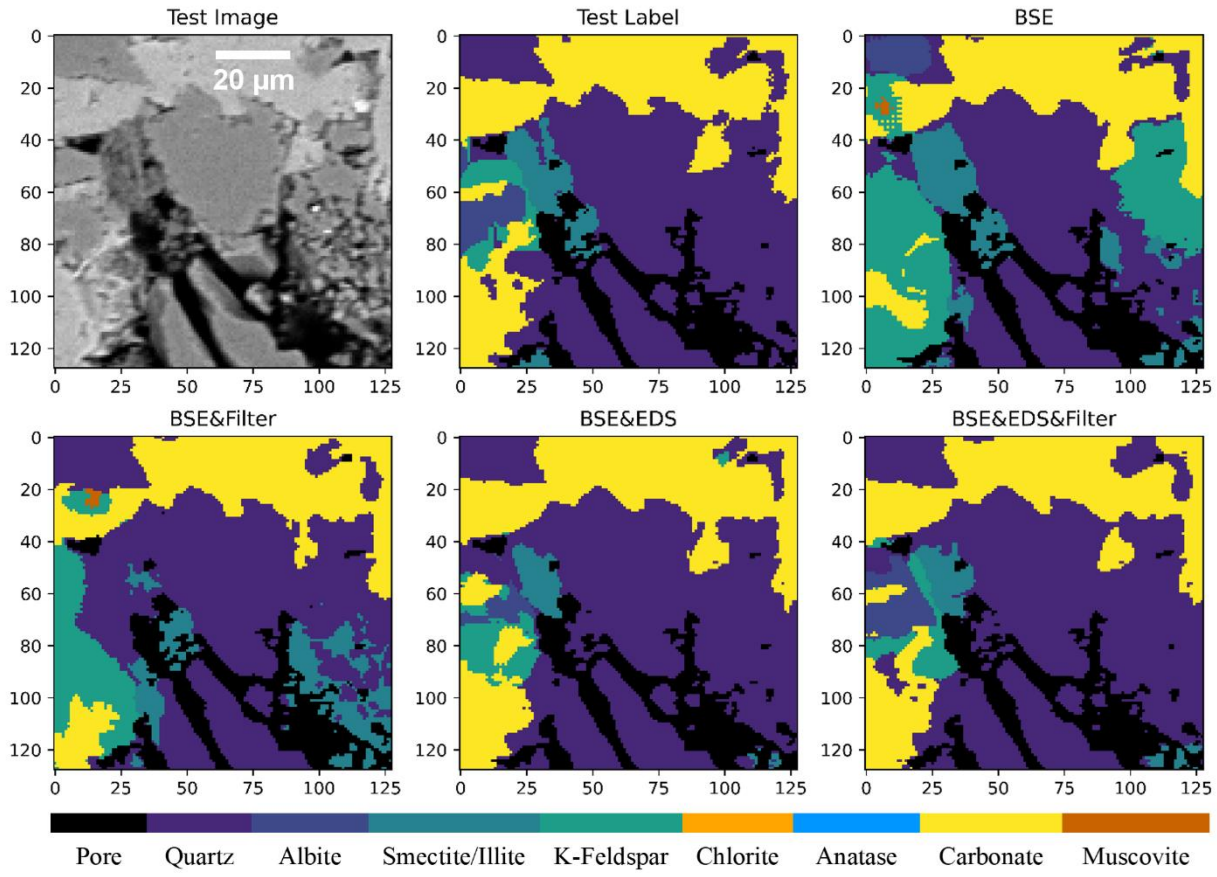

Figure 3.4. Visual performance of U-Net on different classes in the pooled dataset. Vertical and horizontal axes demonstrate pixel numbers with 0.71 µm resolution.

Both models show good performance for prediction of pore classes. Based on Figure 3.3, the "pore" class reaches a high F1-score of 96% to 98%. This highlights the capability of the models to automatically predict the sample pore pixels. Thus, obtained porosity values, which are an important characteristic of a sample and used in reactive transport simulations, are almost identical to the ground-truth data.

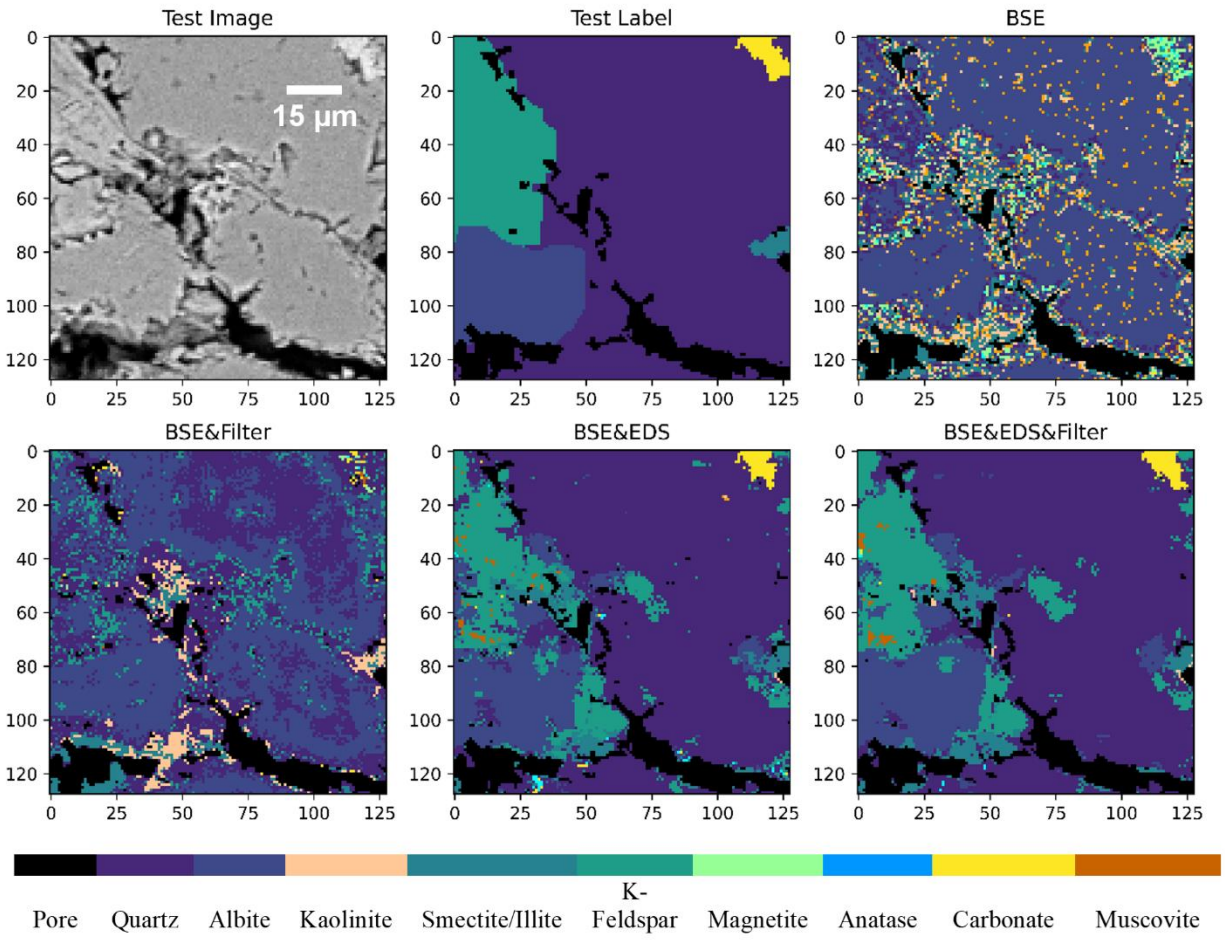

Figure 3.5. Visual performance of the RF model on different mineral classes in the pooled dataset. Vertical and horizontal axes demonstrate pixel numbers with 0.71 µm resolution.

The high F1-score accuracy for most of the classes obtained from the U-Net framework (i.e., the U-Net with pooled dataset and the BSE&EDS&Filter input variable set) reveals the robustness of the framework to various ranges of grayscale inputs since it relies more on extracted features and elemental maps. These features are also important in the Random Forest model where the "mean decrease in Gini Impurity" is used here to rank the input variables for the Random Forest model to determine the most important variables for mineral/pore segmentation. Figure 3.6 shows the resulting relative rank where the higher numbers indicate a higher contribution to successful classification. As shown, the median filter has the highest rank followed by the Ti

elemental map. The results reveal the higher contribution of elemental images and filter extracted features compared to the BSE gray scale values.

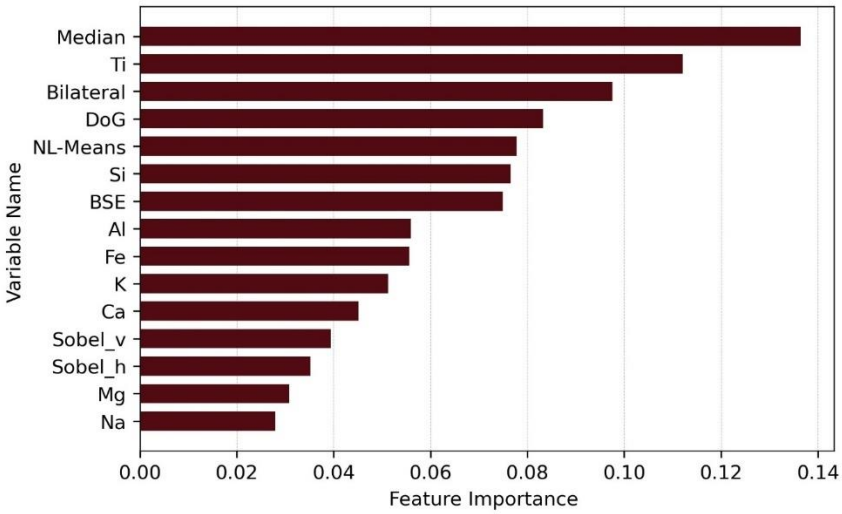

Figure 3.6. Rank of the input variables based on their contribution to improving segmentation (horizontal numbers are the rank of the variables called feature importance value).

3.3.3. Comparison of the Best Random Forest and U-Net Models

The SEM-BSE image dataset of the sandstone samples were processed and segmented for further mineral abundance and surface area analysis, using the best-trained models. Figure 3.7 compares the results of the best performing Random Forest and U-Net frameworks trained on the BSE&EDS&Filter input variable set of the pooled dataset. Although the pixel wise Random Forest classifier almost fails to predict some minority classes such as zircon and chlorite, it has an acceptable performance for the majority classes such as quartz (Figure 3.7). On the other hand, U-Net has a higher performance, especially for muscovite minority class, and can successfully detect different classes. U-Net preserves the structural dependency of pixels and considers the neighboring pixels by utilizing the convolutional kernels which helps detect continuous features such as edges and textures (Figure 3.8). Providing several extracted features helps the Random Forest model to consider this spatial dependency. Considering neighboring pixels and structural

dependency when making a prediction also helps overcome the noise (based on Figure 3.4, 3.5 and 8) that inherently exists in SEM-EDS image datasets and as a result improves prediction performance.

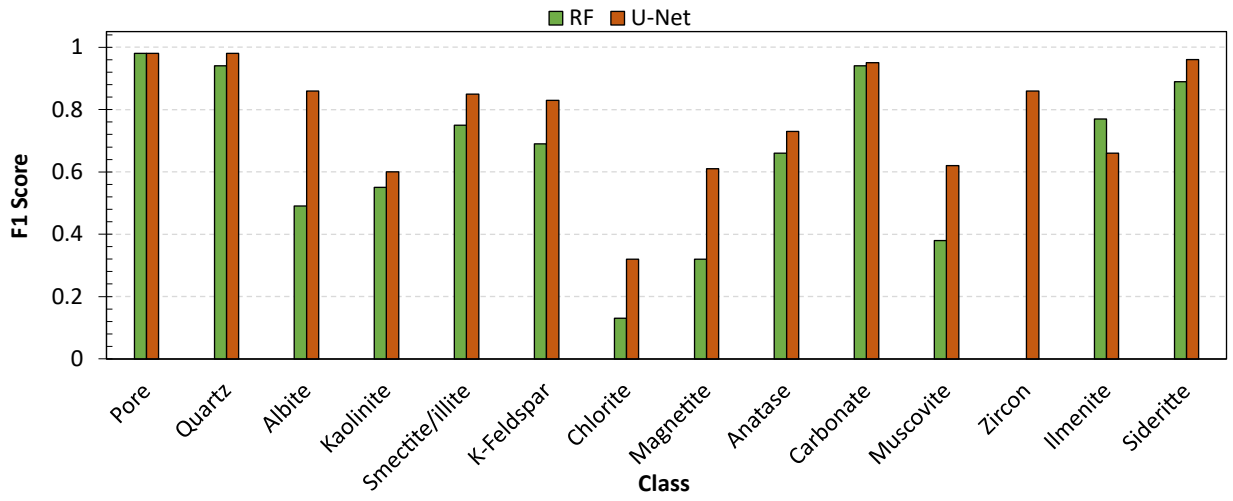

Figure 3.7. Comparison of the best performing U-Net and Random Forest models on predicting different mineral classes in pooled dataset.

Visualization of segmented quartz, albite, microcline, dolomite, kaolinite, llite/smectite, chlorite and pores within the samples (Fig. 3.4, 3.5 and 3.8 for a test subset of the samples) show that the most prevalent component of the samples is quartz, which is in agreement with XRD and ground truth data. Close inspection of these images also shows the promise machine learning has to classify variations in minerals at small scales, some of which may be missed in manual segmentation. Analysis of additional data extracted from segmented images are investigated in the next sections.

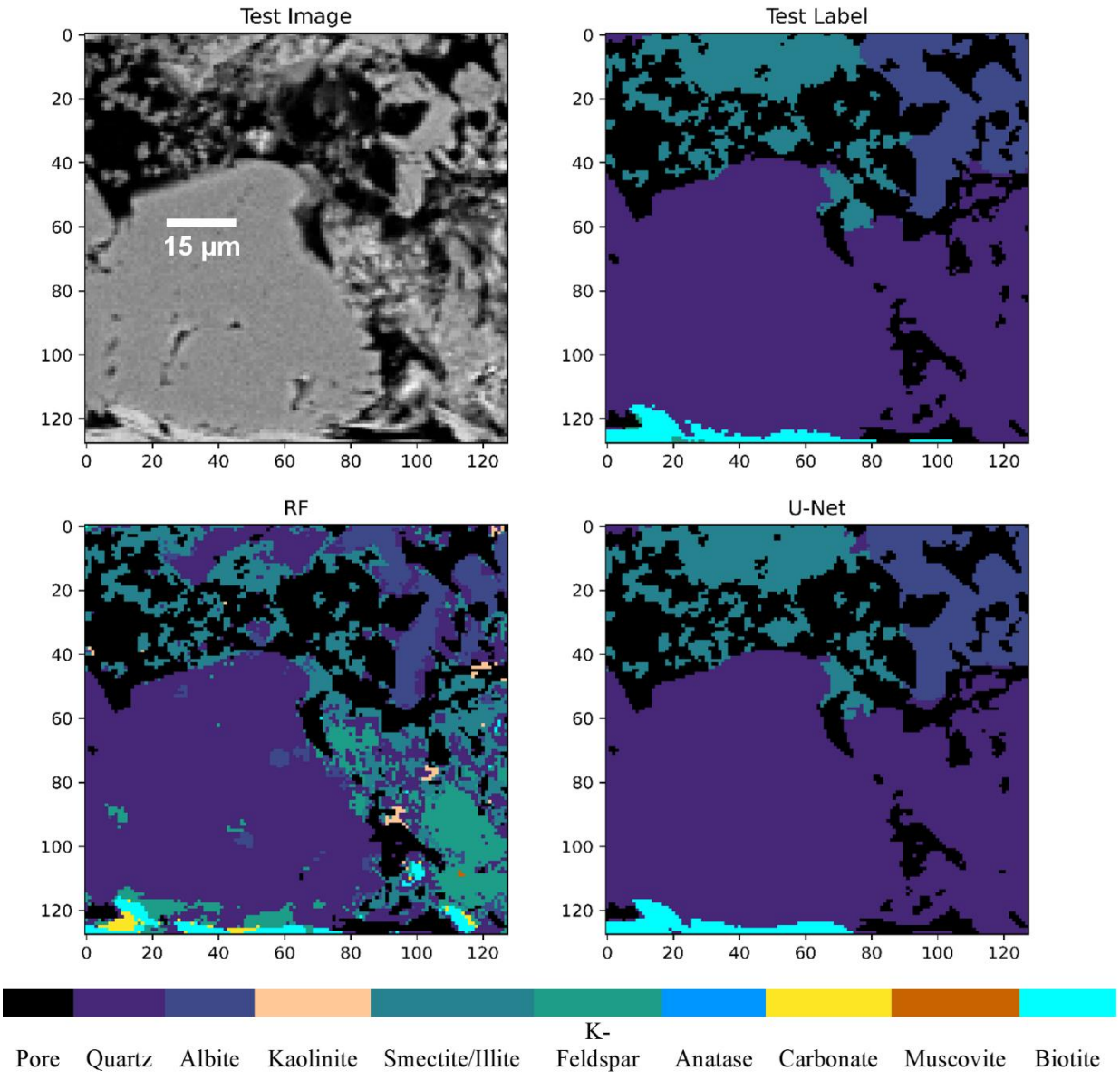

Figure 3.8. Visual comparison of the best performing U-Net and Random Forest models for predicting different mineral classes in pooled dataset. Vertical and horizontal axes demonstrate pixel numbers with 0.71 µm resolution.

3.3.4. Mineral/pore abundance and mineral accessibility analysis

The abundance and accessibility of minerals in segmented images for test dataset (15% of total images in pooled dataset) are given in Table 3.3. Results of mineral quantification indicate that overall quartz has the highest abundance among phases, followed by carbonate minerals (combined) and K-feldspar. This is also evident in the predicted results for individual datasets. Given the comparison of the results obtained from Random Forest and U-Net models with the ground truth data and considering abundance and accessibility as evaluation metrics, quartz (Abundance = 76.83% and Accessibility = 57.61%) is slightly underestimated (Abundance = 72.62% and Accessibility = 44.79%) by Random Forest and slightly overestimated by U-Net (Abundance = 77.72% and Accessibility= 55.86%). The results for other minerals, provided in Table 3.3, show a similar performance in which U-Net has a better result and less difference to the ground truth data compared to the Random Forest model predictions. Note that ground truth data was cross validated with XRD results and therefore U-Net model results is aligned with XRD data. In general, the observed differences in volume percentages are reasonable with most minerals within few percent agreement with the ground truth abundances. There is a larger variation evident among predicted accessibility with as much as 12% variation between predicted accessibility and the ground truth value with the largest difference for smectite/illite.

These results show the capability of machine learning models, especially U-Net, in characterizing geological samples to assess mineralogy and reactivity. A larger, balanced dataset with various mineral distributions could enhance model training and thus improve the results even further.

Table 3.3. Predicted abundance and accessibility values obtained from the models and the corresponding ground truth data.

Mineral	Rank	Chemical formula	Method	Abundance (%)	Accessibility (%)
Quartz	1	SiO_2	ground truth	76.83	57.61
			RF	72.62	44.79
			U-Net	77.72	55.86
Albite	11	$NaAlSi_3O_8$	ground truth	2.02	2.66
			RF	4.22	3.49
			U-Net	2.40	3.97
Kaolinite	5	$Al_2Si_2O_5(OH)_4$	ground truth	0.39	4.85
			RF	0.64	7.18
			U-Net	0.27	3.25
Anatase	3	TiO_2	ground truth	0.04	0.05
			RF	0.03	0.03
			U-Net	0.03	0.05
Carbonate	14	$CaCO_3/MgCO_3 \cdot CaCO_3$	ground truth	8.47	3.45
			RF	8.35	2.96
			U-Net	6.76	2.46
Biotite	8	$K(Mg,Fe^{++})_3[AlSi_3O_{10}(OH,F)_2$	ground truth	0.05	0.01
			RF	0.18	0.04
			U-Net	0.11	0.12
Muscovite	6	$KAl_2[AlSi_3O_{10}]$	ground truth	0.81	1.49
			RF	0.37	0.58
			U-Net	0.42	1.00
K-feldspar	10	$KAlSi_3O_8$	ground truth	3.86	3.30
			RF	4.12	2.07
			U-Net	4.82	3.98
Siderite	13	$Fe(Ca,Mg)(CO_3)_2$	ground truth	0.96	0.30
			RF	0.88	0.22
			U-Net	1.22	0.39
Smectite/Illite	9	$K_{0.65} Al_2 [Al_{0.65} Si_{3.35} O_{10}](OH)_2$	ground truth	6.45	25.79
			RF	8.18	37.90
			U-Net	5.99	28.08
Magnetite	12	Fe_3O_4	ground truth	0.09	0.32
			RF	0.36	0.39
			U-Net	0.20	0.57
Zircon	2	$ZrSiO_4$	ground truth	0.00	0.00
			RF	0.00	0.00
			U-Net	0.03	0.00
Ilmenite	4	$(Fe,Ti)_2O_3$	ground truth	0.03	0.08
			RF	0.03	0.06
			U-Net	0.02	0.04
Chlorite	7	ClO^-_2	ground truth	0.01	0.10
			RF	0.02	0.30
			U-Net	0.02	0.24

3.3.4.1. Mineral dissolution risk assessment map for potential reactive surface area evolution

This section compares and contrasts the obtained dissolution rank from the U-Net mineral/pore results with ground truth data. Figure 3.9 shows the potential dissolution rank for U-Net predicted K-feldspar mineral pixels obtained based on the maximum dissolution rank of neighboring pixels to the pixels of interest. As evident in the figure, variations in the dissolution risk ranking can be observed. Regions that are most available for reaction have the highest scores and are shown in blue. These surfaces are adjacent to pore space. Variations in the anticipated availability of other surfaces for reaction are indicated by varying color/risk number. Higher numbers are anticipated to be accessible for reaction more quickly than those with lower numbers.

The overall trend in the predicted image is similar to the ground truth image. This reveals the reliability of the U-Net model not only for predicting the mineralogy, and as a result, reactivity, of each pixel but also the ability of the trained framework to correctly predict neighboring pixels that may impact the potential reactivity of the pixels of interest. The results obtained based on this image show the U-Net predicted pore/mineral segmented map can be utilized to inform the reactive transport models over time scale.

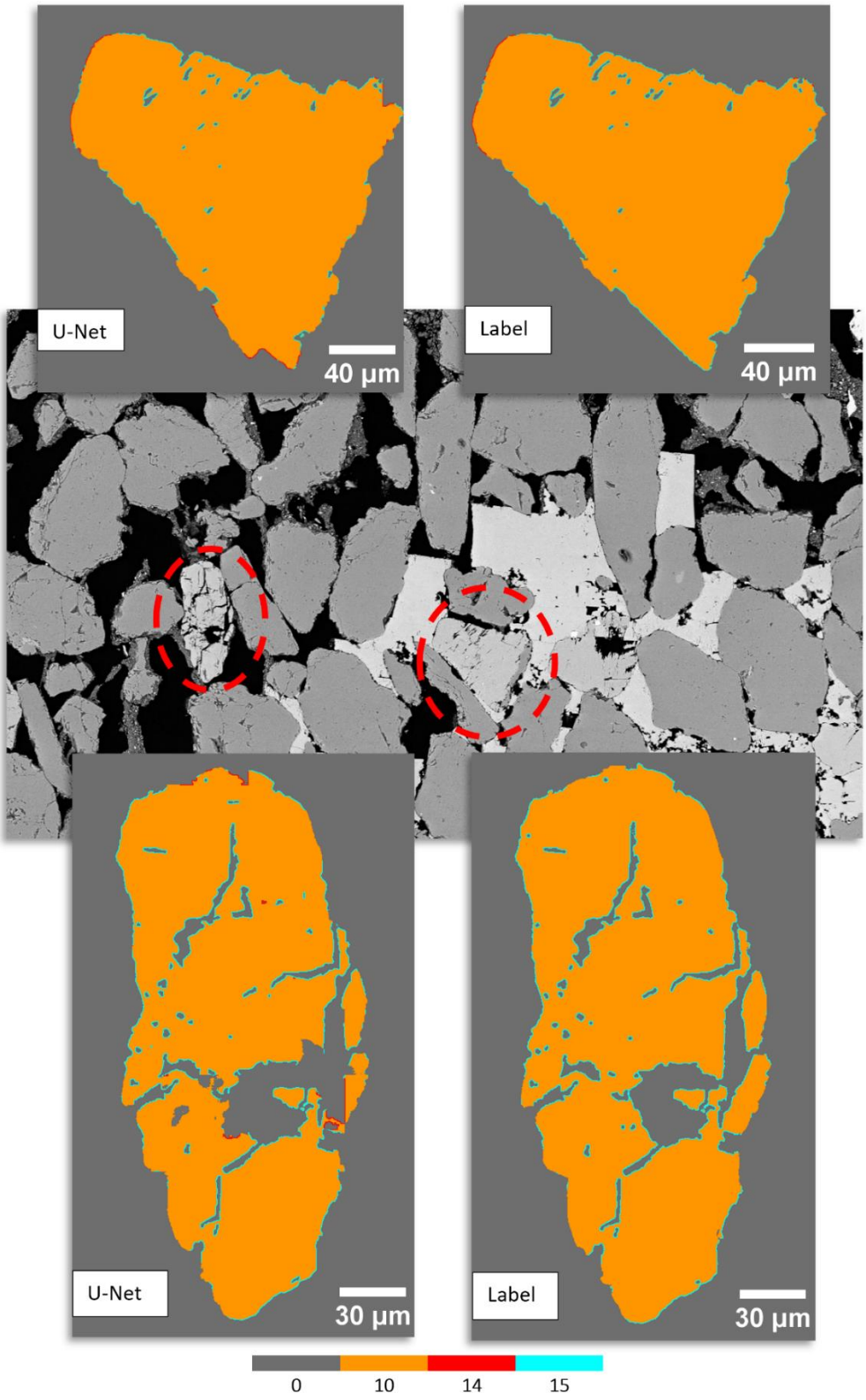

Figure 3.9. Ranked mineral dissolution risk assessment map for K-feldspar (rank 10) that is adjacent to rank 15 (pores) and 14 (carbonate), with 0.34 µm resolution. Rank zero shows pixels that are not on the surface of the mineral of interest.

3.4. **Conclusions**

This study evaluated the performance of Random Forest and U-Net models for mineral/pore phase segmentation and surface analysis of SEM images of various sandstone samples. This is achieved by providing a framework that not only evaluates the results on each pixel but also takes the predicted neighboring pixels into account. The performance of the models was investigated on a series of individual datasets as well as a combined dataset that included data from various samples, each with different grayscale intensity variation, in addition to EDS maps and filter data. It was shown that the performance of both platforms reaches the highest score when all BSE, EDS, filter data are used as input variables on the pooled dataset to train the models. Using those inputs, the U-Net model achieved the highest performance accuracy of 96%.

In general, the results from the U-Net model had a higher performance compared to the Random Forest model in predicting each class and thus a more reliable phase segmentation in different samples. In addition, the U-Net model had a better performance for surface quantification and had comparable results to the ground truth data for mineral abundances and accessibility. By comparing the results of the individual dataset to the pooled one, it can be concluded that using larger datasets (i.e., pooled dataset) can improve the results even further which is an inherent characteristic of machine learning models.

The results obtained from comparing the models with different input variable sets showed the trained models relied more on extracted features and information obtained from EDS elemental maps. Feature importance ranking in the Random Forest model confirmed this conclusion. It also showed the median and gaussian filters had the highest contribution in phase segmentation due to removing unwanted noise and providing more integrated phases. Relying on extracted features

provided a more robust solution to grayscale variation from one dataset to another since the grayscale intensity may vary but extracted features are more or less similar in different datasets.

Finally, the mineral risk assessment map was proposed. This provided a robust solution to identify the locations susceptible for dissolution and is recommended to be used in conjunction with the machine learning platforms. This map can capture variations in surface reactivity due to differences in accessibility where some surfaces are in contact with pores and thus accessible for reaction while others are occluded by mineral coatings. Occluded surfaces will be accessible for reaction once the coating phase dissolves. This may be a promising approach to considering the potential evolution of reactive surfaces.

The intelligent segmentation and surface analysis framework in this work is promising for accelerating the processing of SEM data as well as reducing the need for post-process filtration. The obtained parameters can be utilized to enhance understanding of sample characteristics including mineralogy as well as reactive properties. Data such as porosity and mineral volume fractions can be quantified from processed maps and used to inform reactive transport simulations.

Acknowledgement

This material is based upon work supported by the National Science Foundation under Grant No: 1847243

Supplementary and codes

The labeling and Normalizing&Cropping, Filtering, Accessibility&Abundance_Total, and ranked mineral dissolution risk assessment map codes and images can be found at https://github.com/Parisa-Asadi/Machine-learning-for-Surface-Areas-Analysis.

3.5. **References**

- Asadi, P., & Beckingham, L. E. (2021). Integrating Machine/Deep Learning Methods and Filtering Techniques for Reliable Mineral Phase Segmentation of 3D X-ray Computed Tomography Images. Energies, 14(15), 4595.
- Asadi, P., & Tian, D. (2021). Estimating leaf wetness duration with machine learning and climate reanalysis data. Agricultural and Forest Meteorology, 307, 108548.
- Anovitz, L. M., Beckingham, L. E., Sheets, J. M., & Cole, D. R. (2022). A Quantitative Approach to the Analysis of Reactive Mineralogy and Surface Area. ACS Earth and Space Chemistry, 6(2), 272-287.
- Brantley, S. L. (2008). Kinetics of mineral dissolution. In Kinetics of water-rock interaction (pp. 151-210). Springer, NY, USA.
- Bradski, L. (2001). Random forests. Machine learning, 45(1), 5-32.
- Bradski, G., & Kaehler, A. (2008). Learning OpenCV: Computer vision with the OpenCV library. O'Reilly Media, Inc. Ca, USA.
- Beckingham, L.E., Steefel, C.I., Swift, A.M., Voltolini, M., Yang, L., Anovitz, L.M., Sheets, J.M., Cole, D.R., Kneafsey, T.J., Mitnick, E.H. and Zhang, S. (2017). Evaluation of accessible mineral surface areas for improved prediction of mineral reaction rates in porous media. Geochimica et Cosmochimica Acta, 205, 31-49.
- Brunhoeber, O. M., Anovitz, L. M., Asadi, P., & Beckingham, L. E. (2021). Role of mineralogy in controlling fracture formation. ACS Earth and Space Chemistry, 5(11), 3104-3114.

- Chen, X. Y., Teng, F. Z., Huang, K. J., & Algeo, T. J. (2020a). Intensified chemical weathering during Early Triassic revealed by magnesium isotopes. Geochimica et Cosmochimica Acta, 287, 263-276.
- Chen, Z., Liu, X., Yang, J., Little, E., & Zhou, Y. (2020b). Deep learning-based method for SEM image segmentation in mineral characterization, an example from Duvernay Shale samples in Western Canada Sedimentary Basin. Computers & Geosciences, 138, 104450.
- Deng, H., Fitts, J. P., Tappero, R. V., Kim, J. J., & Peters, C. A. (2020). Acid erosion of carbonate fractures and accessibility of arsenic-bearing minerals: In Operando synchrotron-based microfluidic experiment. Environmental Science & Technology, 54(19), 12502-12510.
- Esene, C., Zendehboudi, S., Aborig, A., & Shiri, H. (2019). A modeling strategy to investigate carbonated water injection for EOR and CO_2 sequestration. Fuel, 252, 710-721.
- Guan, S. (2012). Modeling geomechanical property changes using well logging and pressure data in a carbon dioxide enhanced oil recovery reservoir. ProQuest LLC. Co, USA.
- Iloejesi, C. O., & Beckingham, L. E. (2021a). Assessment of geochemical limitations to utilizing CO_2 as a cushion gas in compressed energy storage systems. Environmental engineering science, 38(3), 115-126.
- Iloejesi, C. O., & Beckingham, L. E. (2021b). Influence of storage period on the geochemical evolution of a compressed energy storage system. Frontiers in Water, 3, 100-113.
- Koohi-Fayegh, S., & Rosen, M. A. (2020). A review of energy storage types, applications and recent developments. Journal of Energy Storage, 27, 101047.
- Kim, J. J., Ling, F. T., Plattenberger, D. A., Clarens, A. F., Lanzirotti, A., Newville, M., & Peters, C. A. (2021). SMART mineral mapping: Synchrotron-based machine learning

approach for 2D characterization with coupled micro XRF-XRD. Computers & Geosciences, 156, 104898.

- Karimpouli, S., & Tahmasebi, P. (2019). Segmentation of digital rock images using deep convolutional autoencoder networks. Computers & geosciences, 126, 142-150.
- Li, C., Wang, D., & Kong, L. (2021). Application of machine learning techniques in mineral classification for scanning electron microscopy-energy dispersive X-ray spectroscopy (SEM-EDS) images. Journal of Petroleum Science and Engineering, 200, 108178.
- Luhmann, A. J., Tutolo, B. M., Bagley, B. C., Mildner, D. F., Seyfried Jr, W. E., & Saar, M. O. (2017). Permeability, porosity, and mineral surface area changes in basalt cores induced by reactive transport of CO_2-rich brine. Water Resources Research, 53(3), 1908-1927.
- Landrot, G., Ajo-Franklin, J. B., Yang, L., Cabrini, S., & Steefel, C. I. (2012). Measurement of accessible reactive surface area in a sandstone, with application to CO_2 mineralization. Chemical Geology, 318, 113-125.
- Ma, J., Ahkami, M., Saar, M. O., & Kong, X. Z. (2021). Quantification of mineral accessible surface area and flow-dependent fluid-mineral reactivity at the pore scale. Chemical Geology, 563, 120042.
- Mahdikhani, M., Bamshad, O., & Shirvani, M. F. (2018). Mechanical properties and durability of concrete specimens containing nano silica in sulfuric acid rain condition. Construction and Building Materials, 167, 929-935.
- Mohammadian, E., Kheirollahi, M., Liu, B., Ostadhassan, M., & Sabet, M. (2022). A case study of petrophysical rock typing and permeability prediction using machine learning in a heterogenous carbonate reservoir in Iran. Scientific Reports, 12(1), 1-15.

- Pirrie, D., Butcher, A. R., Power, M. R., Gottlieb, P., & Miller, G. L. (2004). Rapid quantitative mineral and phase analysis using automated scanning electron microscopy (QemSCAN); potential applications in forensic geoscience. Geological Society, London,UK. Special Publications, 232(1), 123-136.
- Pedregosa, F., Varoquaux, G., Gramfort, A., Michel, V., Thirion, B., Grisel, O., Blondel, M., Prettenhofer, P., Weiss, R., Dubourg, V. & Vanderplas, J. (2011). Scikit-learn: Machine learning in Python. The Journal of Machine Learning Research, 12, 2825-2830.
- Peters, C. A. (2009). Accessibilities of reactive minerals in consolidated sedimentary rock: An imaging study of three sandstones. Chemical Geology, 265(1-2), 198-208.
- Qin, F., & Beckingham, L. E. (2019). Impact of image resolution on quantification of mineral abundances and accessible surface areas. Chemical Geology, 523, 31-41.
- Ronneberger, O., Fischer, P., & Brox, T. (2015, October). U-net: Convolutional networks for biomedical image segmentation. In International Conference on Medical Image Computing and Computer-assisted Intervention (pp. 234-241). Springer, Cham. London, UK.
- Salek, Md. F., Qin, F., Asadi, P., Iloejesi, C., Brunhoeber, O., Mahmood, M., Beckingham, L.E. (2022). Impact of pore connectivity on quantification of mineral accessibility in sandstone samples. ACS Earth Space Chemistry . Submitted.
- Soong, Y., Howard, B.H., Dilmore, R.M., Haljasmaa, I., Crandall, D.M., Zhang, L., Zhang, W., Lin, R., Irdi, G.A., Romanov, V.N. and Mclendon, T.R. (2016). CO_2/brine/rock interactions in Lower Tuscaloosa formation. Greenhouse Gases: Science and Technology, 6(6), 824–837.

- Seyyedi, M., Sohrabi, M., Sisson, A., & Ireland, S. (2018). Quantification of oil recovery efficiency, CO_2 storage potential, and fluid-rock interactions by CWI in heterogeneous sandstone oil reservoirs. Journal of Molecular Liquids, 249, 779-788.
- Suthaharan, S. (2016). Machine learning models and algorithms for big data classification. Integr. Ser. Inf. Syst, 36, 1-12.
- Van der Walt, S., Schönberger, J.L., Nunez-Iglesias, J., Boulogne, F., Warner, J.D., Yager, N., Gouillart, E. & Yu, T. (2014). scikit-image: image processing in Python. PeerJ, 2, e453.
- Yadav, S. K., & Chakrapani, G. J. (2006). Dissolution kinetics of rock–water interactions and its implications. Current Science, 932-937.
- Yoon, H., Melander, D., & Verzi, S. J. (2021, March). Machine learning application for permeability estimation of three-dimensional rock images. In The AAAI 2021 Spring Symposium on Combining Artificial Intelligence and Machine Learning with Physical Sciences (AAAI-MLPS 2021), Stanford, CA, USA, http://ceur-ws.org/Vol-2964/article_191.pdf.
- Zhang, Y., Chen, J., & Li, Y. (2022). Segmentation and quantitative analysis of geological fracture: a deep transfer learning approach based on borehole televiewer image. Arabian Journal of Geosciences, 15(3), 1-17.
- Zhang, S., Yang, L., DePaolo, D. J., & Steefel, C. I. (2015). Chemical affinity and pH effects on chlorite dissolution kinetics under geological CO_2 sequestration related conditions. Chemical Geology, 396, 208-217.

CHAPTER 4

MODELING THE SPATIAL AND TEMPORAL EVOLUTION OF FRACTURED SYSTEMS WITH HETEROGENOUS MINERALOGY

Abstract

Reactive transport modeling has been extensively used to enhance understanding of geochemical reactions and transport phenomena in a wide variety of surface and subsurface systems including fractured systems. Mineral dissolution and precipitation reactions in fractures may alter fracture apertures, enhancing or reducing permeability. This, however, is not well understood. Recent work has shown fractures form preferentially in clay-rich regions such that the fracture surface mineralogy is not well reflected by the bulk mineralogy. Implications of this observation on the reactive evolution of the fracture and matrix are considered in this work. Reactive transport simulations with varying distributions of surface and matrix mineralogy are carried out and cross-compared for a Mancos shale sample. Simulations are initialized using observation of a clay-rich region near the fracture surface extracted from prior analysis of a mechanically induced fracture. These simulations are compared with those considering homogenous mineral distributions given by bulk XRD data and prior imaging of the bulk sample matrix. Temporal and spatial variations in simulation results for different cells were in all simulations with more extensive reactions in cells close to the inlet and fracture surface. The highest simulated change in porosity, mineral composition and ion concentration in all simulations happened in cells adjacent to the fracture at the system inlet. Comparison of simulation results for the three systems showed variation in

simulated mineral and porosity evolution. For long-time simulations, the extent of mineral dissolution and consequently porosity increase was faster for simulations reflecting mineral heterogeneity with a clay-rich near fracture region followed by those using XRD and image obtained matrix homogenous mineralogy. A sensitivity analysis for mineral surface area (SA) was carried out and showed consistent results for simulations conducted using the low and high BET SA values at short times (days) but large variations over longer timescales (years). The results could improve our ability to predict reactive fracture evolution and understand its implications for subsurface CO_2 sequestration and oil recovery.

4.1. **Introduction**

The global temperature has increased mainly due to the increase in CO_2 emissions from human activities. Geologic CO_2 sequestration offers an efficient and sustainable solution for reducing atmospheric CO_2 levels. The rapid development of subsurface organic-rich shales for hydrocarbon recovery in past years has opened up the possibility of utilizing these hydraulically fractured shale reservoirs as potential target reservoirs for CO_2 sequestration. Shales have a low permeability and high sealing capacity which make it a potential candidate for CO_2 sequestration given porosity is increased by artificial fracturing. With the right reservoir conditions, injection of CO_2 into shale reservoirs can result in incremental oil recovery and permanent storage of CO_2 in geological formations *(Kumar et al., 2022)*. Shales are also important caprock formations for sequestration in saline aquifers where fractures may pose a risk to the permanence of storage. To evaluate the CO_2 sequestration potential and security of these fractured networks, we need to better understand the geochemical reactions at CO_2–fluid–shale interfaces and how they affect the flow and

CO_2 storage permanence. Thus, it is important to understand the heterogeneity and complexities associated with component properties and the evolution of shale in these networks.

In these fractured heterogenous networks, mineral dissolution and precipitation reactions may potentially alter fracture apertures. When CO_2 is injected, it can dissolve into formation brine, lowering pH and creating conditions favorable for dissolution of primary minerals *(Beckingham et al., 2017; Qin and Beckingham, 2020; Iloejesi and Beckingham 2021a&b; Wu et al., 2019; Steel et al., 2016; Du and Nojabaei, 2020; Steefel and Hu, 2022)*. As reactions progress, the pH can be buffered by carbonate mineral dissolution and create conditions favorable for precipitation of secondary minerals. These mineral reactions may occur on fracture surfaces or in the low permeability matrix adjacent to fractures and will impact fracture permeability *(Ellis et al., 2011; Deng et al., 2013; Ellis and Peters 2016; Steel et al., 2016; Du and Nojabaei, 2020; Steefel and Hu, 2022).*

Previous research studies showed rock composition plays a critical role in fracture development *(Guo et al 2015; Tian and Daigle, 2019; Ding et al 2012; Yoon et al 2019; Gale 2017; Na et al 2017)*. Brittle minerals such as silica, feldspar, carbonate tend to produce many highly conductive fractures under stress *(Ding et al 2012; Khan et al 2021)*, whereas ductile mineral contents such as organic matter or clay are more prone to form microfractures *(Bourg, 2015; Li et al 2021)*. These observations show the importance of mineral components in fracture formation.

Reactive transport modeling is an essential tool to simulate complex geochemical reactions in porous media that can impact formation properties. To date, most of the reactive transport modeling research on heterogeneous shale formations have focused on mechanical properties. Few studies have considered relationships between fracture surface mineralogy and the fracture

evolution or propagation *(Ding et al 2012; Gale 2017; Bourg 2015; Detwiler and Morris, 2018)* with most simulations simplified by considering bulk formation mineralogy data obtained from XRD information. However, this may not accurately reflect the reactive minerals as bulk mineralogy does not consider mineral distribution, which may result in simulations unable to accurately reflect actual mineral reactions that will occur. Physical heterogeneity, such as heterogeneity in fracture permeability, is also controlled by the spatial variation of mineralogy (*Ellis et al., 2011)* which is not reflected in simulations using homogenous mineralogy distributions based on bulk sample analyses.

Mineral distribution also has an important role in controlling fracture formation. Several studies *(Kuva 2012; Ding et al 2012; Gale 2017; Bourg 2015; Busch et al., 2021)* have noted a relationship between individual mineral grains and the locations where fractures form, mostly focusing on the general mineral sealing capabilities or composition in which fractures tend to form. Beyond the general composition of fracture surfaces, the amount and distribution of reactive minerals on fracture surfaces plays an important role in controlling the reactive evolution of fractures *(Brunhoeber et. al. 2021; Spokas et al., 2018)*. Although there are some recent research studies developing rate laws to take heterogeneity into consideration *(Salehikhoo and Li, 2015; Beckingham et al., 2017; Atchley et al., 2014; Beckingham et al., 2016; Jung and Navarre-Sitchler, 2018; Wen and Li, 2018; Qin and Beckingham, 2021)*, the enhancement or reduction of fracture aperture and permeability by mineral dissolution or precipitation on the fracture surfaces *(Bourg 2015)* is not well understood and exploration of the evolution of these heterogeneous domains has been relatively limited. In addition, no study has particularly investigated the impact of varying multi-mineralic fracture surface and matrix compositions on the reactive evolution of the fracture and surrounding matrix.

The objective of this work is to evaluate the impact of variations in mineralogy of the fracture surface and surrounding matrix on simulated mineral reactions and reaction rates between minerals and CO_2 saturated brine. Mineral composition and distribution measured from image analyses of SEM-BSE images *(Brunhoeber et. al. 2021)* are first used here to evaluate geochemical reactions and the system evolution given observed differences in mineral composition on the fracture surface as compared to that of the bulk sample using reactive transport simulations. Simulations consider the extent of mineral reaction, reaction rates and fracture surface evolution in the context of geologic CO_2 storage at two timescales, a short (days) time scale and a long (years) time scale that are pertinent for understanding reactions for typical laboratory experiments and field conditions, respectively. Complementary simulations are then carried out using mineralogy of the matrix determined from analysis of SEM images *(Brunhoeber et al. 2021)* and bulk XRD of the sample. Simulation results, including the evolution of mineral volume fractions, major ion concentrations, pH, porosity and mineral volume fraction and ion concentrations are then compared. Our goal is to improve our ability to predict reactive fracture evolution and understand its implications for subsurface CO_2 sequestration and oil recovery.

4.2. **Data and Methodology**

4.2.1. Sample

In this work, observations of a Mancos shale sample from our previous work *(Brunhoeber et al. 2021)* are used. This formation is stratigraphically located in the Mid-western United States. In Brunhoeber et al. (2021), shale core samples 1” by 2” were purchased from Kocurek Industries Inc. Samples were fractured by applying unconfined uniaxial compressive stress to each sample

using an Instron 1321 test frame, both with 100kN load cell and equipped with spherical seated compression plates. Polished thin sections were created of the rock matrix parallel and perpendicular to the fracture surface (Applied Petrographic Services Inc). The parallel thin sections were taken ~10 and 15 millimeters away from the fracture. The Mancos fracture surface and thin sections were imaged using a Zeiss EVO 50 Variable Pressure Scanning Electron Microscope at Auburn University. The mineralogy, mineral abundances, and mineral volume fractions determined from analysis of the 2D SEM images (Fig. 4.1 a,b) as well as X-ray Powder Diffraction (XRD) information analysis for the bulk sample *(Brunhoeber et al 2021)* were used here and are reported in Table 1. Mineral volume fractions are defined as mineral volume percentage within the porous medium (m^3 mineral volume/m^3 total porous medium volume).

In Brunhoeber et al (2021), it was observed that concentrations of clay minerals were enhanced near the fracture surface with respect to the bulk sample and that the fracture was most likely to form at kaolinite-kaolinite interfaces. Evaluation of the mineralogical spatial variability through cross-correlation analysis of the surrounding matrix in images of samples cut perpendicular to the fracture showed that clay was 16.7 times more likely to be present than carbonate minerals near the fracture surface *(Brunhoeber et al 2021)*. The high correlation persists roughly 200 microns into the surrounding matrix for the Mancos sample and implies that the fracture formed within a defined clay-rich lithofacies *(Brunhoeber et al 2021)*.

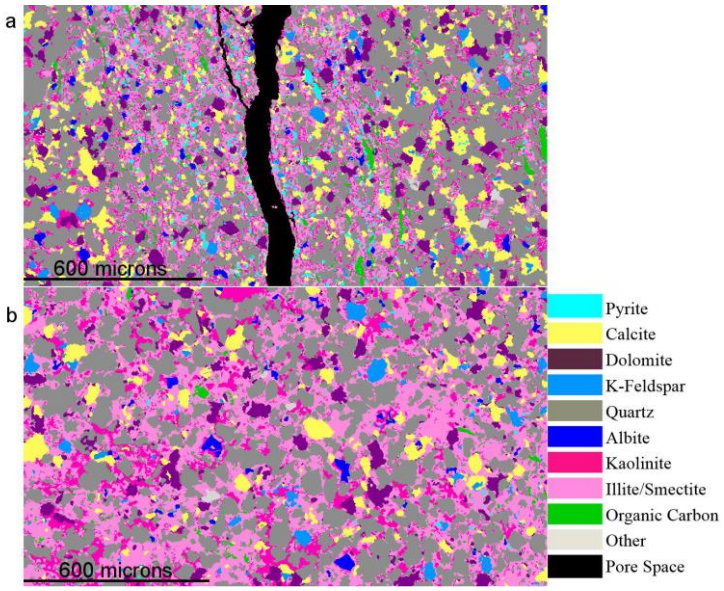

Figure 4.1. Processed SEM-EDS mineral maps of the near fracture matrix. (a) shows the matrix perpendicular to the imaged fracture surface, and (b) shows the matrix parallel to the fracture (Brunhoeber et. al. 2021).

Table 4.1 Mineral volume fractions calculated from Brunhoeber et. al. (2021), specific surface area and rate constants for reactive transport simulations at reservoir condition as obtained from the literature muscovite (Oelkers et al., 2008), kaolinite (Carroll and Walther, 1990; Ganor et al., 1995), illite (Gu and Evans, 2007), K-Feldspar (Bevan and Savage, 1989), albite (Chen and Brantley, 1997), quartz (Knauss and Wolery, 1988; Brady and Walther, 1990), pyrite and dolomite (Palandri and Kharaka, 2004), and calcite (Alkattan et al., 1998). The clay-rich region refers to the 200-micron region surrounding the fracture surface and the surrounding matrix is the matrix >200 microns from the fracture surface.

	Volume fraction (%)				Surface area		Rate constant
Minerals	**XRD**	**Images of matrix parallel to the fracture**	**Images perpendicular to fracture**		**SSA low BET (m^2/g)**	**SSA high BET(m^2/g)**	**Log k (T = 50 °C)**
			Clay-rich region	Surrounding matrix			
Muscovite	6.768	-	-	-	1.1	3.4	-12.67
Kaolinite	3.008	9.6538	60.5518	8.8938	3.17	19.5	-12.43
Illite	7.614	32.9292	0	19.5663	42	66.8	-13.35
K Feldspar	6.298	1.927	1.6264	1.7367	0.112	1.52	-11.65
Albite	7.52	1.034	0.282	1.3472	0.04	0.49	-11.11
Quartz	48.974	36.3404	14.9194	46.5001	0.0225	0.11	-11.6
Pyrite	0.094	0.1034	1.2127	2.3155	0.03	2.8	-7.9
Calcite	7.52	5.3298	9.495	10.3041	0.0139	1.64	-4.21
Dolomite	6.204	5.7152	1.852	5.9678	0.06	0.065	-4.8

4.2.2. Reactive transport simulations

4.2.2.1. Model description

CrunchFlow *(Steefel et al., 2015)* was used to build a reactive transport model coupling the solute transport, flow, and multiple species kinetic evolution for a CO_2-saturated brine injection system with various defined mineralogy (Fig. 4.2). CrunchFlow is a general-purpose continuum scale multicomponent reactive transport simulator that handles advective, diffusive, and dispersive transport and an arbitrary number of mixed equilibrium and kinetic reactions. The software is able to simulate single-phase flow in heterogeneous domains, including fracture flow *(Steefel & Lichtner, 1998)*.

Here, two-dimensional transient reactive transport model systems were developed (Fig. 4.2). Models consisted of a matrix of 3 × 5 grid cells proceeded by a 'ghost' cell (treated as a boundary condition) containing a constant partial pressure of CO_2 in equilibrium with formation brine that acted as a constant source of CO_2-saturated brine throughout the simulations. Cells were 3-millimeter long and 0.2-millimeter wide for both the fracture and clay-rich area (Fig. 4.2) and 1.8-millimeter width for the surrounding matrix cells.

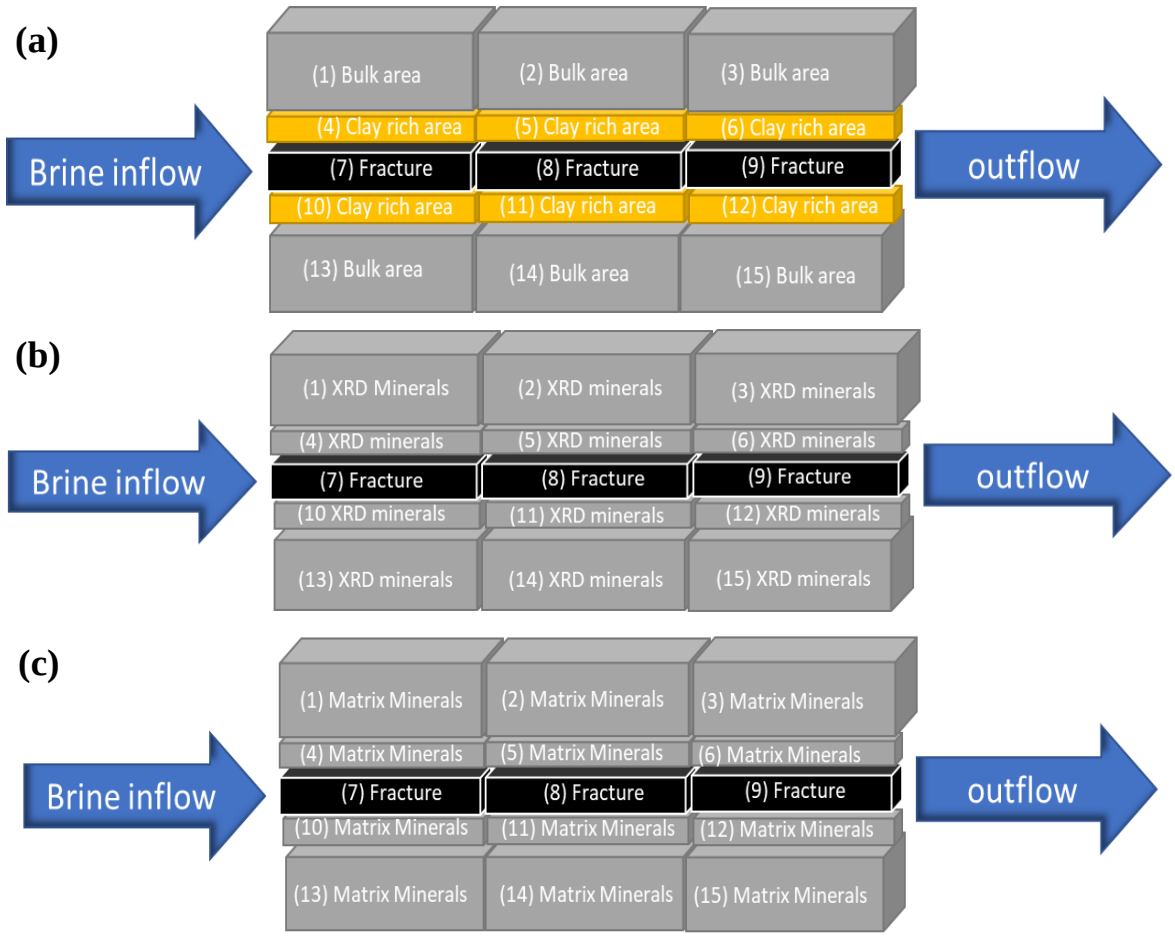

Figure 4.2. Diagram of the simulation system where a) corresponds to mineralogy determined from images perpendicular to the fracture, b) reflects mineralogy determined from bulk XRD analysis of the sample, and c) captures mineralogy observed in images of the matrix in a sample parallel to the fracture.

The mineral cells were initialized based on mineral volume fractions determined from imaging analysis of thin sections in Brunhoeber et. al. (2021) and XRD information *(Brunhoeber et. al. 2021, Asadi and Beckingham 2021)*, given in Table 4.1. Three model scenarios with varying mineralogy were considered. This included a simulation with heterogenous mineral distribution informed by images perpendicular to the fracture which reflects the clay-rich near fracture regions and models with homogenous distributions of mineralogy as given by bulk XRD analysis and imaging of the matrix in a sample parallel to the fracture. For the heterogenous system (Figure 4.1a), the mineral cells consist of clay-rich cells near the fracture (cells from 4 to 6 and 10 to 12)

with 60.55% kaolinite, fracture cells (cells from 7 to 9) with 0.2-millimeter width and surrounding matrix cells with 46.5% quartz (cells from 1 to 3 and 13 to 15). This scenario is representative of real observed and quantified mineral distributions around the fracture compared to the other scenarios that simulate the bulk mineralogy. For the homogenous scenarios, the mineral cells have uniform composition initialized either using mineral volume fractions determined from the XRD analysis or images of the matrix in samples parallel to the fracture (Table 4.1). The XRD volume fractions consist predominantly of quartz (48.97%) with ~15% feldspar minerals and relatively equal amounts (6-7%) of muscovite, illite, calcite, and dolomite while the mineral composition of the matrix determined from the image mainly consists of quartz (36.34%) and illite (32.92%).

Simulations consider the flow of the CO_2 acidified brine through the domain starting from a time of 0 hours, reflecting field conditions and tracking the concentration of major ion species, mineral volume fractions, and porosity. The corresponding estimated temperature and pressure at the sample depth, 1066 m, is 50 ˚C and 100 bar, calculated based on a temperature gradient of 25 ◦C/km and surface temperature of 25 ˚C and pressure gradient of 100 bar/km *(Bachu, 2000; Crandell et al., 2009, Qin and Beckingham 2021).* The upstream location is in the first internal column cells from left, the midstream is the central internal column cells, while the downstream location is the third column cells, furthest cells from the source of injection.

4.2.2.2. Brine chemistry, flow and boundary conditions

The initial formation brine chemistry (Table 4.2) was determined by simulating equilibrium between the XRD determined bulk mineralogy with 1 mol/kg NaCl brine in a closed batch system under 50◦ C for 10,000 years where the resulting initial pH, based on charge balance, was 8.34. This brine composition was used in subsequent flow through simulations for all three simulations.

In flow through simulations, CO_2 at a partial pressure of 100 bars was equilibrated with simulated formation brine in a 'ghost' boundary cell. Starting at a time of zero, the CO_2 saturated brine was flowed through the domain at a constant flowrate of 0.92 m/day *(Sheng et al., 2022)* and the evolution of major ions and mineral volume fractions tracked. The solubility of CO_2 in the formation brine was calculated in CrunchFlow using the Duan and Sun model based on the formation temperature and pressure (*Duan and Sun, 2003*). The corresponding conditions result in a CO_2 saturated brine with a pH of 2.995. Precipitation of potential secondary mineral phases was also considered where the potential precipitating phases were selected using the database sweep option in CrunchFlow. The tortuosity, permeability for mineral cells, and diffusion coefficient were 4.6 (*Hu et al., 2019*), 5.92154 x 10^{-20} m^2 *(Hu et al., 2019; Backeberg et al., 2017)* and 10^{-14} (*Du and Nojabaei, 2020; Hu et al., 2019*).

Simulations consider the flow of the CO_2 acidified brine through the domain starting from a time of 0 hours, reflecting field conditions and tracking the concentration of major ion species, mineral volume fractions, and porosity. The corresponding estimated temperature and pressure at the sample depth, 1066 m, is 50 ˚C and 100 bar, calculated based on a temperature gradient of 25 ◦C/km and surface temperature of 25 ˚C and pressure gradient of 100 bar/km *(Bachu, 2000; Crandell et al., 2009, Qin and Beckigham 2021).* The upstream location is in the first internal column cells from left, the midstream is the central internal column cells, while the downstream location is the third column cells, furthest cells from the source of injection.

The width of the fracture (0.2 millimeter) and clay-rich area (0.2 millimeter) were obtained from the image (Fig. 4.1a) and the permeability for the fracture cells was estimated by the cubic law for fracture permeability *(Lavrov, 2017; Ranjith and Viete, 2011; Steefel and Hu, 2022)*:

$$\text{Fracture permeability} = \frac{W_h^2}{12} \qquad (4.1)$$

where W_h, is the hydraulic aperture of the fracture, defined as the aperture of a smooth-walled conduit that has the same permeability as the real rough-walled fracture *(Brown 1987; Zimmerman et al. 1991).* Fracture permeability is a function of the average opening (aperture) of the fracture and the roughness of the fracture faces that create tortuous flow paths for the fluids *(Brown 1987; Muralidharan et al., 2004; Lavrov, A., 2017).*

In addition, in the simulations in which the porosity evolves due to geochemical reactions, the permeability is updated according to:

$$k = k_0 \frac{\phi^3}{\phi_0^3} \qquad (4.2)$$

where k is the permeability and k_0 and ϕ_0 are the initial permeability and porosity, respectively (*Steefel and Hu, 2022*).

Table 4.2. Simulated brine chemistry of the Mancos formation.

Ion	**Concentration (mol/kg fluid)**
CO_2 (aq)	1.14×10^{-05}
Ca^{++}	4.12×10^{-01}
Mg^{++}	1.71×10^{-02}
Fe^{++}	4.51×10^{-07}
K^{+}	3.25×10^{-04}
Al^{+++}	3.39×10^{-07}
SiO_2 (aq)	2.33×10^{-04}
pH	8.34
Na^{+}	1.41×10^{-01}
HS^{-}	7.90×10^{-07}
Cl^{-}	1.00
SO_4^{--}	1.13×10^{-07}

4.2.2.3. Mineral specific surface areas and reaction rates

Mineral specific surface areas measured using the BET method *(Brunauer et al., 1938)* in previous studies were collected from the literature and used here. For a given mineral phase, BET surface areas vary up to 4 orders of magnitude *(Black et al., 2015; Bourg et al., 2015)* depending on sample

source, sample condition, adsorption method used, etc. Here, the sensitivity of models to mineral surface areas (SA) was investigated using the high and low BET values for SA from the literature and the resulting impact on mineral reaction and porosity evolution compared.

Mineral reactions were simulated in CrunchFlow utilizing parallel rate laws to account for pH dependence and the effects of hydroxyl or electrolyte on the simulated reaction process *(Steefel and Molins 2016)*. The corresponding rate equation is given by:

$$r_s = -A\left(\sum_{a=1}^{N} K_a \left(\prod_{i=1}^{N_c+N_x} a_i^{p_{ia}}\right)\right)\left(1 - \left(\frac{Q_s}{K_s}\right)^M\right)^n \qquad (4.3)$$

where r_s is the reaction rate, A is the reactive surface area of a constituting mineral in the rock sample, K_a is the equilibrium dissolution rate constant for the 'a'th parallel reaction, N is number of parallel reactions, p_{ia} is an exponent that gives the dependence of a species i on the 'a'th parallel reaction, $\prod_{i=1}^{N_c+N_x} a_i^{p_{ia}}$ explains the degree of equilibrium effect of ions in solution, n and M are exponents which are experimentally determined to explain nonlinear dependence of the affinity term, K_s is the equilibrium constant, and Q_s is the ion activity product for the rock-water interaction. The rate constants which incorporate all geochemical dependencies relevant to the study were obtained from literature data and interpolated following Beckingham et al. (*2016*) at anticipated formation conditions post CO_2 injection corresponding to a temperature of 50 ◦C and pH of 2.995. The simulated pH of the system was determined via charge balance and the chemical formula of illite determined from SEM EDS analyses.

4.3. **Results and discussion**

Here, the results for simulations with heterogenous and homogenous mineral distributions are presented and further compared. Simulations consider the evolution of mineral volume fractions, ion concentrations, pH, and porosity. Time starts from negative values, indicating the state of the

system before CO_2 injection. At a time of 0 h, CO_2-saturated brine enters the system. In general, six different simulation sets were carried out including three different mineral volume fractions for two different BET SA sets. The simulated evolution of the system is consistent for both sides of the fracture and as such results are only shown for part of the simulation domain, the fracture cells and surrounding mineral cells from one side of the fracture (cells 1-9 in Figure 4.1).

4.3.1. Evolution of mineral volume fractions

Figure 4.3 shows the simulated spatial and temporal evolution of mineral volume fractions for the scenario with heterogenous mineralogy capturing the clay-rich region near the fracture surface. In this simulation, the initial mineral volume fraction information and their distribution around the fracture and in the matrix correspond to those in the processed SEM image showing the perpendicular to fracture region (Figure 4.1a). At a time of 0 hours, CO_2 saturated brine enters the system and leads to overall dissolution of the two carbonate phases - calcite and dolomite in addition to pyrite and kaolinite, while the other mineral phases remain relatively stable during the first 20 days (cells from 1 to 3 in Figure 4.3). The calcite volume fraction rapidly decreases from around 10% to 0.13% in almost all cells whereas dolomite has a slower dissolution rate, and its evolution varies across the domain. Pyrite and kaolinite dissolution initiate after depletion of calcite and dolomite. It should be noted, however, that pyrite dissolution requires oxygen. Initial oxygen concentrations in subsurface formations are anticipated to be low. However, oxygen may be introduced as an impurity during CO_2 injection and it is not well understood if this would be substantial enough to promote pyrite dissolution in these subsurface systems. In the simulation here, it is assumed sufficient oxygen exists to promote pyrite dissolution but additional efforts beyond the scope of this work are needed to thoroughly understand which, and when, conditions favor pyrite dissolution in subsurface systems.

In the up-stream cells (first column), calcite and dolomite rapidly dissolve and are close to depletion in less than a day, around 12 and 19 hours, respectively. Pyrite and kaolinite dissolution then begin and continue throughout the simulation domain. Quartz, K-feldspar, albite and illite remain stable throughout the simulation domain over the first few days. In the mid- and down-stream cells (i.e., second and third columns from left in Figure 4.3), up-stream calcite dissolution initially results in slight calcite precipitation that later dissolves. Complete dissolution of calcite in the mid and down-stream cells occurs at ~24 and 30 hours, respectively. At early time in mid- and down- stream cells, dolomite precipitates then begin dissolving following complete dissolution of calcite. The average dissolution rate of dolomite increases after complete dissolution of calcite in the system. In addition, kaolinite dissolves in these cells at the same rate as it is dissolving in the up-stream cells. Other minerals remain almost stable in the short term and only quartz precipitates with 0.1% mineral volume fraction. The results for cells 7 to 9, which are representative of the fracture, also shows a small amount of quartz precipitation.

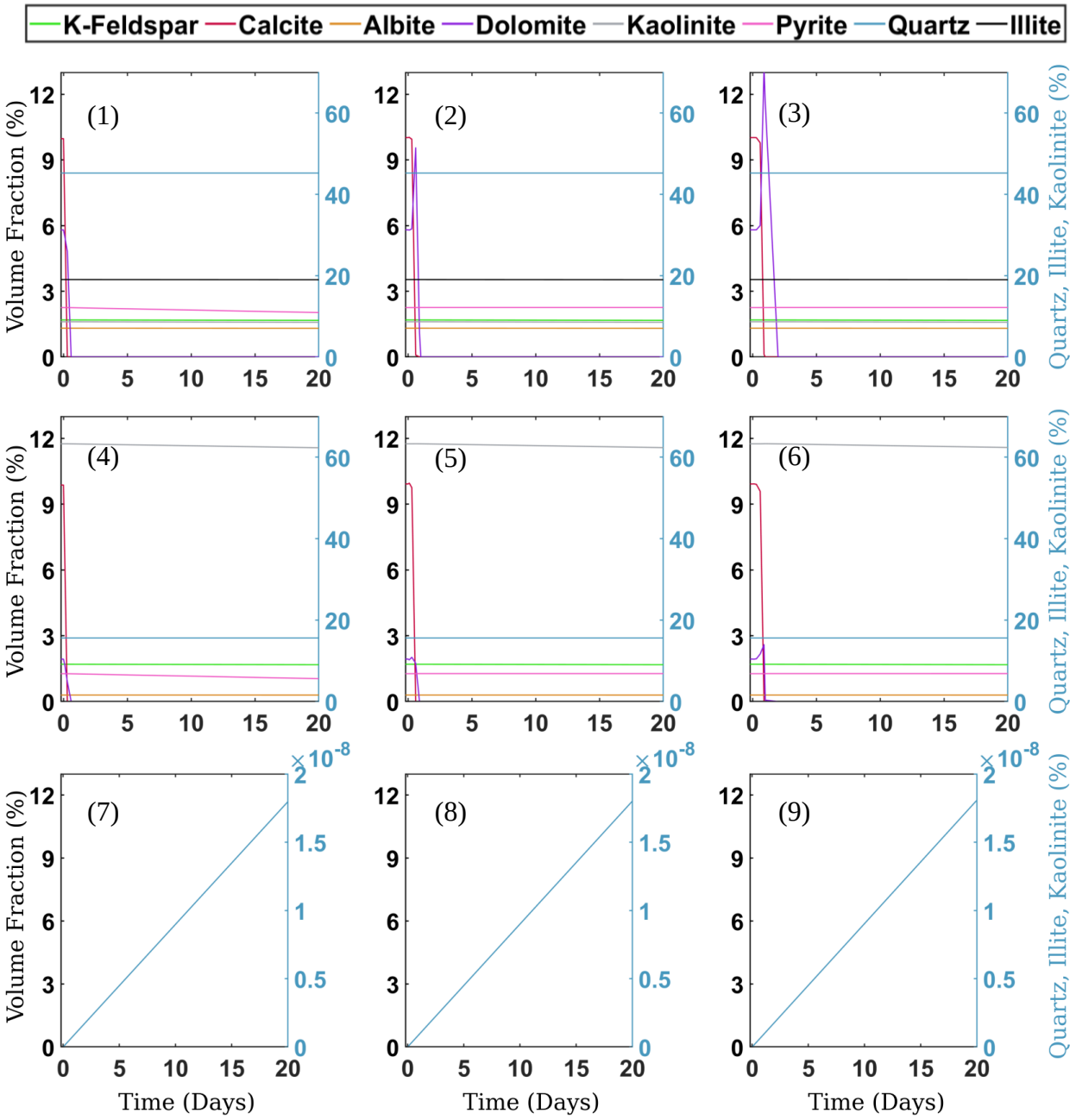

Figure 4.3. Simulated evolution of mineral volume fraction for the heterogenous mineralogy system defined using images perpendicular to the fracture over the first 20 days of simulation for cells one to nine. Cells 1 to 6 are representative of the fracture surface and 7 to 9 are representative of the fracture.

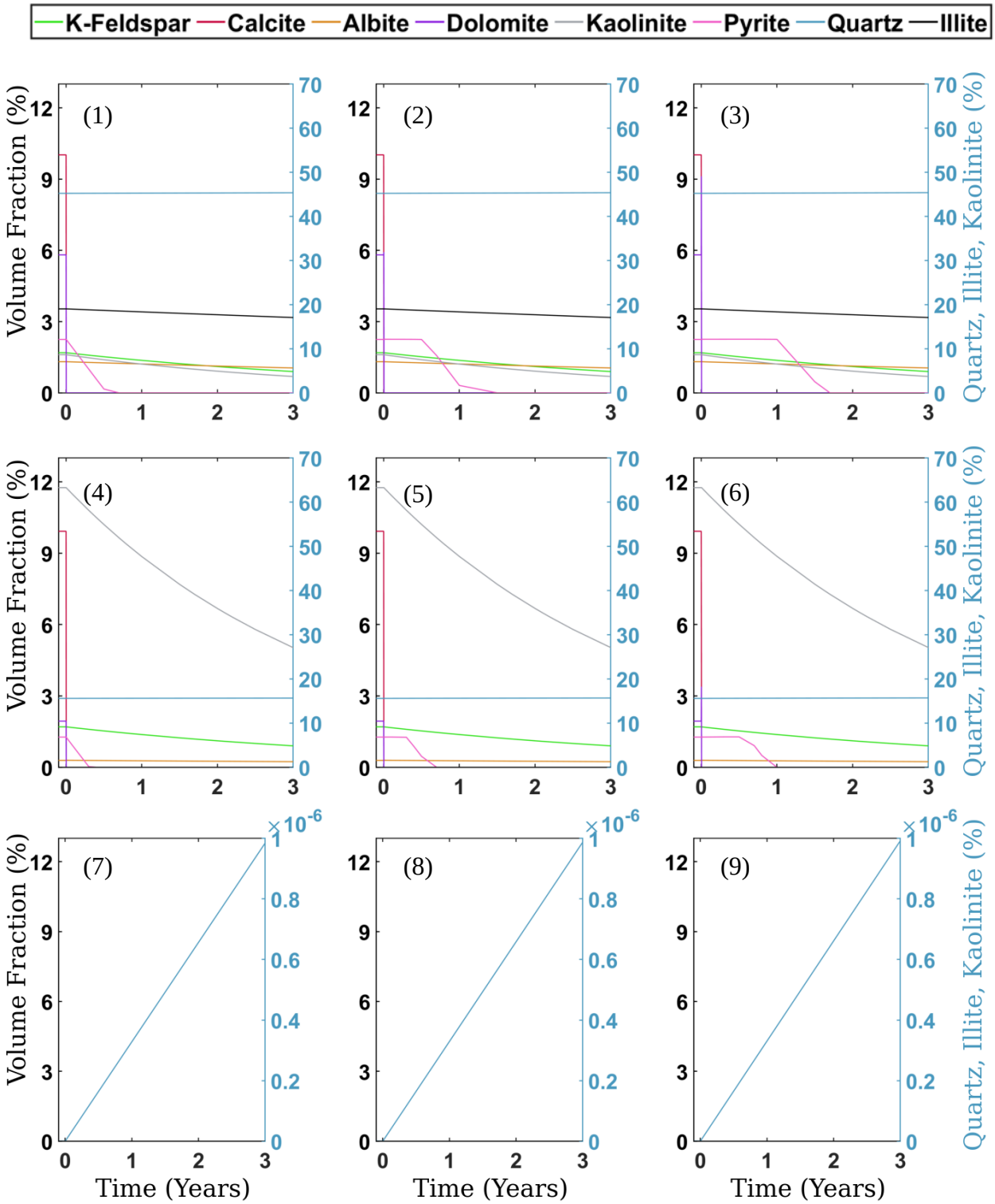

Figure 4.4. Simulated evolution of mineral volume fraction for systems with heterogenous mineralogy defined from the perpendicular images for the first 3 years of simulation for cells one to nine. Cells 1 to 6 reflect the fracture surface and 7 to 9 the fracture.

The simulated evolution of formation minerals over 3 years (Figure 4.4) follows a similar trend to that observed at short times for calcite and dolomite where they are depleted at the first days of simulation that is a half, 1.2, and 2 days for up-, mid- and down-stream cells, respectively. The average dissolution rate of kaolinite increases after almost complete dissolution of calcite in the system. Near the inlet (first column), pyrite initially remains stable then begins dissolving following almost complete dissolution of calcite in each cell. In mid- and down-stream cells, dissolution starts later due to some precipitation of pyrite coming from up-stream pyrite dissolution. Quartz is predicted to precipitate by 5% volume fraction over 3 years while K-feldspar is dissolved by 1% volume fraction in the same period where its dissolution is slightly higher in cells adjacent to the fracture (i.e., cells from 4 to 6). Dissolution of albite and kaolinite was also investigated. Conditions were observed favorable for dissolution of albite to small volume fractions (< 1 orders of magnitude of other minerals) whereas kaolinite dissolves up to 30% with smaller dissolution rates as time progresses. Changes in kaolinite are higher in cells adjacent to the fracture as is also true for K-feldspar.

Figures 4.5 to 4.8 show the temporal and special mineral volume evolution for systems with homogenous mineralogy from XRD and parallel image analyses. As the CO_2-saturated brine flows into both systems, dolomite and calcite rapidly dissolve in inlet mineral cells (first column), and the dolomite dissolution rate increases after calcite depletion. In mid- and down- stream cells, dolomite first precipitates and then dissolves which is similar to the heterogeneous scenario but with a lower amount of precipitation, to a volume fraction of 10% compared to 13% in the previous scenario. In general for all scenarios, the limitation of downstream calcite and dolomite dissolution, due to calcite dissolution in upstream at first days, results in non-uniform calcite volume fractions across the domain until all calcite in upstream cells is consumed. However, the

rate of consumption varies depending on the mineral distribution where simulations with uniform composition based on the XRD mineralogy have a higher calcite depletion rate followed by simulations accounting for the clay enriched near fracture region (perpendicular to fracture image Figure 4.2a) and those of the image observed matrix (parallel to fracture image, Figure 4.2c).

Unlike dolomite and calcite, K-feldspar dissolution in homogenous scenarios, occurs to a relatively uniform extent across the domain length as simulations progress, with a higher depletion rate for the XRD scenario followed by simulations considering heterogenous mineralogy and homogenous mineralogy informed by the image analysis. Pyrite and kaolinite also dissolve throughout the simulation domain in homogenous scenarios. While the dissolution rate of kaolinite is slower in these scenarios compared to the heterogenous system over the first 20 days, the dissolution rate of pyrite is higher here. Pyrite dissolution decreases from up-stream to down-stream and as time progress in both homogenous systems.

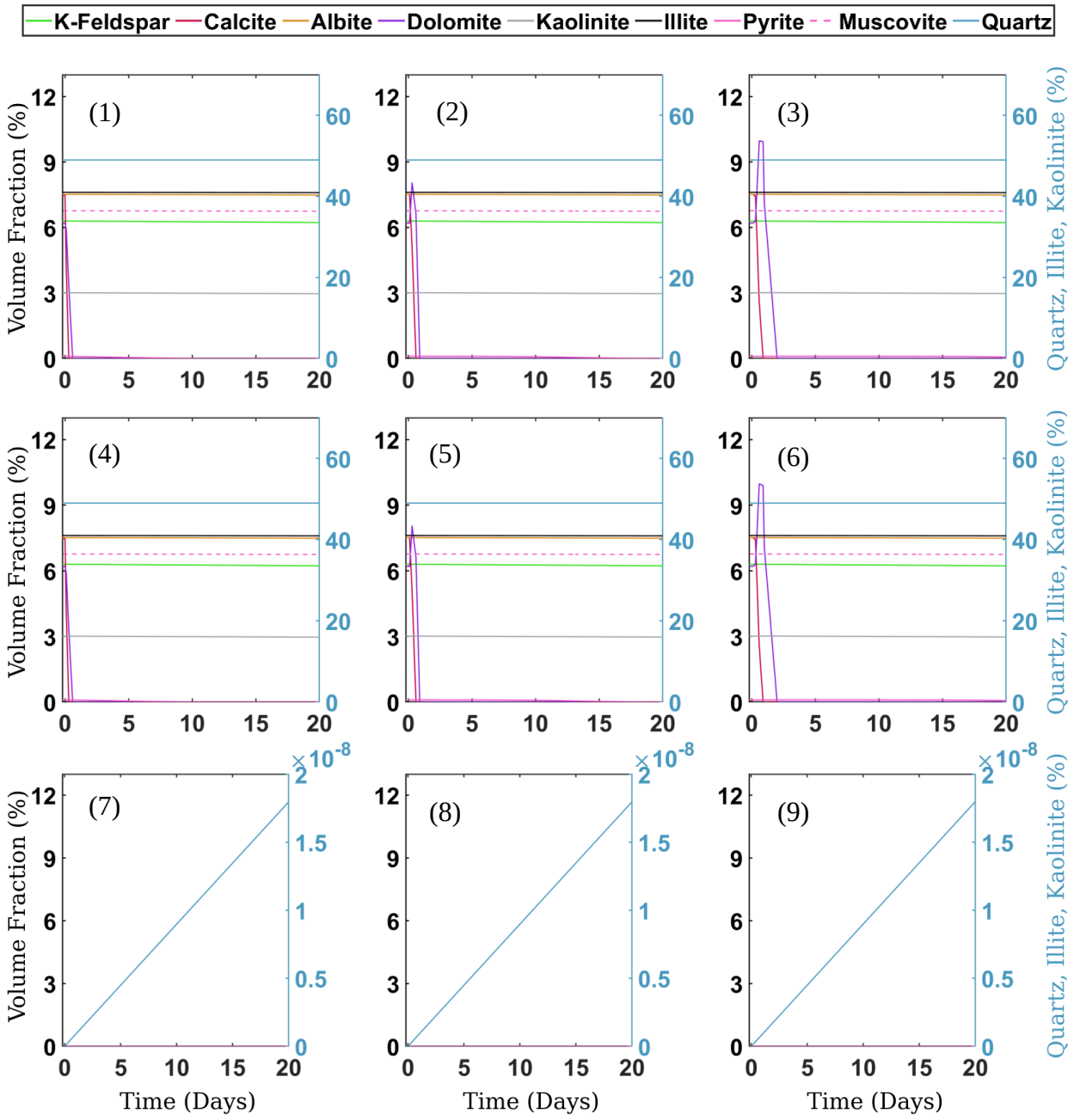

Figure 4.5. Simulated evolution of mineral volume fraction using XRD information depicting the first 20 days simulation for cells one to nine, Cells 1 to 6 are representative of the fracture surface and 7 to 9 are representative of the fracture.

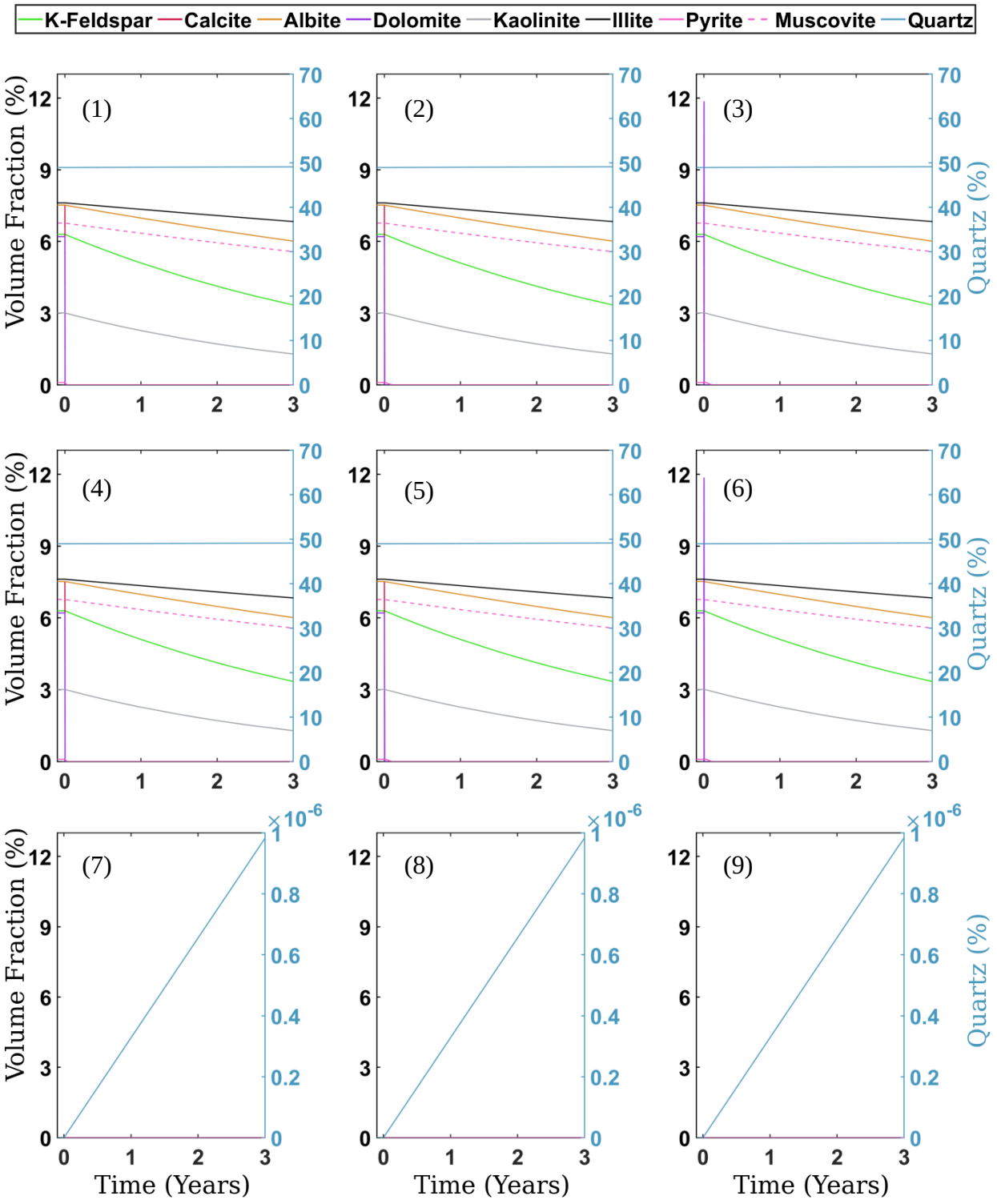

Figure 4.6. Simulated evolution of mineral volume fraction using XRD information depicting the first 3 years simulation for cells one to nine, where 1 to 6 are representativ of fracture surface and 7 to 9 are representative of fracture.

Considering long-term simulation for the homogeneous systems (Figure 4.6 and 4.8), calcite rapidly dissolves and is close to depletion around a half, 1 and 2 days in the up-stream, mid-stream and down-stream cells for the XRD scenario. These values are 13 hours, 1 day, and 2 days and 3 hours, respectively, for the simulations using the homogenous bulk mineralogy from the image parallel to the fracture. The kaolinite dissolution rate, in these scenarios, is also slower than in the heterogenous scenario. Here, the kaolinite volume fraction reduces by 1.5% and 5% compared to 30% reduction in the heterogenous scenario. The volume fraction of albite in simulations using the XRD mineralogy changed by 1.2% which is higher than the ones in both other scenarios. Muscovite is only present in the scenario using the XRD mineralogy and dissolves by 1.5% volume fraction. The volume fraction of K-feldspar decreases from 6% to 4% in the scenario using the XRD mineralogy which shows higher dissolution amount compared to the ones (by 1%) in the other scenarios. In both homogeneous mineralogy scenarios, quartz precipitates around 5%. In general, Quartz does not vary across the simulation domain in all 3 scenarios and precipitates uniformly throughout the simulation domain throughout the duration of the simulations, whereas, as explained, illite, K-feldspar, albite, and kaolinite dissolve and their dissolution vary across simulation domain and from one scenario to the other.

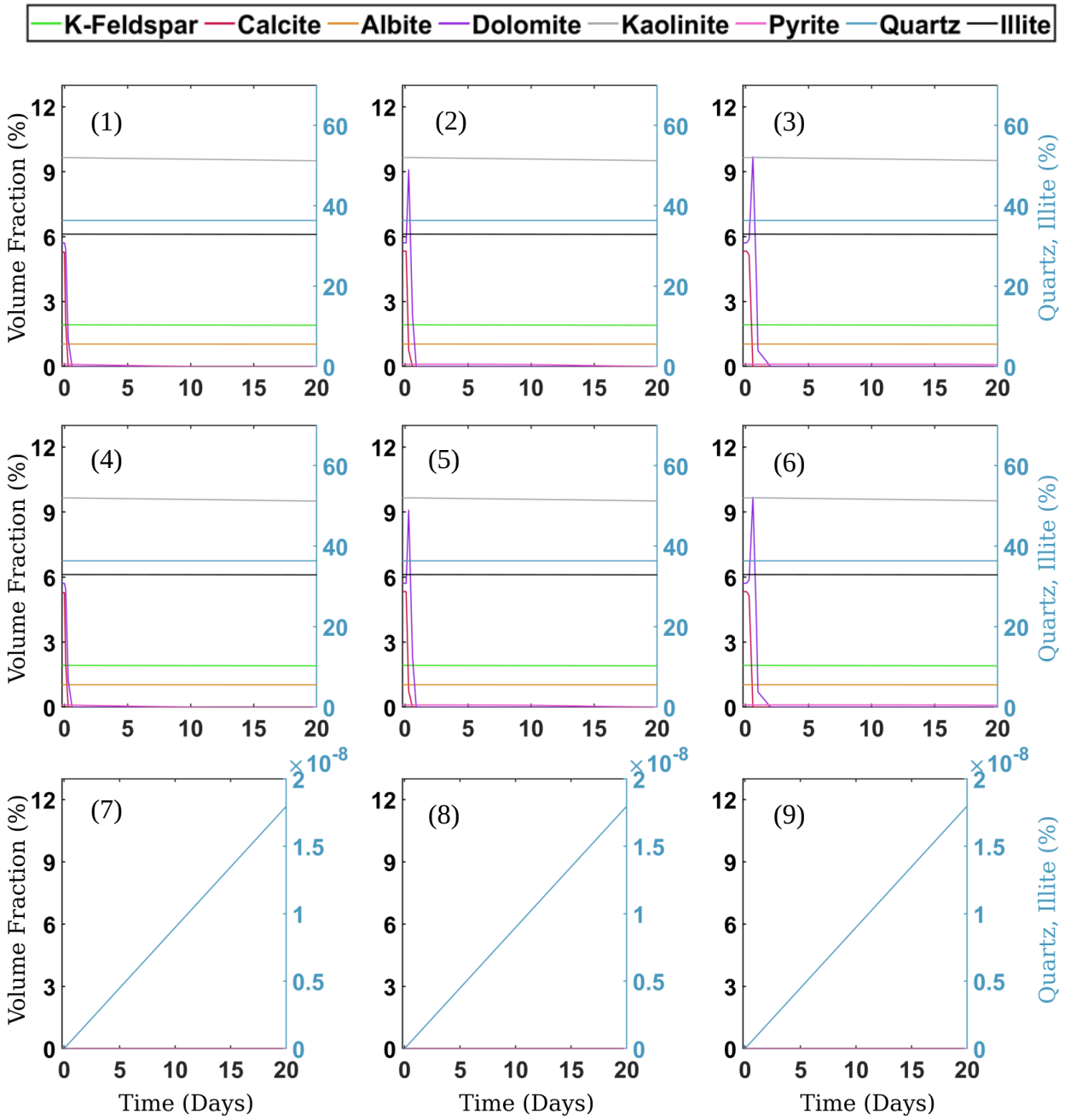

Figure 4.7. Simulated evolution of mineral volume fraction using parallel images to the fracture (Matrix) depicting the first 20 days simulation for cells one to nine, where 1 to 6 are representative of the fracture surface and 7 to 9 are representative of the fracture.

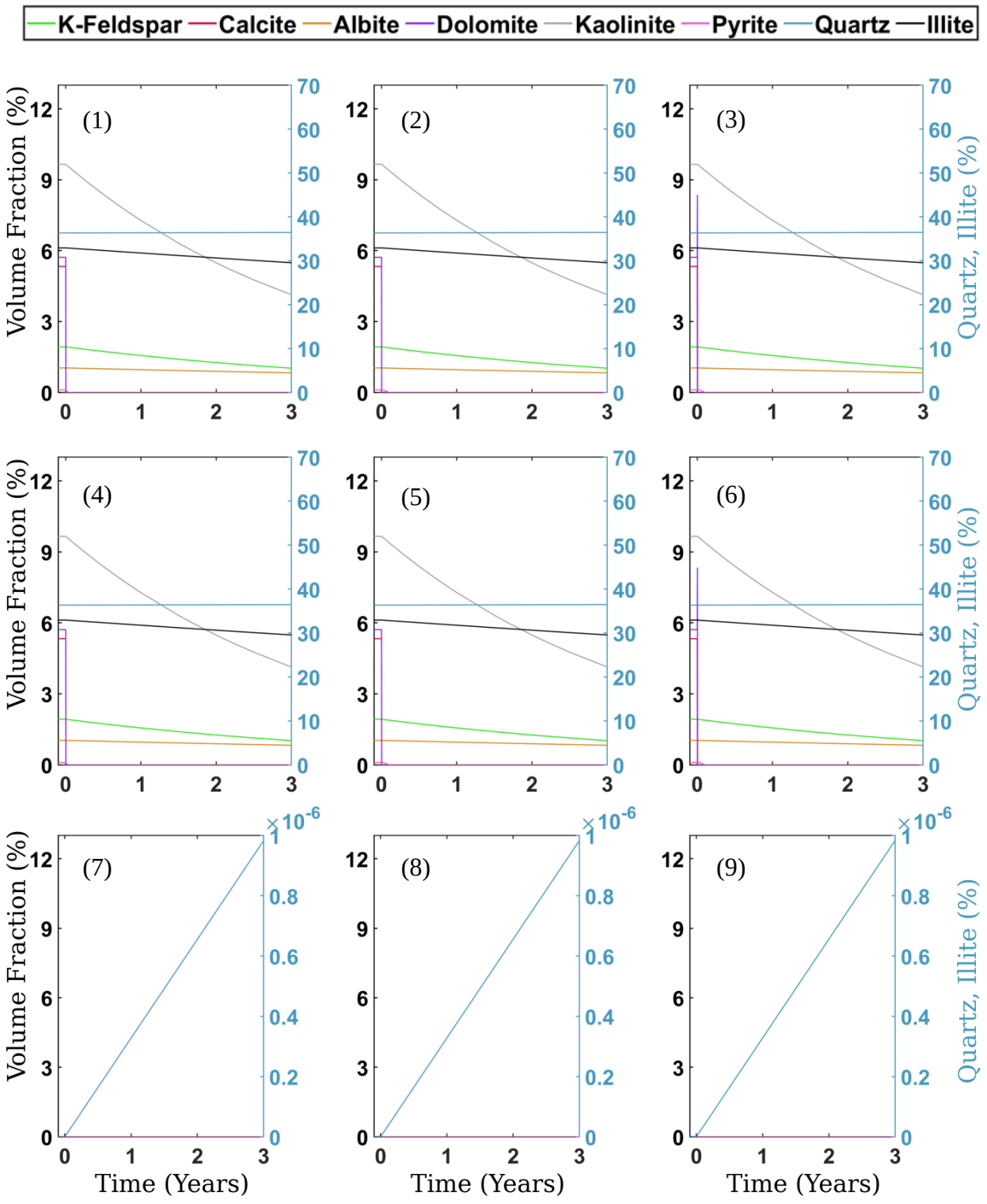

Figure 4.8. Simulated evolution of mineral volume fraction using parallel images to the fracture (Matrix) depicting the first 3 years simulation for cells one to nine, where 1 to 6 are representativ of fracture surface and 7 to 9 are representative of fracture.

4.3.2. Ion concentration and pH

The simulated evolution of major ion concentrations and pH in the CO_2-brine system for heterogenous system is shown in Figure 4.9 over 20 days and Figure 4.10 for the 3 years simulation duration. As the simulation starts, the introduction of acidified brine with a pH of 2.995 at 0 hour results in a decrease in the pH in the mineral cell from the initial pH of 8.4 and increases in the concentrations of calcium, magnesium and iron as calcite and dolomite and pyrite dissolve (Figure 4.9 and 4.10) in up-, mid- and down-stream cells. Calcite dissolution rapidly buffers the pH to 4.4, 4.5, 4.5 in the up-stream, mid-stream and down-stream locations, respectively. Decreasing calcite volume fraction in all cells is closely coupled with pH where the pH gradually drops to 2.995 as calcite is depleted and the extent of buffering is reduced, first in the upstream cell and later in the midstream and downstream locations. Magnesium ion concentration increases due to dolomite disillusion and decreases as time progress. It returns to background concentration as dolomite depletes by around 3 days from the beginning. The increase in iron, aluminum and sulfate concentrations after calcite depletion reflects dissolution of illite, pyrite and kaolinite where concentrations are lowest in the grid cell closet to the inlet and increase with distance from the up-stream or fracture cells. In the long-term, iron, aluminum and sulfate concentrations decrease after pyrite depletes that happens faster in the grid cell closet to the inlet and decreases with distance from the up-stream or fracture cells. No obvious change in aqueous silica or potassium concentrations occur within the simulation period.

The simulated major ion concentrations and pH evolution in the CO_2-brine system for homogenous systems (mineralogy was obtained from bulk XRD analysis and imaging of the matrix in a sample parallel to the fracture) are shown in Figure 4.11 to 4.14 over 20 days and 3 years, respectively. Similar calcium, magnesium and pH evolution patterns were observed in these

scenarios as explained for heterogeneous and the only different was the speed of evolutions that was faster in these two homogenous scenarios compared to the heterogenous one.

In long-term simulations, the rate of decrease in iron, aluminum and sulfate concentrations after calcite depletion was faster (less than a year for these scenarios) in comparison with the simulations considering heterogenous mineral distributions that was a half year for inlet and near fracture cells and one and half year for other cells. It may be due to variation in mineralogy and different amounts of mineral volume fractions of illite, pyrite, muscovite and kaolinite. In addition, concentrations are lowest in the grid cell closet to the inlet and increase with distance from the up-stream or fracture cells.

Overall, the differences in pH and major ion concentrations between different cells are mostly temporal and what was observed first in up-stream occurred in mid- and down-stream with about 2 days delay for calcium and magnesium that shows a good agreement with the results obtained from the volume fraction evolution section. Also, the concentrations are lowest in the grid cell closet to the inlet and increase with distance and time as minerals dissolve in CO_2 acidic brine from the up-stream or fracture cells till the completed depletion of mineral of interest and all patterns and orders follow the same ones mentioned for different scenarios in volume fraction evolution section.

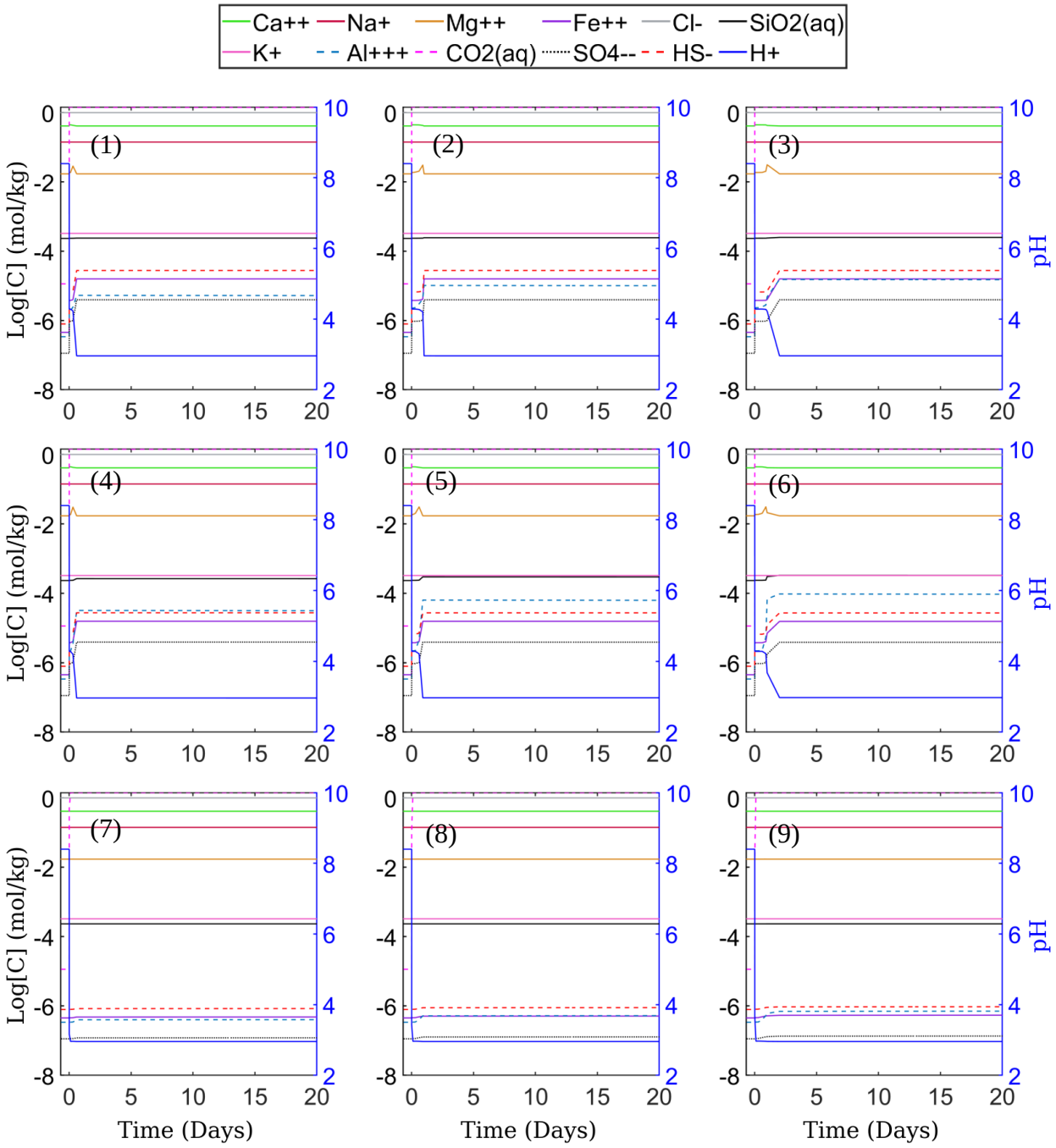

Figure 4.9. Simulated evolution of major ion concentrations and pH for fthe heterogenous mineralogy system defined using images perpendicular to the fracture over the first 20 days of simulation for cells one to nine. Cells 1 to 6 are representative of the fracture surface and 7 to 9 are representative of the fracture.

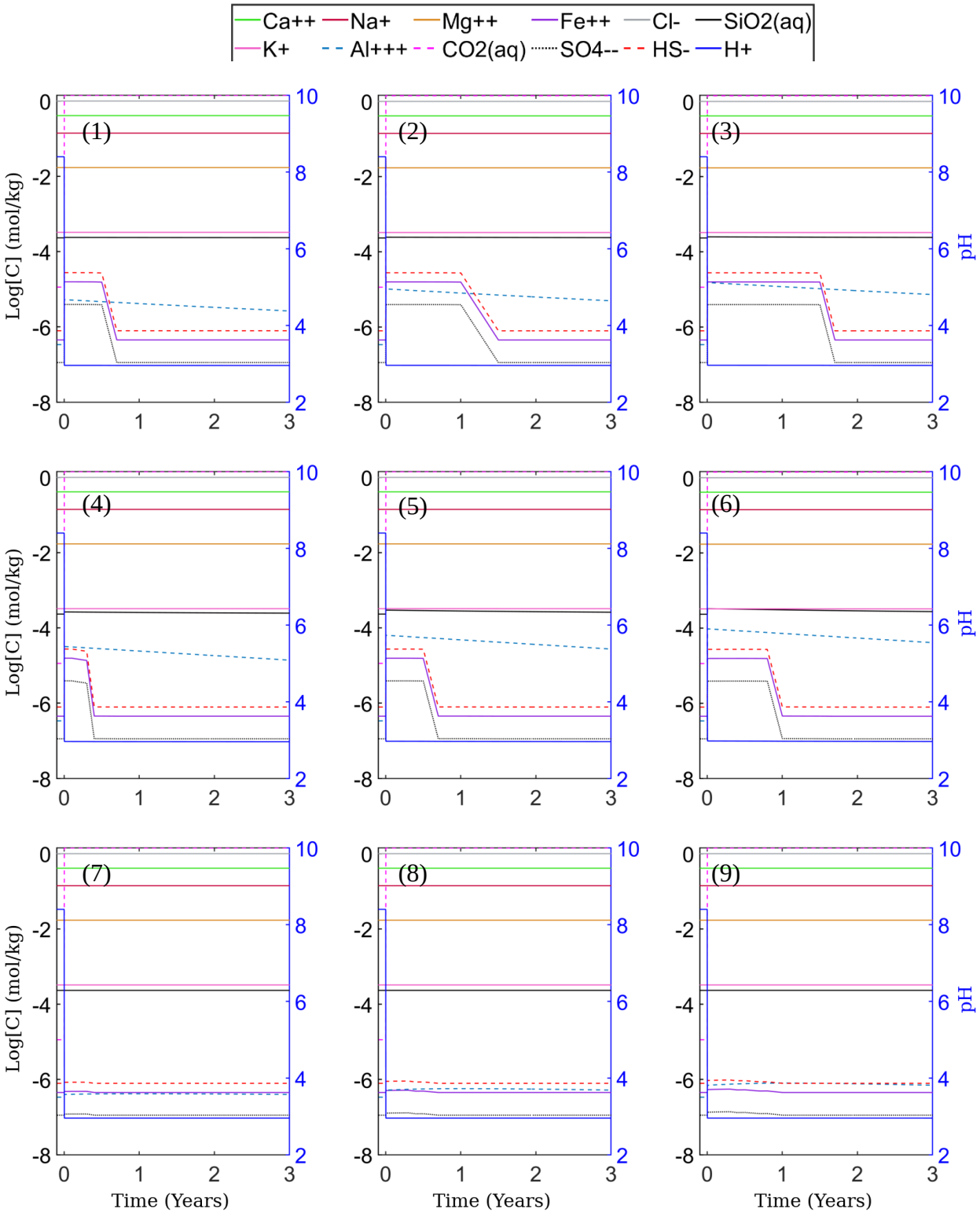

Figure 4.10. Simulated evolution of major ion concentrations and pH for the heterogenous mineralogy system defined using images perpendicular to the fracture depicting 3 years of simulation for cells one to nine. Cells 1 to 6 are representative of the fracture surface and 7 to 9 are representative of the fracture.

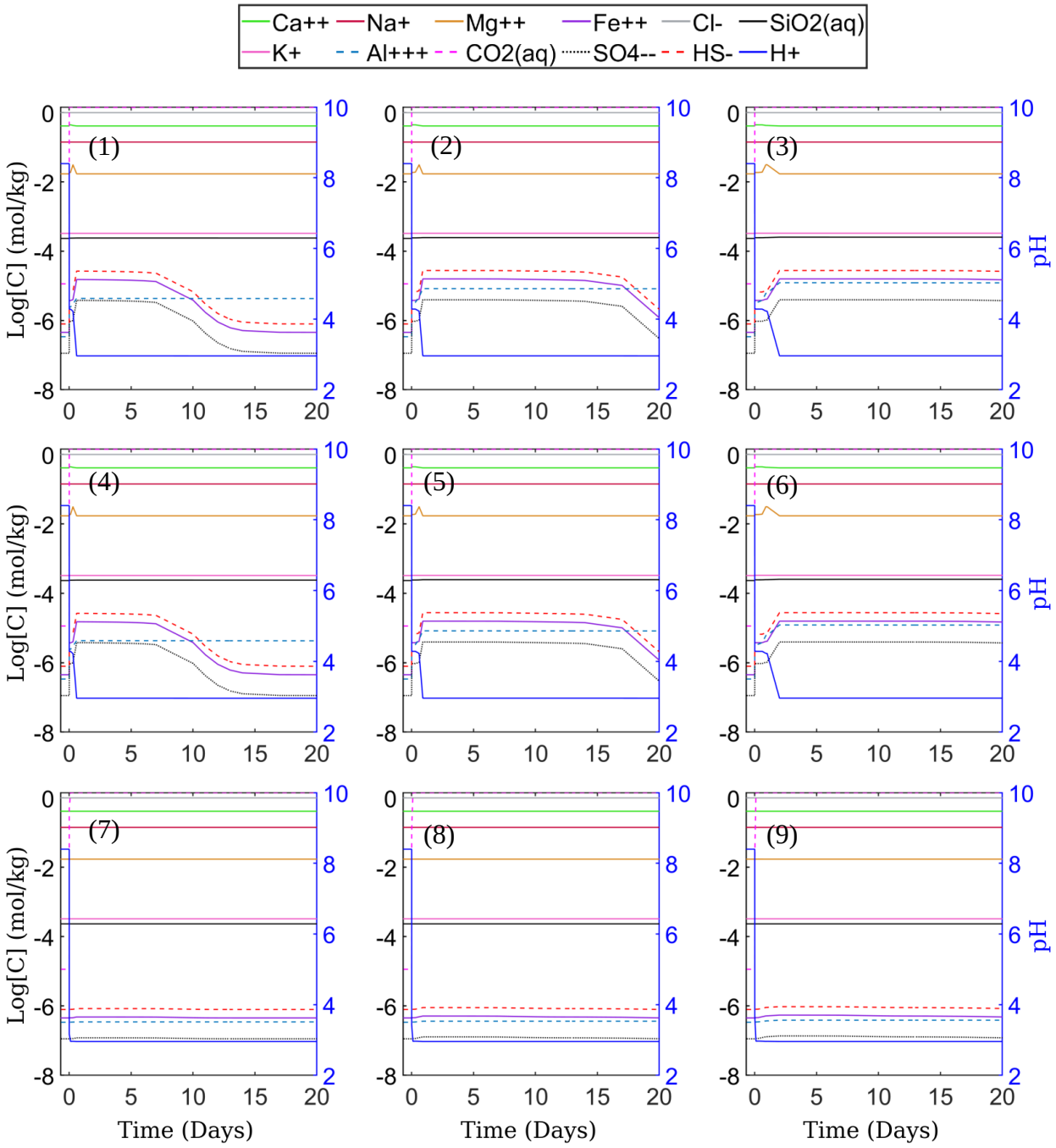

Figure 4.11. Simulated evolution of major ion concentrations and pH using XRD information depicting the first 20 days simulation for cells one to nine, Cells 1 to 6 are representative of the fracture surface and 7 to 9 are representative of the fracture.

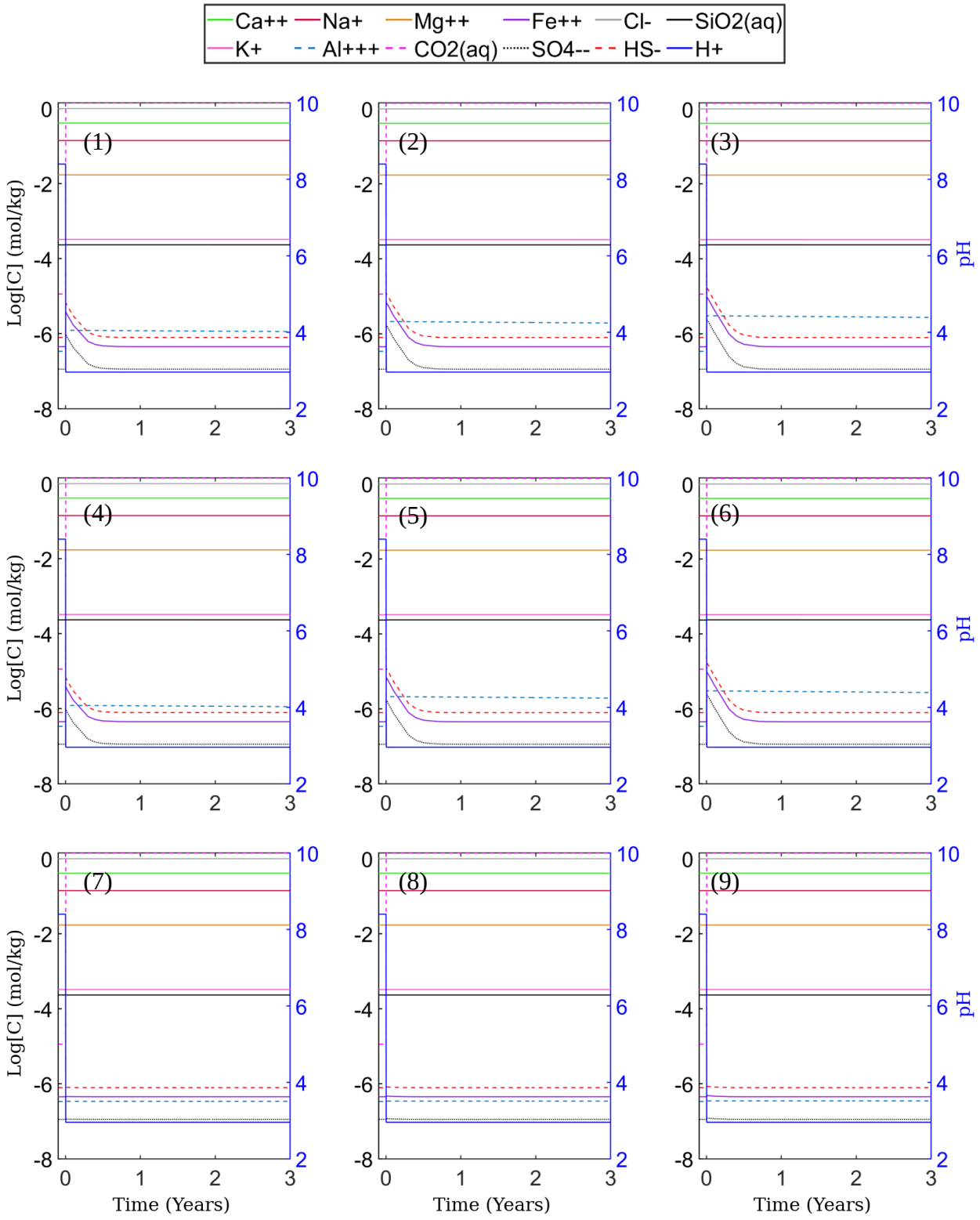

Figure 4.12. Simulated evolution of major ion concentrations and pH using XRD information depicting the 3 years simulation for cells one to nine, Cells 1 to 6 are representative of the fracture surface and 7 to 9 are representative of the fracture.

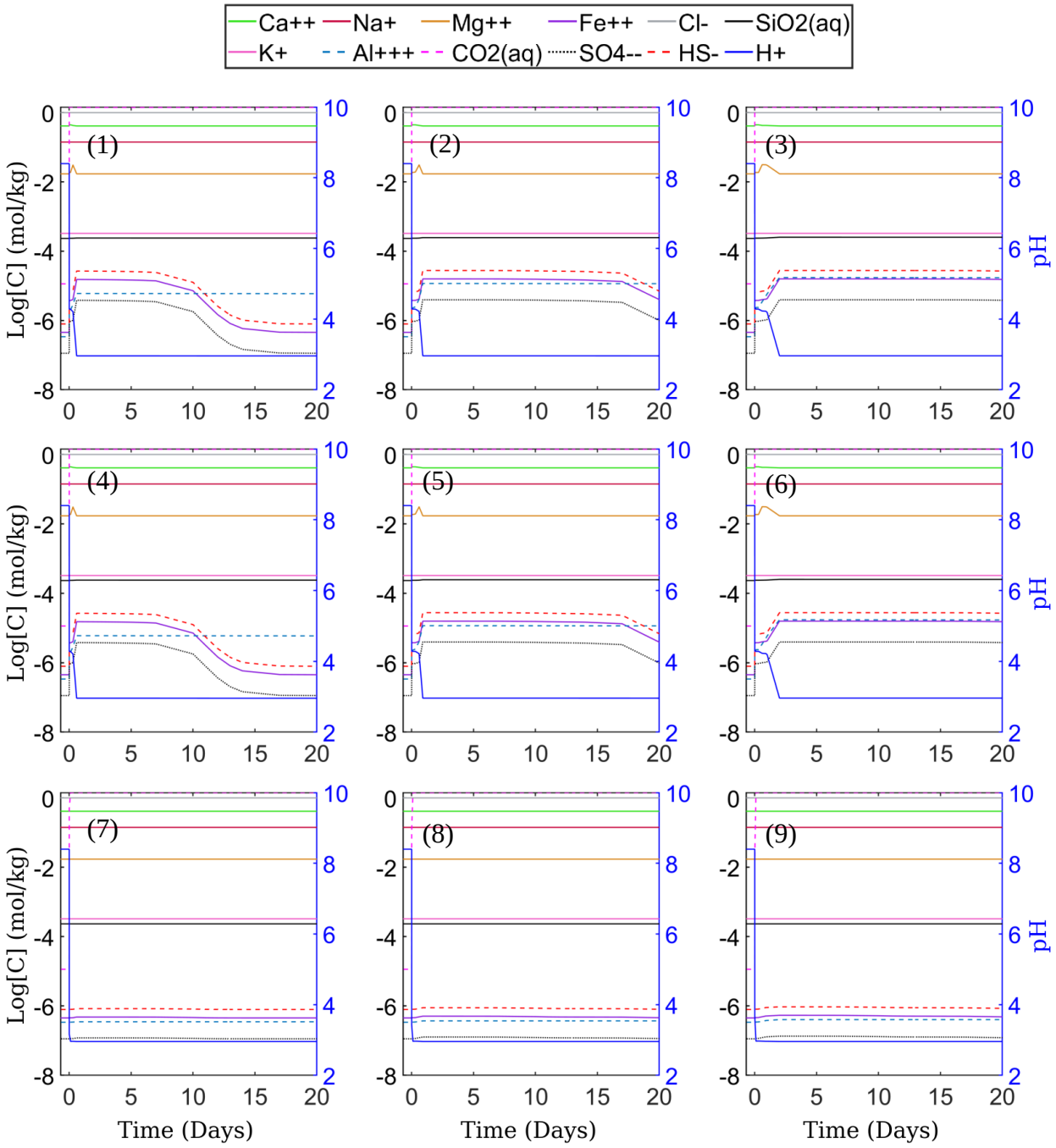

Figure 4.13. Simulated evolution of major ion concentrations and pH using parallel images to the fracture (Matrix) depicting the first 20 days simulation for cells one to nine, where 1 to 6 are representee of the fracture surface and 7 to 9 are representative of the fracture.

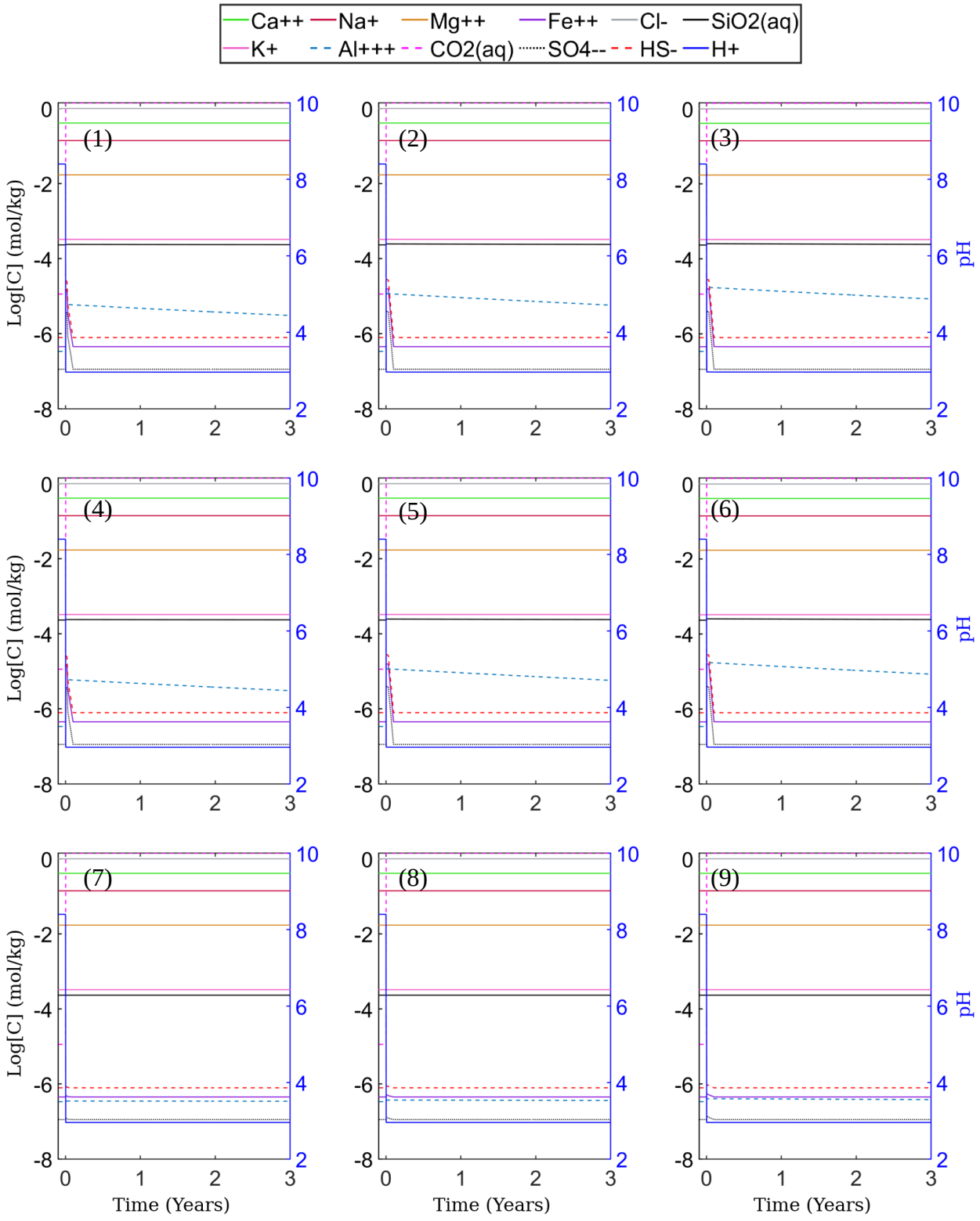

Figure 4.14. Simulated evolution of major ion concentrations and pH using parallel images to the fracture (Matrix) depicting 3 years simulation for cells one to nine, where 1 to 6 are representee of the fracture surface and 7 to 9 are representative of the fracture.

4.3.3. Porosity Evolution

The simulated evolution of porosity for the three different scenarios considering high and low BET SA over first 20 days and 3 years period are shown in Figure 4.15 and Figure 4.16, respectively. The porosity evolution serves to quantify the total effect of the mineral dissolution and precipitation reactions occurring in the sample following CO_2-brine injection. In Crunchflow software, the porosity (ϕ) is updated according to the evolving mineral volume fractions as a result of reactions, and at each time, it is defined as the subtraction of the total mineral volume fractions from the total volume (including voids) fractions.

As shown in Figure 4.15, in the up-stream cell furthest from the fracture, porosity rapidly increases with sharp slope throughout the simulation domain until ~1 day following CO_2-brine injection for all scenarios and continuous to gradually increase throughout the study duration. This is largely a result of dissolution of calcite and dolomite. After 20 days, the porosity in the up-steam cells have increased to 22%, 20% and 17.5%, from their initial value of 6% throughout the simulation for all scenarios with the largest increase in porosity for the heterogenous mineralogy system that reflects the clay-rich near fracture region and the smallest porosity increase for homogenous simulations using the bulk mineralogy from the imaging analysis of a parallel to fracture sample. This pattern and order are observed for mid- and down-stream cells furthest from the fracture (cells 1 to 3) due to similar mineralogy. However, the porosity increase is highest near the inlet and deceases away from the inlet largely due to variations in calcite dissolution.

For the first 20 days, there is little variation in porosity between the simulated results considering low or high BET SA for each scenario. The simulated evolution of porosity for cells closest to the fracture over 20 days shows porosity increases from 6% to 18.5%, 20% and 18% for the heterogeneous mineralogy, homogenous bulk XRD mineralogy, and homogenous bulk imaging mineralogy, respectively. The change of the order may be because of slower transport and

reaction in the clay-rich region in the heterogenous scenario compared to the homogenous scenario using the bulk XRD mineralogy.

Over longer time periods (Figure 4.16), porosity continues to increase with the expectation that the locations closest to the inlet and fracture have higher porosity. This is because downstream reactions are limited by elevated ion concentrations resulting from upstream dissolution. This also explains the lower porosity and slower depletion rates at the mid- and down-stream cells for heterogenous mineralogy scenario's compared to the homogenous scenarios XRD and matrix. The overall simulated change in porosity is different for each scenario, highlighting the importance of considering the clay-rich area next to the fracture that may cause up to a 20% difference in simulated porosity evolution. In addition, differences in the simulated porosity based on the selected surface area values are evident where higher surface area values result in larger simulated increases in porosity and permeability in these areas (based on equation 4.2). Extreme increases in porosity and permeability result (equation 4.2) in simulations using the high BET SA values for simulations that reflect the clay rich region near the fracture. It should be noted that with such large increases, the fracture may no longer be stable and may collapse due to confining pressure. This, however, cannot be accounted for in the simulation approach considered here. Overall, simulations showed fracture apertures slightly decrease due to a small amount of quartz precipitation throughout the simulation as the precipitation will increase the total mineral volume fraction in these cells that also slightly reduce the permeability in these areas.

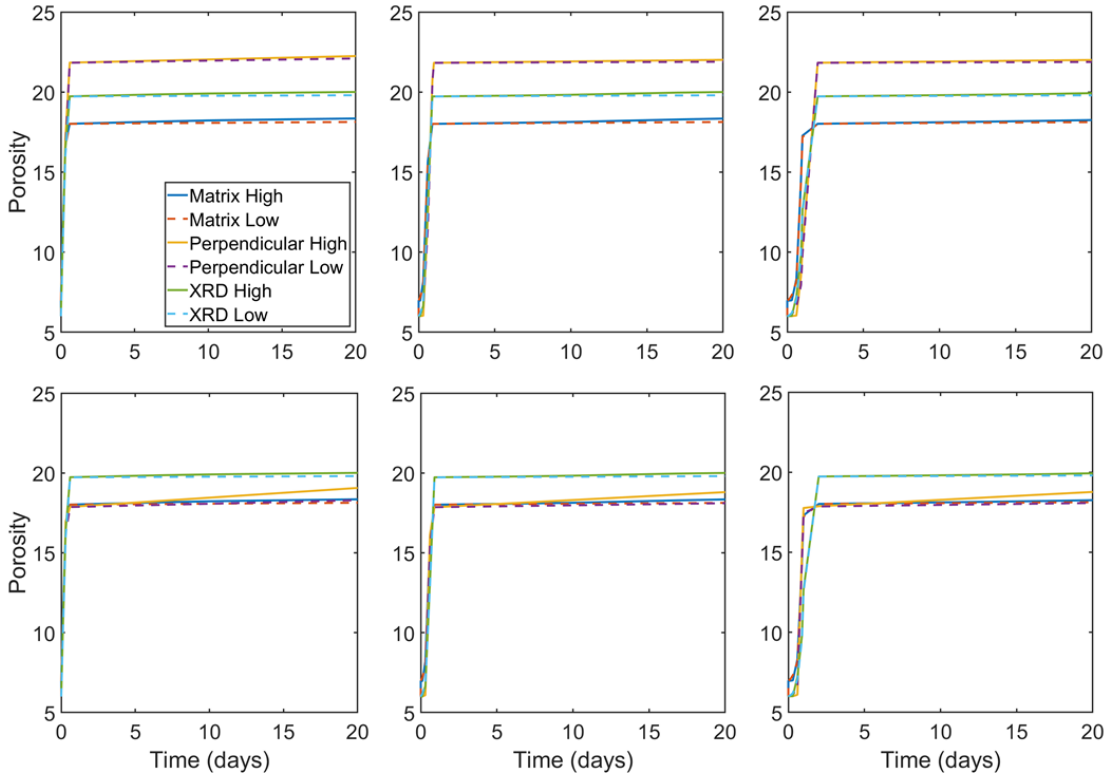

Figure 4.15. Simulated porosity (%) evolution over first 20 days.

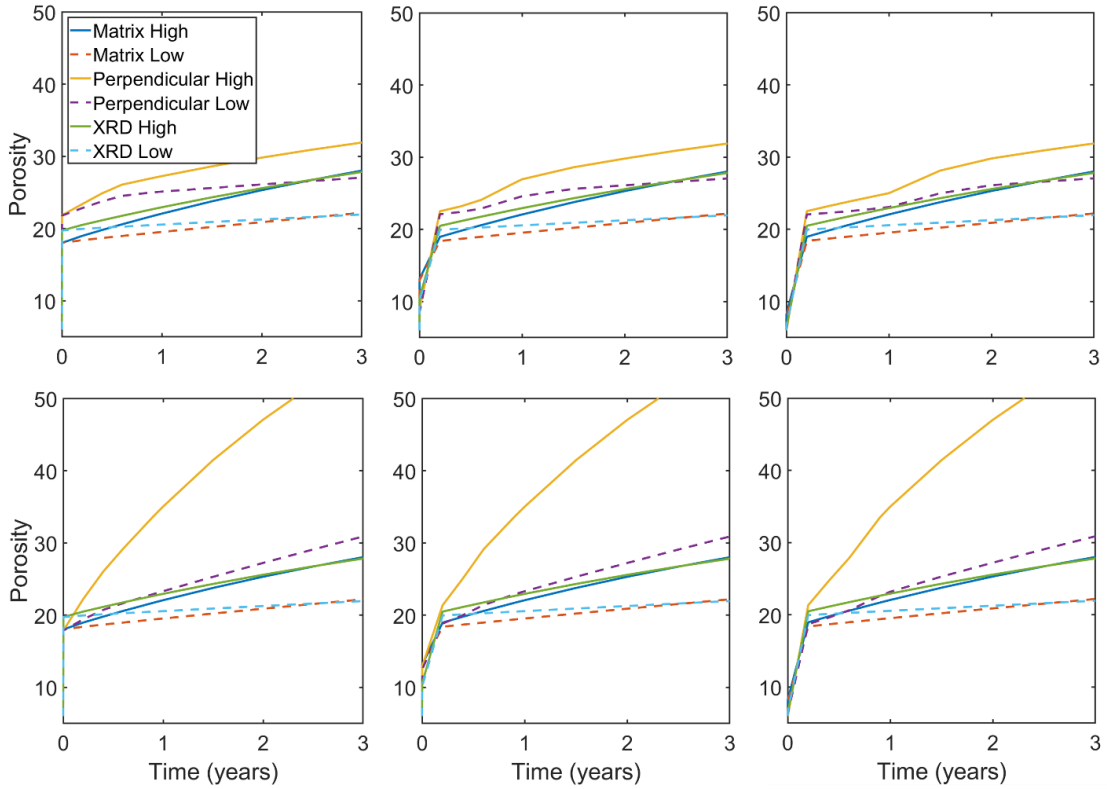

Figure 4.16. Simulated porosity (%) evolution over 3 years.

4.4. **Conclusion**

This work aims to understand the impact of variations in minerology of the fracture surface and surrounding matrix on simulated mineral reactions and reaction rates between minerals and CO_2 saturated brine. We quantitatively assess and compare the simulated porosity, mineral, and ion concentration evolutions near fracture surfaces in the context of geologic CO_2 storage, for various heterogenous and homogenous mineral distributions measured from image analyses of SEM-BSE images and XRD analysis. Simulations consider reactions with CO_2 acidified brine at two timescales, a short (days) time scale and a long (years) time scale.

Overall, temporal and spatial variations in the simulation results are evident where cells close to either the inlet or fracture have a higher extent of reaction compared to the other cells. The highest change in the simulated porosity, mineral composition and ion concentration happened in the upstream cells closest to the fracture surface in all scenarios. Similar patterns in calcite and dolomite dissolution are evident in each simulation but over different time scales. In addition, for all scenarios, dissolution of some minerals such as calcite and dolomite in inlet cells results in slower reactions and changed in mineralogy in mid- and down-stream cells, which is also intensified due to the high dependency of reactions on diffusion. In all scenarios, the high reaction rate of calcite results in rapid depletion of calcite upstream that prevents downstream calcite and dolomite dissolution until almost complete calcite consumption in upstream cells.

The rate of mineral dissolution varies depending on the mineral distribution where simulations with uniform composition based on the XRD mineralogy have a higher calcite depletion rate followed by simulations accounting for the clay enriched near fracture region and those using the homogenous mineralogy observed in the image. K-feldspar dissolution also has a higher depletion rate for the XRD scenario followed by heterogenous and homogenous image

informed scenarios. Large variations in kaolinite, albite, and illite dissolution among scenarios were observed with the largest reduction in illite and kaolinite volume fractions in the heterogenous scenario. Slight uniform quartz precipitation throughout the simulation domain and duration is noted for all scenarios.

Considering the impacts of surface area on simulation results between scenarios, variations in mineralogy and porosity were observed. For short times, dissolving calcite and dolomite control the porosity evolution such that fasted increases in porosity are evident for heterogenous simulations that reflect the clay rich near fracture region followed by homogenous simulations using the XRD mineralogy in cells furthest from the fracture. In cells closest to the fracture, the largest increase in porosity was for homogenous simulations using XERD mineralogy followed by the heterogenous mineralogy simulations. Variations in SA for given simulations had little impact on the simulated evolution of porosity.

For long time simulations, mineral dissolution and porosity increase was faster for simulations using the heterogenous mineralogy followed by the homogenous simulations using XRD mineralogy. In contrast to the short-term simulations, variations in porosity have a noted impacted on the simulated evolution of porosity. Higher surface areas result in increased reaction rates and increased porosity.

Overall, simulations showed fracture apertures slightly decrease due to a small amount of quartz precipitation throughout the simulation as the precipitation will increase the total mineral volume fraction in these cells. It is noted that the porosity is defined as the subtraction of the total mineral volume fractions from the total volume fractions. In addition, different patterns of dissolution are evident for different minerals such as illite and K-feldspar for the different scenarios. As such, the evolution of matrix porosity is different in each scenario. This may impact

the minerals that are accessible to reactive fluids, potentially exposing new surfaces. Simulations that do not consider heterogeneity in mineral distribution may result in simulations unable to accurately reflect the actual mineral reactions occurred, especially for cells adjacent to the fracture. This is critical in assessing if fractures will self-seal or be enhanced due to reactions. Larger reaction extents near the fracture surface and corresponding increases in porosity may promote fracture sealing by compressive stress while systems with less reactive near-fracture regions may retain fracture permeability. The results could improve our ability to predict reactive fracture evolution and understand its implications for subsurface CO_2 sequestration and oil recovery.

4.5. **Acknowledgements**

Acknowledgment is made to the Donors of the American Chemical Society Petroleum Research Fund and the National Science Foundation (Grant No: 1847243) for support of this research.

4.6. **Reference**

- Atchley, A. L., Navarre-Sitchler, A. K., & Maxwell, R. M. (2014). The effects of physical and geochemical heterogeneities on hydro-geochemical transport and effective reaction rates. Journal of contaminant hydrology, 165, 53-64.
- Asadi, P., & Beckingham, L. E. (2021). Integrating Machine/Deep Learning Methods and Filtering Techniques for Reliable Mineral Phase Segmentation of 3D X-ray Computed Tomography Images. Energies, 14(15), 4595.
- Backeberg, N. R., Iacoviello, F., Rittner, M., Mitchell, T. M., Jones, A. P., Day, R., ... & Striolo, A. (2017). Quantifying the anisotropy and tortuosity of permeable pathways in clay-rich mudstones using models based on X-ray tomography. *Scientific reports*, *7*(1), 1-12.

- Beckingham, L. E., Steefel, C. I., Swift, A. M., Voltolini, M., Yang, L., Anovitz, L. M., ... & Xue, Z. (2017). Evaluation of accessible mineral surface areas for improved prediction of mineral reaction rates in porous media. Geochimica et Cosmochimica Acta, 205, 31-49.
- Bevan, J., & Savage, D. (1989). The effect of organic acids on the dissolution of K-feldspar under conditions relevant to burial diagenesis. Mineralogical Magazine, 53(372), 415-425.
- Brady, P. V., & Walther, J. V. (1990). Kinetics of quartz dissolution at low temperatures. Chemical geology, 82, 253-264.
- Brady, P. V., & Walther, J. V. (1989). Controls on silicate dissolution rates in neutral and basic pH solutions at 25 C. Geochimica et Cosmochimica acta, 53(11), 2823-2830.
- Bourg, I. C. (2015). Sealing Shales versus Brittle Shales: A Sharp Threshold in the Material Properties and Energy Technology Uses of Fine-Grained Sedimentary Rocks. Environmental Science and Technology Letters, 2(10). https://doi.org/10.1021/acs.estlett.5b00233
- Bourg, I. C. (2015). Sealing Shales versus Brittle Shales: A Sharp Threshold in the Material Properties and Energy Technology Uses of Fine-Grained Sedimentary Rocks. Environmental Science and Technology Letters, 2(10).
- Brunhoeber, O. M., Anovitz, L. M., Asadi, P., & Beckingham, L. E. (2021). Role of mineralogy in controlling fracture formation. ACS Earth and Space Chemistry, 5(11), 3104-3114.
- Brunhoeber, O. M., Anovitz, L. M., Asadi, P., & Beckingham, L. E. (2021). Role of mineralogy in controlling fracture formation. ACS Earth and Space Chemistry, 5(11), 3104-3114.

- Busch, B., Okamoto, A., Garbev, K., & Hilgers, C. (2021). Experimental fracture sealing in reservoir sandstones and its relation to rock texture. Journal of Structural Geology, 153, 104447.
- Carroll, S. A., & Walther, J. V. (1990). Kaolinite dissolution at 25 degrees, 60 degrees, and 80 degrees C. American Journal of Science, 290(7), 797-810.
- Chen, Y., & Brantley, S. L. (1997). Temperature-and pH-dependence of albite dissolution rate at acid pH. Chemical Geology, 135(3-4), 275-290.
- Deng, H., Ellis, B. R., Peters, C. A., Fitts, J. P., Crandall, D., & Bromhal, G. S. (2013). Modifications of carbonate fracture hydrodynamic properties by CO2-acidified brine flow. *Energy & Fuels*, *27*(8), 4221-4231.
- Ding, W., Li, C., Li, C., Xu, C., Jiu, K., Zeng, W., & Wu, L. (2012). Fracture development in shale and its relationship to gas accumulation. Geoscience Frontiers. https://doi.org/10.1016/j.gsf.2011.10.001.
- Detwiler, R. L., & Morris, J. P. (2018). Fracture Initiation, Propagation, and Permeability Evolution. https://doi.org/10.1002/9781119118657.ch5.
- Du, F., & Nojabaei, B. (2020). Estimating diffusion coefficients of shale oil, gas, and condensate with nano-confinement effect. Journal of Petroleum Science and Engineering, 193, 107362.
- Ellis, B., Peters, C., Fitts, J., Bromhal, G., McIntyre, D., Warzinski, R., & Rosenbaum, E. (2011). Deterioration of a fractured carbonate caprock exposed to CO2-acidified brine flow. *Greenhouse Gases: Science and Technology*, *1*(3), 248-260.
- Ellis, B. R., & Peters, C. A. (2016). 3D Mapping of calcite and a demonstration of its relevance to permeability evolution in reactive fractures. *Advances in water resources*, *95*, 246-253.

- Ganor, J., Mogollón, J. L., & Lasaga, A. C. (1995). The effect of pH on kaolinite dissolution rates and on activation energy. Geochimica et Cosmochimica Acta, 59(6), 1037-1052.
- Gale, J. F. W., Laubach, S. E., Olson, J. E., Eichhubl, P., & Fall, A. (2017). Natural fractures in shale: A review and new observations. AAPG Bulletin. https://doi.org/10.1306/08121413151
- Gu, X., & Evans, L. J. (2007). Modelling the adsorption of Cd (II), Cu (II), Ni (II), Pb (II), and Zn (II) onto fithian illite. Journal of colloid and interface science, 307(2), 317-325.
- Guo, L., Jiang, Z. xing, & Guo, F. (2015). Mineralogy and fracture development characteristics of marine shale-gas reservoirs: A case study of Lower Silurian strata in southeastern margin of Sichuan Basin, China. Journal of Central South University. https://doi.org/10.1007/s11771-015-2704-6.
- Hu, Q., Kalteyer, R., Wang, J., & El-Sobky, H. F. (2019). Nanopetrophysical characterization of the Mancos shale formation in the san juan basin of northwestern New Mexico, USA. Interpretation, 7(4), SJ45-SJ65.
- Iloejesi, C. O., & Beckingham, L. E. (2021a). Assessment of geochemical limitations to utilizing CO_2 as a cushion gas in compressed energy storage systems. Environmental engineering science, 38(3), 115-126.
- Iloejesi, C. O., & Beckingham, L. E. (2021b). Influence of storage period on the geochemical evolution of a compressed energy storage system. Frontiers in Water, 100.
- Iloejesi, C. O., & Beckingham, L. E. (2021). Influence of storage period on the geochemical evolution of a compressed energy storage system. Frontiers in Water, 3 ,100-113.

- Jew, A. D., Druhan, J. L., Ihme, M., Kovscek, A. R., Battiato, I., Kaszuba, J. P., ... & Brown Jr, G. E. (2022). Chemical and Reactive Transport Processes Associated with Hydraulic Fracturing of Unconventional Oil/Gas Shales. Chemical reviews, 122(9), 9198-9263.
- Khan, H. J., Spielman-Sun, E., Jew, A. D., Bargar, J., Kovscek, A., & Druhan, J. L. (2021). A critical review of the physicochemical impacts of water chemistry on shale in hydraulic fracturing systems. Environmental science & technology, 55(3), 1377-1394.
- Kumar, N., Sampaio, M. A., Ojha, K., Hoteit, H., & Mandal, A. (2022). Fundamental aspects, mechanisms and emerging possibilities of CO_2 miscible flooding in enhanced oil recovery: A review. Fuel, 330, 125633.
- Kuva, J., Siitari-Kauppi, M., Lindberg, A., Aaltonen, I., Turpeinen, T., Myllys, M., & Timonen, J. (2012). Microstructure, porosity and mineralogy around fractures in Olkiluoto bedrock. Engineering Geology, 139–140.
- Lavrov, A. (2017). Fracture permeability under normal stress: a fully computational approach. Journal of Petroleum Exploration and Production Technology, 7(1), 181-194.
- Li, X., Zhu, H., Zhang, K., Li, Z., Yu, Y., Feng, X., & Wang, Z. (2021). Pore characteristics and pore structure deformation evolution of ductile deformed shales in the Wufeng-Longmaxi Formation, southern China. Marine and Petroleum Geology, 127, 104992.
- Li, L., Peters, C. A., & Celia, M. A. (2007). Effects of mineral spatial distribution on reaction rates in porous media. Water resources research, 43(1).
- Li, L., Steefel, C. I., & Yang, L. (2008). Scale dependence of mineral dissolution rates within single pores and fractures. Geochimica et Cosmochimica Acta, 72(2), 360-377.
- Na, S. H., Sun, W. C., Ingraham, M. D., & Yoon, H. (2017). Effects of spatial heterogeneity and material anisotropy on the fracture pattern and macroscopic effective toughness of Mancos

Shale in Brazilian tests. Journal of Geophysical Research: Solid Earth. https://doi.org/10.1002/2016JB013374.

- Navarre-Sitchler, A., Brantley, S. L., & Rother, G. (2015). How porosity increases during incipient weathering of crystalline silicate rocks. Reviews in Mineralogy and Geochemistry, 80(1), 331-354.
- Palandri, J. L., & Kharaka, Y. K. (2004). A compilation of rate parameters of water-mineral interaction kinetics for application to geochemical modeling. Geological Survey Menlo Park CA.
- Qin, F., & Beckingham, L. E. (2019). Impact of image resolution on quantification of mineral abundances and accessible surface areas. Chemical Geology, 523, 31-41.
- Samara, H., & Jaeger, P. (2021). Driving mechanisms in CO_2-assisted oil recovery from organic-rich shales. Energy & Fuels, 35(13), 10710-10720.
- Saadeldin, R., Gamal, H., Elkatatny, S., & Abdulraheem, A. (2022). Intelligent Model for Predicting Downhole Vibrations Using Surface Drilling Data During Horizontal Drilling. Journal of Energy Resources Technology, 144(8).
- Salehikhoo, F., & Li, L. (2015). The role of magnesite spatial distribution patterns in determining dissolution rates: When do they matter?. Geochimica et Cosmochimica Acta, 155, 107-121.
- Sheng, J., Jiahui, Z. H. A. O., & Ping, Y. U. E. (2022). An Experimental Study of the Effect of CO_2 Water-Mancos Shale Interactions on Permeability. International Journal of Earth Sciences Knowledge and Applications, 4(1), 26-31.

- Spokas, K., Peters, C. A., & Pyrak-Nolte, L. (2018). Influence of Rock Mineralogy on Reactive Fracture Evolution in Carbonate-Rich Caprocks. Environmental Science and Technology. https://doi.org/10.1021/acs.est.8b01021.
- Steefel, C. I., & Hu, M. (2022). Reactive Transport Modeling of Mineral Precipitation and Carbon Trapping in Discrete Fracture Networks. Water Resources Research, e2022WR032321.
- Steel, L., Liu, Q., Mackay, E., & Maroto-Valer, M. M. (2016). CO2 solubility measurements in brine under reservoir conditions: A comparison of experimental and geochemical modeling methods. Greenhouse Gases: Science and Technology, 6(2), 197-217.
- Tian, X., & Daigle, H. (2019). Preferential mineral-microfracture association in intact and deformed shales detected by machine learning object detection. Journal of Natural Gas Science and Engineering. https://doi.org/10.1016/j.jngse.2019.01.003.
- Wen, H., & Li, L. (2018). An upscaled rate law for mineral dissolution in heterogeneous media: The role of time and length scales. Geochimica et Cosmochimica Acta, 235, 1-20.
- Wu, S., Zou, C., Ma, D., Zhai, X., Yu, H., & Yu, Z. (2019). Reservoir property changes during CO2–brine flow-through experiments in tight sandstone: Implications for CO2 enhanced oil recovery in the Triassic Chang 7 Member tight sandstone, Ordos Basin, China. Journal of Asian Earth Sciences, 179, 200-210.
- Yoon, H., Ingraham, M. D., Grigg, J., Rosandick, B., Mozley, P., Rinehart, A., Mook, W. M., & Dewers, T. (2019). Impact of Depositional and Diagenetic Heterogeneity on Multiscale Mechanical Behavior of Mancos Shale, New Mexico and Utah, USA. In Memoir 120: Mudstone Diagenesis: Research Perspectives for Shale Hydrocarbon Reservoirs, Seals, and Source Rocks. https://doi.org/10.1306/13672214m1213824

CHAPTER 5

CONCLUSIONS AND CONTRIBUTION TO NEW KNOWLEDGE

5.1. Integrating machine/deep learning methods and filtering techniques for reliable mineral phase segmentation of 3D X-ray Computed Tomography images

Chapter 2 presents a study that explored the feasibility of using machine learning approaches with feature extraction techniques for pixel-level phase segmentation of shales in 3D X-ray CT images. This study provided new knowledge of the feasibility of machine learning for mineral phase segmentation in 3D X-ray CT images of shales. Once segmented, the categorized data could be used to retrieve useful information such as grain size distributions or mineral phase spatial distribution. To our knowledge, this study is the first to consider mineral phase segmentation in 3D X-ray CT images integrating both pixel-level classifications using machine learning models along with filtering techniques and image segmentation using a deep learning model on shale samples.

To improve the accuracy of the models, a feature engineering methodology was used that first extracted additional features from images using well-known filters and from the second convolutional layer of the pre-trained VGG16 architecture. Then, K-means clustering, Random Forest, and Feed Forward Artificial Neural Network methods, as well as the modified U-Net model, were applied to the extracted input features. The models' performances were then compared and contrasted to evaluate the performance of each model on reliable phase segmentation.

Based on the results for two different datasets, RF had the best accuracy among all applied machine learning methods due to its capability to handle imbalanced datasets and data scarcity. Adopting a feature engineering strategy into this model resulted in improved performance. Feature importance analysis showed the Median and Gaussian filters had the highest contribution in accurate phase segmentation because they remove unwanted noise and provide more integrated phases.

The results from U-Net showed even higher performance compared to RF. Considering all three methods of evaluations (i.e., F1-score, IOU, and accuracy), the U-Net method had a better performance in predicting each class compared to all other methods. It was also shown that the loss function plays an essential role in determining the model performance for both the Marcellus and Mancos samples. It was found that it is not efficient to train the model only based on a conventional loss function such as categorical cross-entropy since the majority class can negatively overwhelm the minority class. Instead, this study used focal and dice losses, which are focus-based loss functions, since they minimize the error based on each class in addition to overall error. As a result, a minority class is less likely to be overwhelmed by a majority class. Overall, it was shown that the U-Net deep learning model can outperform machine learning models for mineral phase segmentation and is the recommended approach for when a large dataset is available.

In addition to the new knowledge generated on the utility of machine learning for phase segmentation in 3D X-ray CT images, this work generated new open access codes for use by other researchers. The associated codes for the study are shared in GitHub (https://github.com/Parisa-Asadi/Integrating-machine-deep-learning-and-filtering-techniques-for-reliable-mineral-phase-segmentation). This includes developed frameworks for feature extraction and data engineering, data augmentation, image cropping, and the developed codes for mineral phase segmentation for

both the Mancos and Marcellus datasets based on K-means clustering, Random Forest, and Feed Forward Artificial Neural Network methods, VGG16 and U-Net.

The advancement in understanding facilitated via this study will help geologists distinguish between mineral phases in 3D X-ray CT images for reliable phase segmentation. Future work associated with this study would be to further distinguish discrete mineral phases by training ML/DL methods using SEM images of the surface of a given sample as ground truth for the X-ray CT mineral segmentation task. The trained model could then be utilized to segment the complete stack of X-ray CT images into individual mineral phases versus the groups of phases considered here.

5.2. Intelligent framework for mineral segmentation and fluid-accessible surface area analysis in Scanning Electron Microscopy

Integrating micro-imaging with machine learning based image-processing techniques can accelerate image processing but the performance of these models for accurate sample characterization and accessible surface area analysis has not previously been completely evaluated. Chapter 3 evaluated the potential of Random Forest and U-Net machine learning methods for mineral characterization. The utility of these approaches was evaluated for the first time on metrics related to analysis of surface area for scanning electron microscopy (SEM) backscattered electron (BSE) images of six sandstone samples with various resolutions. Filter extracted features, SEM BSE images and SEM-energy dispersive x-ray spectroscopy (EDS) images were all considered as input to the models. The performance of the models was investigated on a series of individual datasets as well as a combined dataset that included data from total samples, each with different grayscale intensity variation and resolution.

This chapter also proposed a novel mineral risk assessment map methodology which provides a robust solution to identify locations susceptible for dissolution. This new methodology can be utilized to once the models are segmented using the trained models to distinguish the surfaces more susceptible to dissolution for a given mineral. This map can capture variations in surface reactivity due to differences in accessibility where some surfaces are in contact with pores and thus accessible for reaction while others are occluded by mineral coatings, some of which are highly reactive. Occluded surfaces will be accessible for reaction once the coating phase dissolves. This approach can be used to consider the potential evolution of reactive surfaces. The dissolution risk assessment maps obtained from the models are compared with the labeled data to assess the efficacy of models for accurate surface area estimation.

In addition, the proposed framework not only evaluates the accuracy of prediction for each pixel, but also investigates the accuracy of predicted neighboring pixels, providing a more robust assessment of the models. The results showed that the models perform better when all BSE, EDS, filter data are used as input variables via the pooled dataset used to train the models. By considering these inputs, the U-Net model achieved an accuracy of 96% on the combined dataset, higher than Random Forest. In addition, the U-Net model had a better performance for surface quantification and had comparable results to the ground truth data for mineral abundances and accessibility. Feature importance, considered using Random Forest, showed that more information is gained from the extracted features and EDS elemental maps. It also showed the median and gaussian filters had the highest contribution for phase segmentation since they remove unwanted noise and therefore provide more integrated phases. Adopting a feature engineering strategy by including extracted features provided a robust solution to grayscale variation that changes from one dataset

to another. This is because the extracted features are invariant from one dataset to another, whereas the grayscale intensity for one feature can be different in various datasets. In addition, the proposed methodology combining machine learning-surface metrics was shown to reliably identify the locations susceptible for dissolution indicated via proposed risk assessment maps that indicate the accuracy of U-Net model in surface area analysis.

In addition, this work created new open access codes that are publicly available. The associated codes for the study are shared in the GitHub account (https://github.com/Parisa-Asadi/Machine-learning-for-Surface-Areas-Analysis). Codes include developed frameworks for feature extraction and data engineering, data augmentation, image cropping, the developed codes for mineral phase segmentation for different datasets as well as the combined dataset, accessibility and abundance analysis, and dissolution risk assessment analysis and mapping.

Overall, the intelligent mineral segmentation and surface area analysis framework is promising for accelerating the processing of SEM data, reactivity assessment of samples, and reducing post-process tasks, examined in various sandstone samples. The obtained parameters can enhance our understanding of sample characteristics such as mineralogy and reactive properties. Data such as porosity and mineral volume fractions can be quantified from processed maps and used to inform reactive transport simulations.

5.3. Modeling the Spatial and Temporal Mineral Evolution in Fractured Heterogenous System

Reactive transport modeling has been extensively used to help further understand geochemical reactions and transport phenomena in surface and subsurface systems. Mineral dissolution and precipitation reactions in fractures may alter fracture apertures, enhancing or reducing

permeability. This, however, is not well understood. Chapter 4 investigated the relationship between fracture surface compositions and the evolution of mineralogy, porosity, and ion concentrations in heterogeneous fractured rock domains over time and space to better understand the reactive evolution of fractures in heterogeneous media. The impact of fracture surface mineralogy and specific surface area on the spatial and temporal mineral reactions in fractures and the surrounding fracture matrix were explored and cross validated with the results obtained from bulk mineralogy. Variations in geochemical reactions and the system evolution were considered using different mineral compositions and distributions measured from image analyses of SEM-BSE images in prior work. These observations noted differences in mineral composition on the fracture surface as compared to that of the bulk sample and the implications of such observations considered here for the first time using reactive transport simulations. Simulations were carried out at short-term scale (days) and a long-term scale (years).

By comparing the temporal and spatial variations in simulated results for different cells, it was illustrated that cells close to either the inlet or fracture had higher reaction extents compared to the other cells. In all scenarios, it was found that the largest simulated change in the porosity, mineral composition and ion concentration happened in the cells located in the corner of the cross-section of the fracture and inlet. The evolution of mineral volume fractions followed similar patterns for calcite and dolomite dissolution for all scenarios and throughout the domain. However, the results occurred over different time scales. Over long-time scales, simulations reflecting the clay-rich region surrounding the fracture (the “perpendicular” scenario) had a slower simulated mineral evolution compared to other scenarios, which was also reflected in the simulated porosity evolution. In addition, for all scenarios, dissolution of some minerals such as calcite and dolomite

in inlet cells resulted in slower reaction and mineral evolution in mid- and down-stream cells, which was also intensified due to high dependency of flow transport to diffusion.

Overall, it was observed that the simulated mineral dissolution and porosity changes were faster for simulations reflecting the clay-rich region near the fracture surface followed by simulations with uniform mineral distribution as given by XRD analysis of the sample and lastly those with uniform mineralogy reflecting the bulk matrix mineralogy obtained from images. Simulation results also varied with surface area where simulation considering low surface area had lower porosity increment compared to the high BET SA simulation results. However, the simulations considering low BET SA for different scenarios followed the same pattern for porosity increment where the heterogenous scenario had highest porosity increment followed by simulations results for homogenous scenarios obtained from XRD analysis and the bulk matrix mineralogy.

It was also found that the simulated evolution of minerals and porosity for mid- and down-stream cells varies depending on the initial mineralogy as well as the time scale. Overall, for short-term simulations, those using the image obtained matrix mineralogy had larger simulated changes in mineralogy and consequently higher increases in porosity. However, simulation results for cells adjacent to the fracture for the long-term period showed that simulations using the bulk XRD mineralogy had more extensive dissolution and consequently higher increases in porosity compared to those reflecting the clay-rich region near the fracture.

Comparison of major ion concentrations, porosity and mineral volume fraction evolution among different scenarios showed higher evolution in simulations using the bulk XRD mineralogy simulation compared to those reflecting the clay-rich fracture region. Fracture apertures were simulated to decrease due to a small amount of quartz precipitation. In addition, different patterns

of dissolutions for different minerals such as Illite and k-feldspar in different scenarios resulted in variations in matrix porosity. Regions initially limited to diffusion, because of low porosity and permeability, may become more reactive as phases dissolve, resulting in mineral reactions unpredicted by bulk formation data. This may because that bulk mineralogy neither considers mineral distribution nor physical heterogeneity, which may result in simulations unable to accurately reflect actual mineral reactions that may occur, especially for cells adjacent to the fracture. The results could improve our ability to predict reactive fracture evolution and understand implications for subsurface CO_2 sequestration and oil recovery.

In addition, this work produced open access codes for the reactive transport simulations. The codes for the study are shared in the GitHub account (https://github.com/Parisa-Asadi/Modeling-the-Spatial-and-Temporal-Mineral-Evolution-in-Fractured-Heterogenous-Systems-/upload/main). This includes the developed framework for 2D dimension porous media developed in the Crunchflow software and codes for processing the output files and plotting the results.